Volume 4 | 2014
ISSN 2231 – 0002 | EISSN 2231 – 0010

Physics Express

Proceedings of
International Conference on Material Science (ICMS 2013)

organized by
Department of Physics, Tripura University (A Central University), India
during 21 – 23 February, 2013

Cognizure

www.cognizure.com/physics

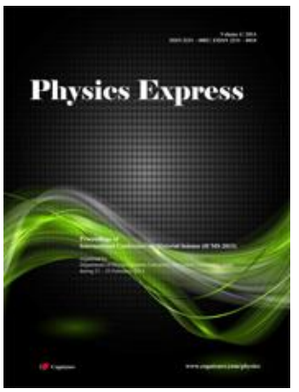

Physics Express

Proceedings of
International Conference on Material Science (ICMS 2013)

organized by
Department of Physics, Tripura University (A Central University), India
during 21 – 23 February, 2013

Cognizure

Table of Contents

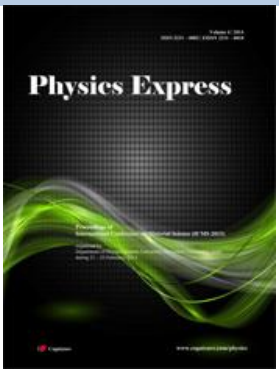

Editorial

Proceedings of International Conference on Material Science (ICMS 2013)

It is a matter of great pleasure to bring out the proceedings of the International Conference on Material Science (ICMS-2013) as a special issue of Physics Express. ICMS-2013 conference covered a wide range of interdisciplinary and current research topics related to Material Science including nanomaterials, biomaterials, semiconductor & electronic materials, composites, surface engineering, sensor technology, modeling & simulation of material phenomena and other advance materials. This international conference helped the researchers around the world exchange the state-of-the-art of research & development and identify research needs as well as to open new doors for collaborative research in different aspects of Material Science.

The conference was inaugurated by Prof. Krishan Lal, President, Indian National Science Academy and former Director, National Physical Laboratory, New Delhi. Prof. Mushahid Hussain, Director, Centre for Nanoscience and Nanotechnology, Jamia Millia Islamia, New Delhi, delivered the keynote address on "Carbon nanotube based field emission displays". There were five foreign invited speakers out of total fourteen invited talks. Totally 176 contributory papers (oral: 46 and poster 130) were presented by researchers from different parts of the globe.

On behalf of the organizing committee, I would like to extend my sincere thanks to all the participants and the contributors for their active participation, without which it might not be possible to organize this conference successfully and publish this special issue. I would like to take the opportunity to acknowledge the financial support rendered by DST, Govt. of India, CSIR, Govt. of India, BRNS, Govt. of India, DBT, Govt. of India, INSA, New Delhi, MoES, Govt. of India, DRDO, Govt. of India, and Tripura University to organize this prestigious conference. Finally, I would like to thank the Editors and staff members of the Physics Express for their cooperation for publishing this special issue.

Dr. Syed Arshad Hussain
Convener
ICMS 2013 conference

Synthesis of ZnO nanoleaf via plasma enhanced reactive evaporation and its structural, optical and field emission properties

D. Banerjee[b,*], K. K. Chattopadhyay[a,b,*]

[a] *Thin Films and Nanoscience Laboratory, Department of Physics, Jadavpur University, Kolkata 700 032, India*
[b] *School of Material Science and Nanotechnology , Jadavpur University, Kolkata 700 032, India*

[*] *Authors for Correspondence: K. K. Chattopadhyay, email: kalyan_chattopadhyay@yahoo.com*
D. Banerjee, email: nilju82@gmail.com
Received 29 Mar 2013; Accepted 26 Apr 2013; Available Online 26 Apr 2013

Abstract

This article reports for the first time the synthesis of ZnO nanoleaf-like structure via plasma enhanced reactive evaporation on both silicon as well on glass substrate. The as-prepared samples were studied by X-ray diffraction, energy dispersive analysis of X-rays, field emission scanning electron microscope, high resolution transmission electron microscope, UV-Vis-NIR spectroscopy and photoluminescence spectroscopy. The direct band gap obtained from the optical transmittance spectra came out to be 3.08 eV thus proving the sample to be a wide band gap material. The as-prepared sample has shown room temperature photoluminescence at 388 nm which was assigned as band-to-band transition. Also the efficient field emission characteristic has been obtained from the sample with a turn-on field ~5.71 V/μm. The field emission characteristics have been analyzed via both Millikan-Lauritsen and Fowler-Nordheim technique and a relation regarding the slope of the corresponding linear fit and enhancement factor between the two plots has been shown.

Keywords: Plasma enhanced evaporation; Zinc oxide; Nano structure; Photoluminescence; Field emission

1. Introduction

Zinc oxide (ZnO) is a versatile material regarding its diverse properties that includes piezoelectricity, chemical stability, biocompatibility, optical transparency in the visible region, high voltage-current nonlinearity etc [1]. Owing to these properties, ZnO posesses immense potential in different applications such as in solar cells, transparent electrodes, blue/UV light emitter device, gas sensor, and also in many other [2-6]. Zinc oxide (ZnO), a direct and wide band-gap (3.37 eV) semiconductor with large exciton binding energy of 60 meV at room temperature, has been considered as a promising high efficient short-wavelength light-emitting material operating at room temperature [7, 8]. Due to very high aspect ratio different 1-D ZnO nanostructures can very efficiently be used as field electron emitter [9]. In the last few decades enormous research works have been done on the synthesis of different zinc oxide nanostructures and to use them in different application fields. Those nanostructures include 0-D nanoparticles [10], 1-D nanowires, nanotubes, nanocombs, nanohelices, [11-15] etc. Also chemical vapor deposition, thermal evaporation, template-involved processes and solution-phase synthesis, have been employed successfully for preparing more complex two-dimensional (2D) and three-dimensional (3D) superstructures of ZnO [16, 17]. However there are not many reports regarding the synthesis of ZnO leaf-like structure except a few. For example, Yang et al. reported synthesis of ZnO nanoleaf by pulsed laser ablation of aqueous solution [18]. Zhang et al. reported the homo-epitaxial growth and optical properties of ZnO polar nanoleaves by thermal evaporation [19]. She et al. reported the synthesis of bamboo-leaf-shaped ZnO nanostructures by oxidation of Zn/SiO_2 composite films [20]. Wu et al. synthesized the lotus leaf-like ZnO nanostructure and studied its hydrophobicity [21]. But so far the authors are concerned there is no report regarding the synthesis of ZnO nanoleaf by plasma enhanced reactive evaporation (PERE). Owing to this fact, in this paper we have reported the synthesis of leaf-like ZnO nanostructure by PERE and studied its room temperature photoluminescence. Also for the first time electron field emission from such structure has been reported here.

2. Experimental Details

Zinc Oxide nanoleaf-like structure in thin film form has been deposited on both glass and silicon substrates via plasma enhanced reactive evaporation of zinc acetate. Before the film deposition, the Si substrates were immersed in 20% HF solution for 5 min prior to ultrasonically cleaning for 10 minutes. The glass substrates were thoroughly clean step by step with base, acid and finally ultrasonicated for 10 minutes. Immediately after cleaning the substrates, they were transferred to the evaporation chamber which was evacuated to a pressure $\sim 10^{-6}$ mbar with the help of a rotary and a diffusion pump. The schematic of the PERE has been shown in Figure 1. The process is rather simple a partially covered Mo heater, as shown in Figure 1 was used as an electrode in the evaporation chamber. The Zn precursor was placed inside the heater whereas the substrates were placed on it. Current was passed with appropriate arrangements in order to heat up and evaporate the precursor, at the same time oxygen was passed and plasma was ignited by applying a D. C. voltage. All the deposition parameters of the synthesis process have been summarized in Table 1.

After the deposition is over the as prepared samples were cooled normally and characterized by X-ray diffraction

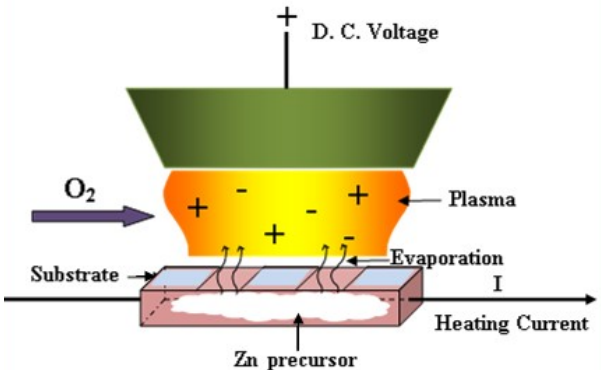

Figure 1. Schematic of PERE process.

(XRD, Bruker D8 Advance), energy dispersive X-ray analysis (EDX, Oxford, model-7582), field emission scanning electron microscopy (FESEM, Hitachi, S-4800), high resolution transmission electron microscopy (HRTEM, JEOL-JEM 2100), UV-Vis-NIR spectrometer (Shimadzu UV-3101PC) and Elico fluorimeter. In addition field emission characteristic of as-prepared sample has been synthesized via our laboratory made high vacuum field electron emission measurement set-up. It is to be noted that the sample deposited on glass was used only for transmission study and all the other characterizations were done with sample deposited on silicon substrate.

3. Results and Discussion

3.1. EDX and XRD study

The elemental composition of the as-prepared sample was obtained using EDX spectrum, shown in Figure 2. The strong peaks, attributed to Zn and O are clearly present in the EDX spectrum and no other impurities were detected confirming high purity of the product. Moreover, according to quantitative analysis of EDX, the weight percentage of Zn and O is 70.41 and 29.59 respectively. Inset of Figure 2 shows the XRD pattern of as-deposited sample. XRD was studied, using a diffractometer by Cu Kα radiation (λ= 0.15406 nm),

Table 1. Deposition parameters for synthesizing nano leaf-like ZnO structure.

Parameter	Value/Description
Substrate used	Cleaned glass and silicon
Inter-electrode distance	~2 cm
Reacting gas	Oxygen
Temperature	450^0C
Final pressure	1 mbar
Applied D.C. voltage	1.5 kV
Duration of Deposition	15 minutes

operating at 40 kV, 40 mA with a normal θ–2θ scanning. The spectra shows three strong peaks centering on 2θ= 31.92°, 34.64°, 36.44° that corresponds to (100), (002) and (101) plane of hexagonal wurtzite structured ZnO. The absence of any additional peak confirms the pure phase formation of the as-synthesized sample.

3.2. Microscopic Study

Figure 3 shows the FESEM images of the as-prepared sample with different magnifications deposited on Si (a-c) and glass (d-f) substrate. It can be seen that the deposition occurred uniformly throughout the entire substrate and thus can be called large area deposition. From Figure 3b and c it has been seen that the length and breadth of the larger leafs are around 300 nm and 100 nm respectively. But most of the other leaves have dimensions much smaller compared to that. More interestingly it can be seen from Figure 3 (a-f) that substrate does not have much effect onto the morphology of ZnO structure and thus ZnO synthesized on Si as well as glass substrate produces same nanoleaf-like structure. HRTEM images of the as-prepared sample with corresponding lattice image and selected area electron diffraction (SAED) pattern has been shown in Figure 3(g-i). It has been seen that due to ultra-sonication the leaf structures are not remained intact and have broken into several 1-D rods having diameter ~ 50-100 nm. So it can be concluded that these rods are basically the building block of this kind of structure. Based on this a possible growth mechanism can be proposed where it is speculated that Zn precursor first get sublimated to produce Zn

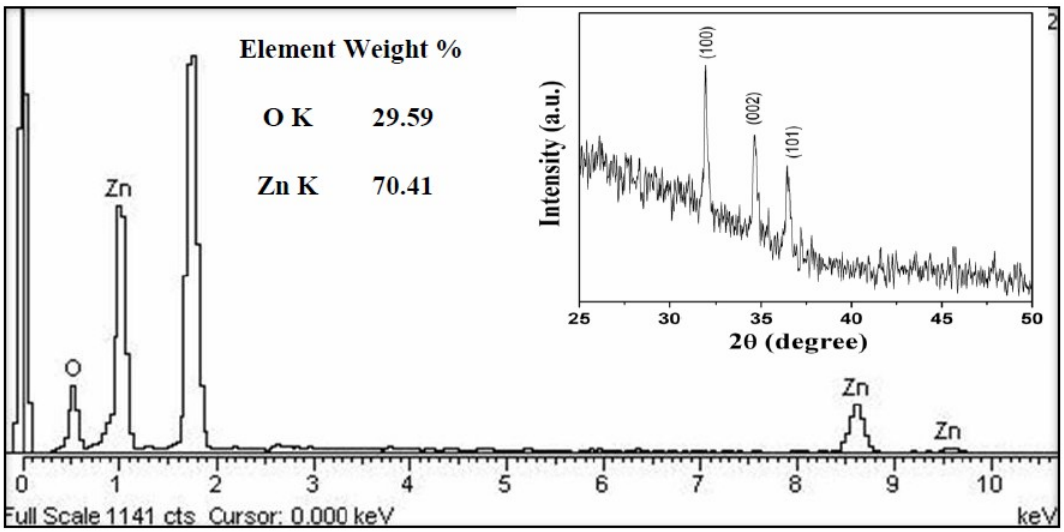

Figure 2. EDX spectrum of the ZnO nanoleaf-like structure with corresponding atomic percentage of the elements; X-ray diffraction pattern of the as-synthesized sample has been shown in the inset.

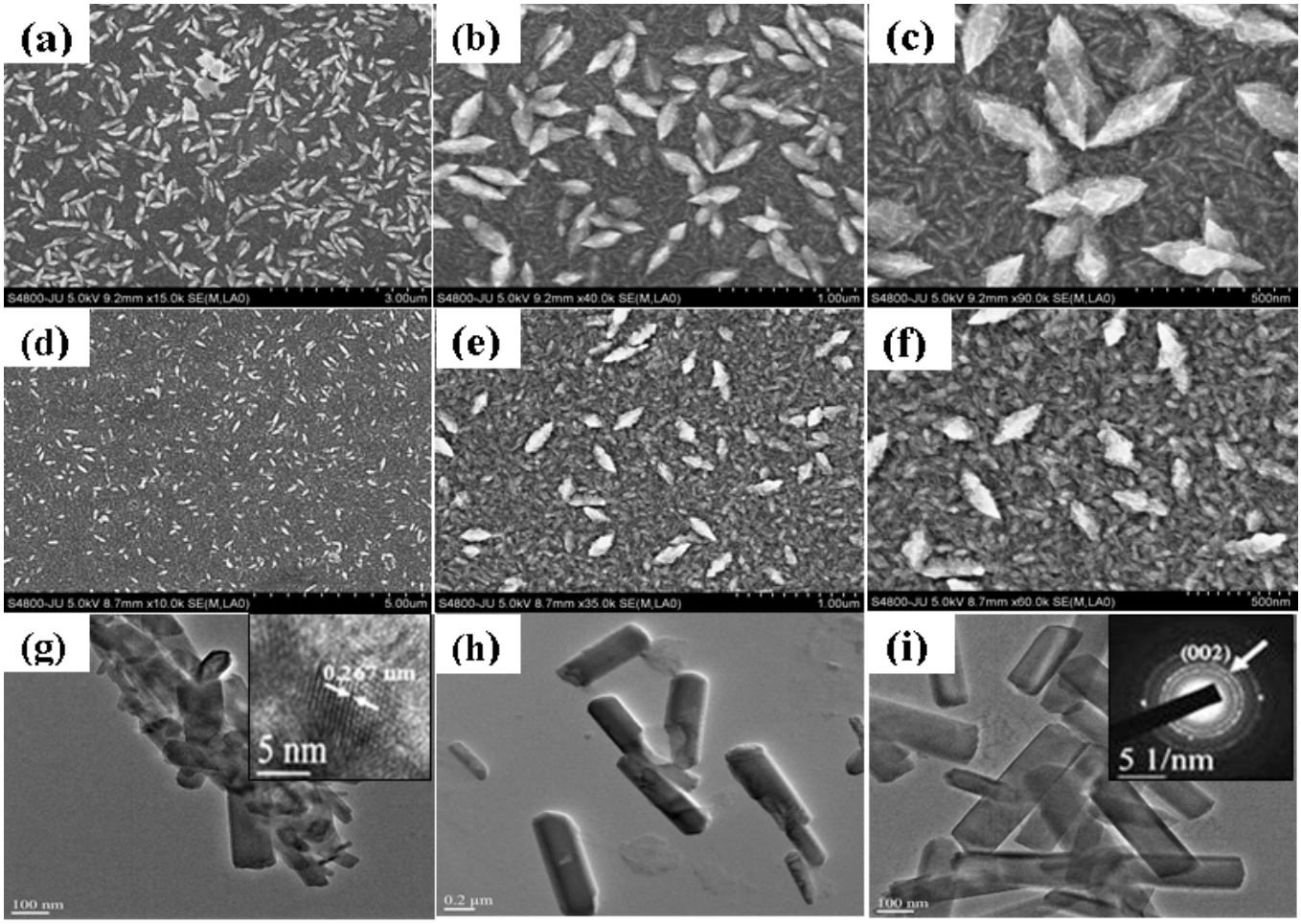

Figure 3. FESEM images of ZnO nanoleaf with different magnifications deposited on Si; (d-f) deposited on glass and (g-i) HRTEM images of the same with lattice image and SAED pattern shown in the inset.

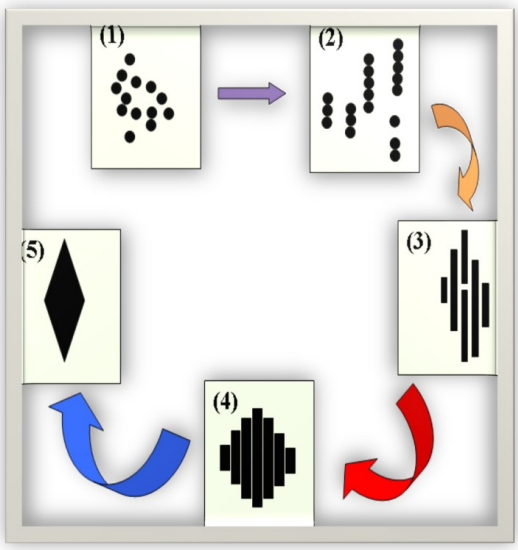

Figure 4. Schematic of possible growth mechanism.

nanoparticle which can be readily oxidized to ZnO under high temperature, oxygen flow and plasma. ZnO has an inherent tendency to grow along c axis and thus to form a rod-like structures which get coalesced side-by-side to form this leaf as suggested by Yang et al. [17]. The whole states of affairs have been shown in Figure 4. Lattice image of (002) plane of zinc oxide has been shown in Figure 3g with corresponding SAED pattern shown in the inset to Figure 3i. It can be seen from either of the two figures that the sample is polycrystalline in nature.

3.3. Optical transmittance and photoluminescence (PL) study

Figure 5 shows the optical transmittance spectra of the as-prepared sample synthesized on glass substrate from which the direct band gap can be obtained by plotting $(\alpha h\nu)^2$ with $(h\nu)$ as shown in the inset to Figure 5 where α is the extinction coefficient. It is seen that the direct band gap has come out to be 3.08 eV. This value is rather lower compared to the existing literature (3.37 eV) but the synthesized nanostructures are having much oxygen deficient as can be clearly seen from EDX results (Figure 1). The excess Zn, produce donor levels and at higher concentration of the same, it converts into impurity band which merge with the conduction band bottom. This will lower the band gap and that is why we get its value 3.08 eV. It may be mentioned that exciton Bohr radius of ZnO is extremely small ~ 2 nm, hence widening of band gap due to carrier confinement is unlikely to occur in this case as the particle sizes are much bigger.

A room temperature PL spectrum of the as-prepared sample deposited on glass substrate has been shown in Figure

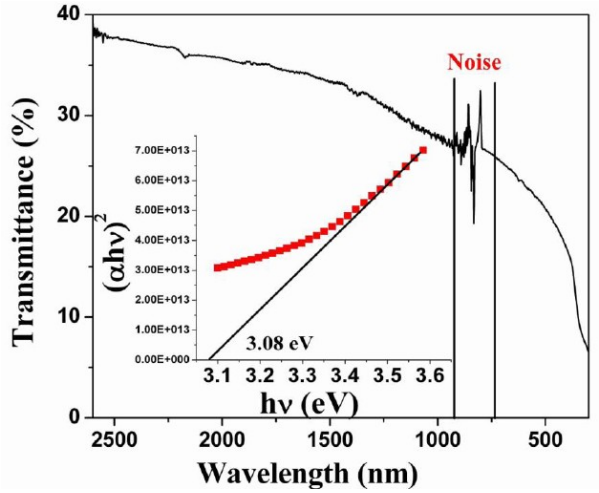

Figure 5. Transmittance spectra of ZnO nanoleaf deposited on glass substrate and inset plot of $(\alpha h\nu)^2$ with hν for the determination of band gap.

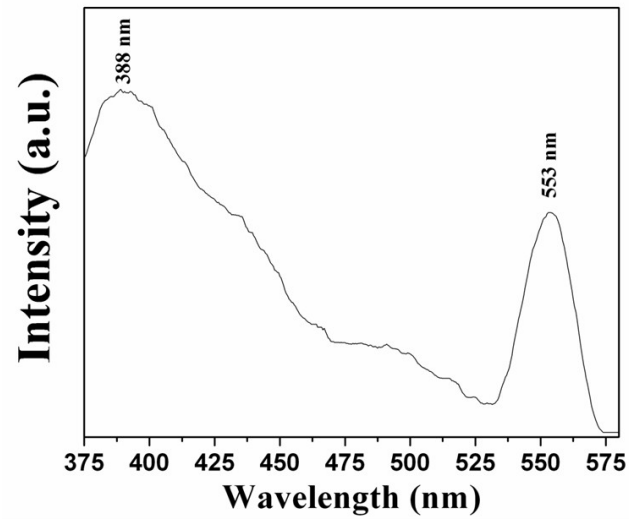

Figure 6. Photoluminescence spectra of ZnO nanoleaf.

6. The excitation wavelength was 325 nm applied by using a conventional xenon lamp. The spectrum shows two distinct peaks around 388 nm i.e. in the UV region and other centering around 553 nm thus in visible region. The UV emission is well understood as near-band-edge emission, while the visible emission originates from a variety of deep level defects, e.g. vacancies from oxygen and zinc interstitials [22, 17]. This basically comes from the recombination of photo-generated holes with singly ionized charge states in intrinsic defects as mentioned above.

3.4. Field emission study

Field emission characteristics of as-synthesized ZnO nanoleafs were taken in our home-made high vacuum field emission set up. The macroscopic applied electric field can be obtained by dividing the applied voltage by the inter electrode distance. Theoretically, the emission current and the macroscopic electric field are related to each other by the well-known Fowler Nordheim equation [23].

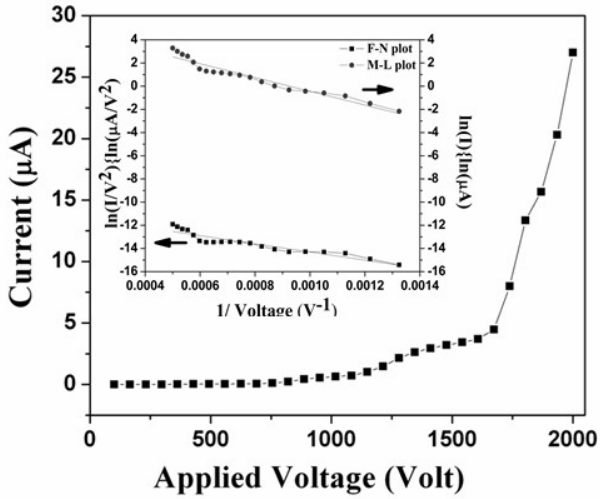

Figure 7. Field emission I-V characteristics of ZnO nanostructure and both F-N and M-L plots in the inset.

$$I = Aat_F^{-2}\phi^{-1}(\beta E)^2 \exp\{-bv_F\phi^{3/2}/\beta E\} \quad (1)$$

Where A is the effective emission area, ß is the enhancement factor, t_F , v_F are the values of special field emission elliptic function for a particular barrier height ϕ [24], a and b are respectively the first and second Fowler–Nordheim (F-N) constants having values $a=1.541434\times10^{-6}$AeV V^{-2} and $b=6.830890\times10^{9}eV^{-3/2}V\ m^{-1}$. The F-N equation when simplified takes the form as

$$\ln\{J/E^2\} = \ln\{t_F^{-2}a\phi^{-1}\beta^2\} - [\{v_F b\phi^{3/2}\beta^{-1}\}/E] \quad (2)$$

where J= I/A is the macroscopic current density

Hence plot of $\ln\{J/E^2\}$ vs. 1/E should be a straight line and its slope and intercept gives the valuable information about the enhancement factor, local work function etc. An experimental F-N plot has been modeled and can be expressed as

$$\ln\{J/E^2\} = \ln\{ra\phi^{-1}\beta^2\} - [\{sb\phi^{3/2}\beta^{-1}\}/E] \quad (3)$$

where r and s are respectively the intercept and slope correction factors. Typically, the value of s is nearly unity but r may have values, which may be as high as 100 and even greater.

The enhancement factor (β) and the effective work function (Φ_{eff}) can be calculated from the slope (m) of the F-N plot using the relation:

$$\beta = (-b\Phi^{3/2})/m \quad \text{and} \quad \Phi_{eff} = \Phi/\beta^{2/3} \quad (4)$$

Here Φ has been taken as 5.3 eV for ZnO [9].

Taking electric field as independent parameter is customary when the emitting surface is perfectly smooth otherwise, for rough surfaces as in our cases; it is more convenient to plot I–V instead of J–E or I–E. The experimental I-V characteristic of the as-prepared sample has been shown in Figure 7 with there corresponding linear plot shown in the inset. The turn-on field has been defined as the field required

Table 2. Different parameters obtained from the analysis of field emission characteristic.

Parameter	Value/Description
Turn-on field	5.73 V/μm
Slope (F-N plot)	-3537 V
Slope (M-L plot)	-5943 V
$\mathbf{m_{F\text{-}N} = m_{M\text{-}L} + 2\times[V]_{average}}$	-3276 V
β (F-N plot)	2788
$\mathbf{\Phi_{eff}}$ **(F-N plot)**	0.027 eV

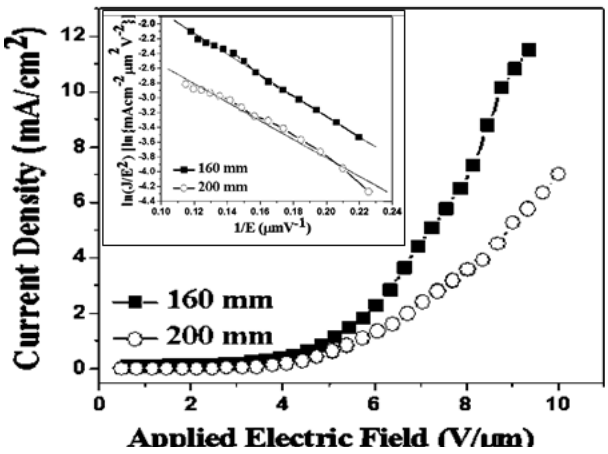

Figure 8. Field emission I-V characteristics of ZnO nanostructure for two different inter-electrode distances with corresponding F-N plot shown in the inset.

to obtain an emission current 0.5 μA and has come out to be 5.7 V/μm (inter-electrode distance d=160 μm). Before going to the detail F-N analysis it is to be noted that there is another very old method for analyzing the field emission data which recently came into limelight [25] known as Millican-Lauritsen (M-L) plot, that used ln(I) with 1/V. Basically all the plots (either F-N or M-L) originated from the mother equation

$$I = CV^k \exp(-B/V) \quad (5)$$

where B and C are constants.

F-N plots take k=2 whereas M-L plot considers it zero. This readily suggests that there must be definite relationship between the slopes of both the plots. It can be shown through simple mathematical manipulation that

$$m_{F\text{-}N} = m_{M\text{-}L} + 2\times[V]_{average} \quad (6)$$

where m stands for the slope.

Table 2 summarized the turn-on field, enhancement factor and effective work function of the sample as calculated from the F-N analysis. Also the slopes of all the two plots are tabulated to verify equation 6. Though F-N plot is widely used but some people like M-L plot due to its simplicity. Also beside simplicity there are more serious reasons for using M-L plots like:

(1) Sometime explicit voltage dependence of emission current is not known. Then ML approach is easier when one wants to make corrections for all physical sources of voltage dependence in the data, or to estimate uncertainties in derived parameter.

(2) Sometime experiments demand only to check whether the electrons are emitted due to cold field emission or not. Then checking the linearity of M-L plot is as good as that of F-N plot.

(3) Most importantly M-L plots are applicable to more wide class of materials unlike the F-N approaches which is strictly applicable to bulk metals only (though now being used in all the cases)

Figure 8 shows the field emission characteristics of as-prepared sample with two different inter-electrode distances with corresponding F-N plots shown in the inset. It is seen that field emission characteristics get worse with increasing inter-electrode distance. The explanation has been given in our previous work [26]. Briefly speaking, here conical shaped stainless steel anodes were used and hence the lines of force are diverging in nature, particularly due to the well-known edge effect. Hence when the anode-cathode distance was small, the number of lines of force passing through the emission sites of the underneath samples per unit area was larger and its number density decreases when the anode cathode distance increased thus the field strength decreases causing an inferior field emission characteristics.

4. Conclusions

Zinc oxide nanoleaf-like structure has been synthesized via plasma enhanced reactive evaporation of the zinc salt. The XRD and EDX study confirms the pure phase formation of the sample. FESEM and HRTEM study has shown that the as-prepared leaves have a diameter ~ 50-100 nm and composed of several 1-D rod-like structures. A room temperature PL spectrum has shown peaks originated both band edge emission as well as the emission from the defects level. Field emission characteristic has been synthesized both by F-N plot and M-L plot and a relation between these two has been drawn.

Acknowledgments

The authors wish to acknowledge West Bengal State Government during the execution of this work for giving the financial support under the state fellowship scheme. We also wish to acknowledge the financial support under UPEII scheme, the University Grants Commission, the Govt. of India.

References

1. D. C. Look, Mater. Sci. Eng. B 80 (2001) 383.
2. T. Negami, Y. Hashimoto, S. Nishiwaki, Sol. Energy Mater. Sol. Cells 67 (2001) 331.
3. C. Lee, K. Lim, J. Song, Sol. Energy Mater. Sol. Cells 43 (1996) 37.
4. Y. Natsume, H. Sakata, Thin Solid Films 372 (2000) 30.
5. D. C. Look, D. C. Reynolds, C. W. Litton, R. L. Jones, D. B. Eason, G. Cantwell, Appl. Phys. Lett. 81 (2002) 1830.
6. X. Wang, W. P. Carey, S. Yee, Sens. Actuat. B 28 (1995) 63.
7. M. Alhamed, W. Abdullah, J. Electron Devices 7 (2010) 246.
8. R. F. Service, Science 276 (1997) 895.
9. U. N. Maiti, Sk. F. Ahmed, M. K. Mitra, K. Chattopadhyay, Mater. Res. Bull. 44 (2009) 134.
10. S. Music, D. Dragcevic, S. Popovic, M. Ivanda, Mater. Lett. 59 (2005) 2388.
11. Y. N. Xia, P. D. Yang, Y. G. Sun, Y. Y. Wu, B. Mayers, B. Gates, Y. D. Yin, F. Kim, Q. Yan, Adv. Mater. 15 (2003) 353.

12. M. H. Huang, S. Mao, H. Feick, H. Yan, Y. Wu, H. Kind, E. Webe, R. Russo, P Yang, Science 292 (2001) 1897.
13. B. P. Zhang, N. T. Binh, K. Wakatsuki, Y. Segawa, Y. Yamada, N. Usami, M. Kawasaki, H. Koinuma, Appl. Phys. Lett. 84 (2004) 4098.
14. C. S. Lao, P. X. Gao, R. S. Yang, Y. Zhang, Y. Dai, Z. L Wang, Chem. Phys. Lett. 417 (2005) 359.
15. P. X. Gao, Y. Ding, W. J. Mai, W. L. Hughes, C. S. Lao, Z. L. Wang, Science 309 (2005) 1700.
16. J. P. Liu, X. T. Huang, Y. Y. Li, K. M. Sulieman, F. L. Sun, X. He, Scr. Mater. 55 (2006) 795.
17. B. Liu, H. C. Zeng, J. Am. Chem. Soc. 126 (2004) 16744.
18. L. Yang, P. W. May, L. Yin, T. B. Scott, Nanotechnology 18 (2007) 215602.
19. C-Z. Zhang, H. Gao, D. Zhang, X-T Zhang, Chin. Phys. Lett. 25 (2008) 302.
20. L. Shi, Y. Li, C. Xue, H. Zhuang, J. He, D. Tian, Appl. Surf. Sci. 252 (2006) 2853.
21. J. Wu, J. Xia, W. Lei, B-P. Wang, Mater. Lett. 65 (2011) 477.
22. Y. Sun, G. M. Fuge, N. A. Fox, D. J. Riley, M. N. R. Ashfold, Adv. Mater. 17 (2005) 247.
23. R. H. Fowler, L. Nordheim, Proc. R. Soc. Lond. A 119 (1928) 173.
24. E. L. Murphy, R. H. Good, Phys. Rev. 102 (1956) 1464.
25. R. G. Forbes, J. Appl. Phys. 105 (2009) 114313.
26. D. Banerjee, A. Jha, K. K. chattopadhyay, Physica E 41 (2009) 1174.

Cite this article as:

D. Banerjee *et al.*: **Synthesis of ZnO nanoleaf via plasma enhanced reactive evaporation and its structural, optical and field emission properties.** *Phys. Express* 2014, **4:** 1

Organic Light Emitting Diode (OLED) materials from spirobifluorene derivatives

R. N. Jana*, S. Chakraborty, R. Banerjee

Department of Chemical Engineering, Haldia Institute of Technology, ICARE Complex, Pura Medinipur, Haldia – 721657, India

Author for correspondence: R. N. Jana, email: rabindrajana@yahoo.com
Received 13 Feb 2013; Accepted 29 Mar 2013; Available Online 29 Mar 2013

Abstract

Novel spirobifluorene (SBF) derivatives containing different π-conjugated functional groups were synthesized using a cross coupling reaction with palladium (Pd) catalyst under an inert atmosphere. The synthesized SBF derivatives showed the photoluminescence (PL) emission spectra in the range from blue to near-UV range i.e., from 2.7 eV (461 nm) up to 3.5 eV (352 nm). However, the naphthyl and amine contained derivatives showed a significant deviation in PL, photoluminescence excitation (PLE), and UV-Vis absorption (OD) spectroscopy, indicating their additional photon energy specific to non-radiative decay channels. Time-dependant density functional theory (TD-DFT), based on the B3LYP functional with the 6-31G(d) basis set using Gaussian 98 package, was applied to calculate the ground state energy, excited triplet and singlet states energies. The calculated excitation energies (ε), oscillator strength (f) and dominant orbital excitation showed that these compounds may produce a blue emission due to the extended conjugation length of the SBF derivatives thus suggesting their use as promising blue organic light-emitting diode (OLED) materials.

Keywords: Organic light-emitting diode (OLED); Spirobifluorene; Photoluminescence; Electroluminescence; Time-dependent density functional theory (TD-DFT)

1. Introduction

Nowadays, organic light-emitting diode (OLED) materials are in great deal due to their potential applications in light emitting devices and flat panel displays [1-3]. OLEDs are made from semiconducting organic molecules, especially π-conjugated oligomers or polymers with many advantages e.g., their better brightness, faster response time, lighter weight, cheaper fabrication, and no backlight requirement etc. over liquid crystal displays (LCDs), except their lower efficiency and poor service life [4, 5]. The spirobifluorene (SBF) derivatives in this respect are considered to be the promising blue light emitting materials because of their high photoluminescence (PL) and electroluminescence (EL) efficiencies, thermal stability, and ready color-tuning through the introduction of low-band-gap comonomers [6–8]. Easy functionalization at 2,2′,7,7′ positions of the SBF unit improves solubility and processability of these compounds [9,10]. Moreover, due to presence of fused aromatic rings in the SBF compounds the inter-chain interaction is believed to be less possible which in turn will reduce broadening of emission spectrum effectively [11]. Unfortunately, during long time device operation the tendency to display undesired long-wavelength emission bands upon exposure to heat and consequently the color instability and reduced efficiency, are the crucial problems which have limited the application of SBFs in OLEDs [12]. Several chemical approaches have been utilized to improve the efficiency and to enhance the color stability of the compounds e.g., introduction of low-band-gap chromophores [13], end-capping with cross-linkable materials [14] or introduction of hole-trapping groups [15], kinking the backbone structure [16], encapsulating the polymer backbone with bulky side chains [17-19] and incorporation of siloxane bridges or polyhedral oligomeric silsesquioxane (POSS) units [20]. Out of the approaches, introduction of low band gap chromophores is very effective and therefore we have incorporated several π-conjugated molecules, e.g., phenylacetylene, 4-*n*-butylphenylacetylene, triphenylsilyl acetylene, 4-ethynylbiphenyl, 1-ethynylnaphthalene, 4-ethynyl-N,N-dimethylaniline, and 1-ethylenenaphthalene, etc into the SBF moiety to get the desired light emitting materials. Here we have described the synthesis of the polymers starting from commercially available SBF by bromination and then cross coupling reaction with different conjugated substitutions to get the 2,2′,7,7′ substituted SBF derivatives. The synthesized three-dimensional structure would restrict close packing of the macromolecules and reduce the inter-chain π - π* interactions and thus may suppress the aggregate or excimer formation and enhance PL efficiency. The synthesized polymers are characterized by means of UV-Vis absorption (OD), photoluminescence (PL) and photoluminescence excitation (PLE) spectroscopy. The time-dependent density functional theory (TD-DFT) is applied to calculate the time-dependent excitation energies (ε), oscillator strength (f) and dominant orbital excitation with the interaction of molecules in an electric laser field.

2. Experimental Details

2.1. Materials

The different π-conjugated compounds e.g., phenylacetylene, 4-*n*-butylphenylacetylene, triphenylsilyl acetylene, all other reagents and solvents were purchased from Aldrich Co. and used without any further purification.

2.2. Synthesis of SBF compounds

The chemical structures of different SBF derivatives are shown in Figure 1 and their synthesis methods (Scheme 1) are reported here.

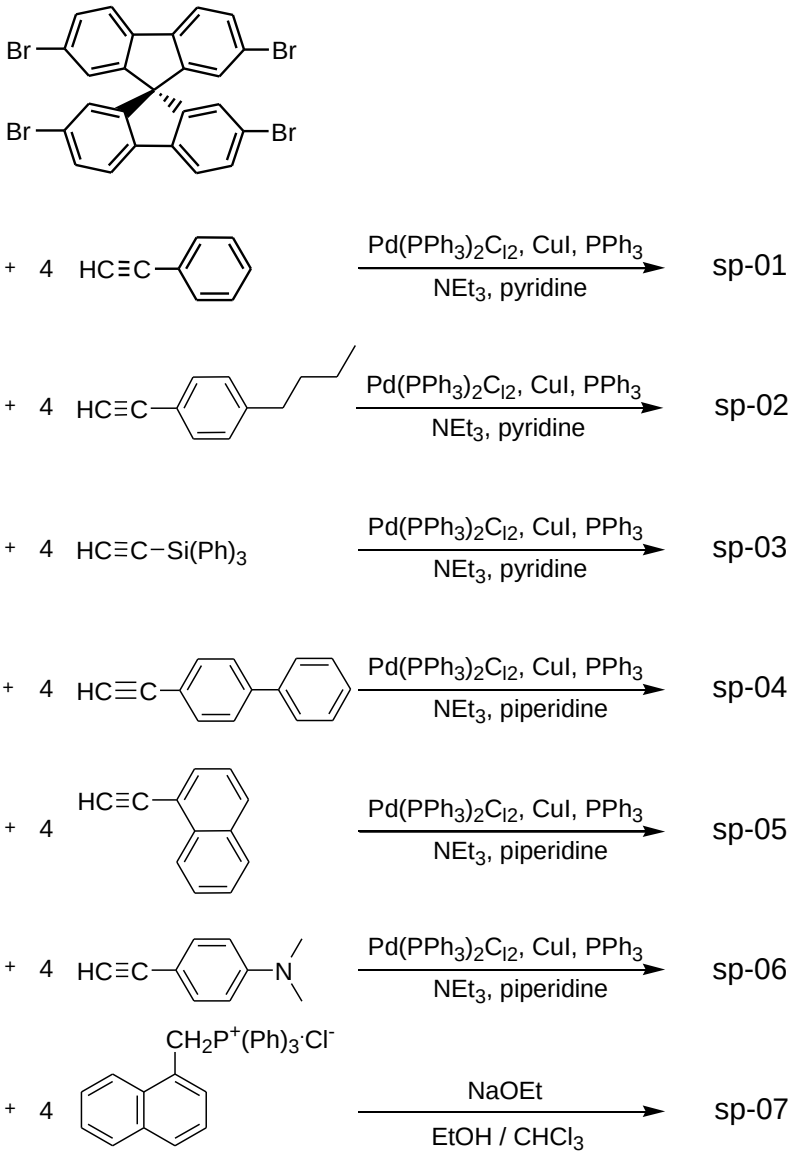

Scheme 1. Synthetic routes for novel SBF derivatives.

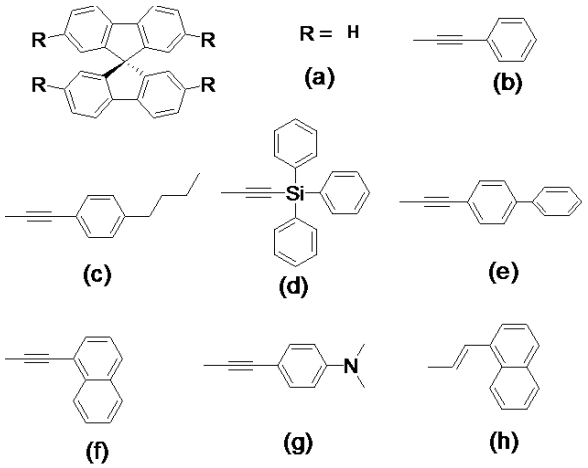

Figure 1. Chemical structures of different SBF derivatives with different substitutions e.g., (a) R=H, (b) Phenylacetylene, (c) 4-*n*-butylphenylacetylene, (d) triphenylsilylacetylene, (e) 4-Ethynylbiphenyl, (f) 1-ethynylnaphthalene, (g) 4-Ethynyl-N,N-dimethylaniline , (g) 2,2′,7,7′-tetraformyl-9,9′-spirobifluorene, (h) in this study.

Synthesis of sp-00: 9, 9′-Spirobifluorene (sp-00) and 2,2′,7,7′-tetrabromo-9,9′-spirobifluorene were synthesized using a reported procedure [21].

Synthesis of sp-01: Phenylacetylene (0.53 ml, 4.8 mmol), 2,2′,7,7′-tetrabromo-9,9′-spirobifluorene (0.632 g, 1 mmol), triethylamine (5.57 ml, 40 mmol), pyridine (3.24 ml, 40 mmol) was added to the three neck 100 ml flask fitted with reflux condenser, and the flask was cooled down to 0°C and $Pd(PPh_3)_2Cl_2$ (28.1 mg, 0.04 mmol) and CuI (26.6 mg, 0.14 mmol), PPh_3 (56.4 mg, 0.215 mmol) were added. The reaction mixture was slowly warmed up to 70°C and stirred overnight. To the reaction mixture 30 ml water was added, and the resulted precipitate was filtered off, recrystallization with CH_2Cl_2 and ethanol mixture gave 0.45 g (63% yield) gray solid of sp-01. ^{1}H-NMR (400MHz, $CDCl_3$); δ 7.0 (d, 4H), 7.36 (m, 12H), 7.5 (dd, 8H), 7.6 (dd, 4H), 7.9 (d, 4H), and ^{13}C-NMR ($CDCl_3$); δ 67, 89.8, 90.7, 120.8, 123.4, 123.5, 127.7, 128.6, 131.9, 132.2, 141.5, 148.6

Synthesis of sp-02: sp-02 was synthesized in the same methods as in sp-01 synthesis. 4-*n*-butylphenylacetylene was used instead of phenylacetylene. The yield was 83.5% (0.832 g). ^{1}H-NMR(400MHz, $CDCl_3$); δ 0.84-0.88 (m, 12H), 1.23-1.35 (m, 8H), 1.52-1.61 (m, 8H), 2.53-2.57 (t, 8H), 6.92-6.93 (t, 4H), 7.07-7.09 (dd, 8H), 7.31-7.33 (m, 8H), 7.54-7.57 (dd, 4H), 7.80-7.82 (dd, 4H).

Synthesis of sp-03: sp-03 was synthesized in the same methods as in sp-01 synthesis. triphenylsilylacetylene was used instead of phenylacetylene. The yield was 91.6% (1.32 g). ^{1}H-NMR (400MHz, $CDCl_3$); δ 6.89-6.90 (m, 4H), 7.30-7.32 (m, 4H), 7.32-7.35 (m, 20H), 7.36-7.40 (m, 14H), 7.60-7.64 (m, 26H), 7.78-7.81 (dd, 4H).

Synthesis of 4-Ethynylbiphenyl: 4-Bromobiphenyl (1.9 g, 19.5 mmol) was dissolved in diethylamine (25 ml) and piperidine (12 ml) under argon atmosphere. Copper iodide (114 mg) and dichlorobis(triphenyl-phosphine (210 mg) and triphenylphosphine (78.6 mg) were added to the stirred solution. Trimethylsilylacetylene (3.49 g, 15 mmol) was dropped in and the mixture was stirred at room temperature for 4 h. The formed precipitate of diethylamine hydrobromide was filtered off and washed with ether. The combined filtrates were evaporated under reduced pressure, and the residue was chromatographed on a column of silica gel using hexane/benzene (3/2) to yield 4-trimethysilylethynylbiphenyl as an intermediate. Hydrolysis of this compound (2.7 g, 10.78 mmol) in methanol (30 ml), 1 normal aqueous potassium hydroxide solution (10 ml) was added and the mixture was stirred at room temperature for 1 h. After removal of methanol, the product was extracted with ether and purified by chromatography on alumina to afford a colorless desired material of 4-Ethynyl biphenyl with a yield of 71.9%.

Synthesis of sp-04: sp-04 was synthesized in the same methods as in sp-01 synthesis. 4-Ethynylbiphenyl was used instead of phenylacetylene. The yield of sp-04 was 35.6% (0.364 g). ^{1}H-NMR (400MHz, $CDCl_3$); δ 6.98-6.99 (m, 4H), 7.32-7.34 (m, 4H), 7.39-7.42 (tt, 8H), 7.45-7.47 (m, 8H), 7.50-7.52 (m, 8H), 7.55 (m, 4H), 7.56-7.60 (m, 8H), 7.84-7.86 (dd, 4H).

Synthesis of 1-Ethynylnaphthalene: 1-Ethynylnaphthalene was synthesized in the same methods as in the synthesis of 4-Ethynylbiphenyl. 1-bromonaphthalene was used instead of 4- bromobiphenyl. The yield was 73.7%.

Synthesis of sp-05: sp-05 was synthesized in the same methods as in sp-01 synthesis. 1-Ethynylnaphthalene was used instead of phenylacetylene. The yield was 52.78% (0.484 g). ^{1}H-NMR (400MHz, $CDCl_3$) ; δ 7.11-7.12 (m, 4H), 7.37-7.40 (m, 4H), 7.47-7.50 (m, 4H), 7.51-7.54 (m, 4H), 7.64-7.67 (dd, 4H), 7.72-7.75 (dd, 4H), 7.77-7.82 (td, 8H), 7.92-7.95 (dd, 4H), 8.33-8.35 (dd, 4H).

Synthesis of 4-Ethynyl-N,N-dimethylaniline: 4-Ethynyl-N,N-dimethylaniline was synthesized in the same methods as in the synthesis of 4-Ethynylbiphenyl. 4-bromo-N,N-dimethylaniline was used instead of 4- bromobiphenyl. The yield was 78.3%. ^{1}H-NMR (400MHz, $CDCl_3$); δ 2.97 (s, 6H), 6.59-6.63 (dt, 2H), 7.34-7.37(dt, 2H).

Synthesis of sp-06: sp-06 was synthesized in the same methods as in sp-01 synthesis. 4-Ethynyl-N,N-dimethylaniline was used instead of phenylacetylene. The yield was 39.7% (0.353 g). ^{1}H-NMR (400MHz, $CDCl_3$); δ 2.94 (s, 24H), 6.57-6.59 (d, 8H), 6.9 (m, 4H), 7.27-7.30 (dd, 8H), 7.50-7.53 (dd, 4H), 7.76-7.78 (dd, 4H).

Synthesis of 2,2′,7,7′-tetraformyl-9,9′-spirobifluorene: 2,2′,7,7′-tetrabromo-9,9′-spirobifluorene (1.26 g, 2 mmol) was dissolved in dry toluene (100 ml) under argon atmosphere. To the solution was dropped in n-BuLi (1.6 M in Hexene) (16.08 ml, 25.78 mmol) at room temperature and stirred at 60^{o}C for 4 h. The lithium compound solution was cooled to 0^{o}C, and N-formyl piperidine (4.8 ml, 43.4 mmol) was added, and warmed up to room temperature. The mixture was acidified with diluted HCl solution and stirred for 5 h and the product was extracted into CH_2Cl_2 and purified by column chromatography to afford yellow solid. The yield was 30%. ^{1}H-NMR (400MHz, $CDCl_3$); δ 7.26 (d, 4H), 8.0 (dd, 4H), 8.13 (d, 4H), 9.87 (s, 4H, CHO).

Synthesis of sp-07: Triphenyl phosphonium methyl naphthalene chloride (1.93 g, 4.4 mmol), 2,2′,7,7′-tetraformyl-9,9′-spirobifluorene (0.5 g, 1.1 mmol) was dissolved in 15 ml ethanol and 15 ml $CHCl_3$. To the solution was added sodium ethoxide (0.59 g, 8.8 mmol) dissolved in 15 ml ethanol at room temperature and stirred for 10 h. The resulted precipitate were collected and recrystallized by methanol to afford yellow solid with 76% yield. FT-IR (with KBr); cm^{-1} 2875.6 - 3011.1, 1657.5, 1467.0, 776.4.

2.3. Fabrication and characterization of OLEDs

Multilayer OLEDs were fabricated, with configurations of ITO (180 nm)/PEDOT:PSS (80 nm)/PVK (50 nm)/EML (80 nm)/LiF (1 nm)/Al (100 nm), in which EML represents one of the seven spiroderivatives. The ITO coating from the masked ITO glass was etched out by vapor from HNO_3:HCl (1:3, v/v) solution at 40^{o}C for 5 min, then washed with de-ionized water, acetone, isopropyl alcohol for 15 min sonication in each case, and finally rinsed with de-ionized water to get desired ITO pattern. This cleaned and patterned ITO-coated glass was treated with UV plasma for 1 min to remove any trace of organic material left over from solution cleaning. PEDOT:PSS layer was coated by spin coating from the stock solution at 2500 rpm for 35s and heat treated in an oven at 110^{o}C under vacuum for 1 h. Subsequently, the other layers were also deposited using the same conditions from 1% solution of PVK, and one SBF derivative in chlorobenzene and then LiF and Al were evaporation-deposited sequentially. The thickness was measured using thickness / rate monitor, SQM-160 (Sigma Instruments, USA). The device area was 0.09 cm^2 determined by the overlap area of the anode and cathode.

To characterize intrinsic photo-physical properties, diluted solution samples using pure chloroform solvent were prepared. Concentrations of diluted solutions for synthesized molecules were typically either 10^{-5} M or 10^{-6} M in chloroform solution. Optical densities (OD) were measured by a conventional UV-Vis absorption spectrometer (Cary 100, Varian Co.). PL and PLE spectra of dilute solutions were mainly recorded by a commercial spectrometer (LS-50B, Perkin-Elmer Co.) using quartz cells at room temperature. From these PL and PLE scan spectra, 3 dimensionally correlated PL and PLE maps were obtained for further analysis.

2.4. Computational Method

Time-dependent density functional theory (TD-DFT) is the modification of the stationary DFT to time-dependent potentials and the corresponding electron densities in presence of molecular interaction with an electric laser field. In most of the cases, for calculation of photo-absorption spectra for fixed nuclei, the electric field constitutes a small perturbation which can be treated using linear response theory. Here the ground and the low-lying excited electronic states in SBF derivatives were calculated using the Gaussian 98 package [22]. The energy level of the highest occupied molecular orbital (HOMO) and the energy gap between HOMO and the lowest unoccupied molecular orbital (LUMO) of the compounds were estimated. The 3-21G(d) basis set and the B3LYP with the 6-

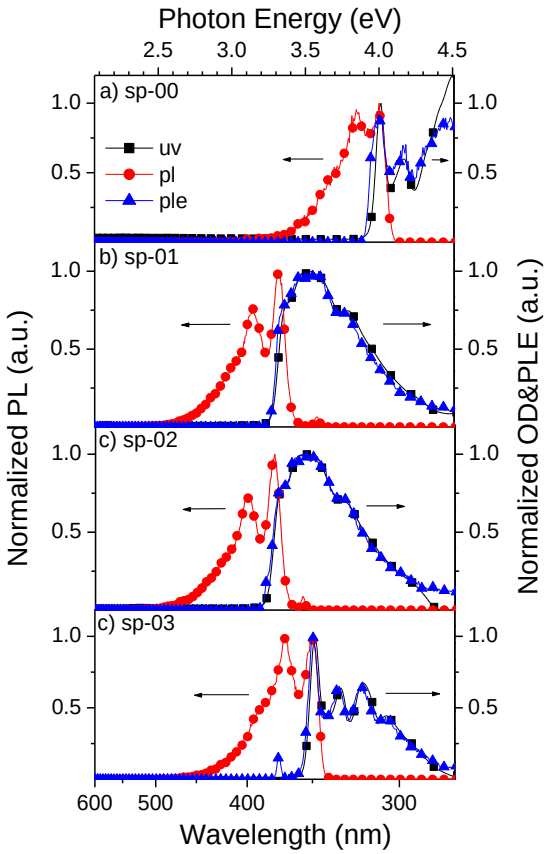

Figure 2a. Selected OD, PL and PLE spectra of sp-00~sp-03 compounds.

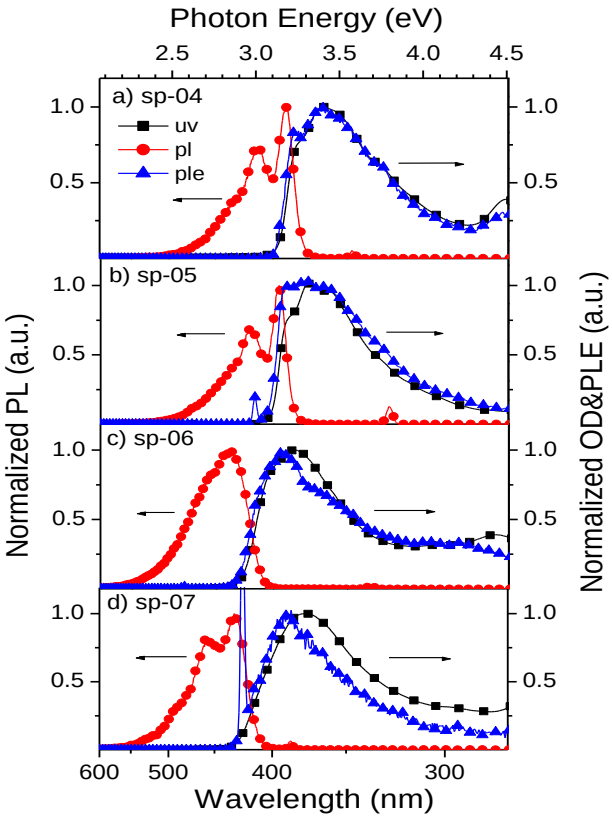

Figure 2b. Selected OD, PL and PLE spectra of sp-04~sp-07 compounds.

31G(d) basis set were used for the geometry optimization and the energy level calculation of the ground state of these compounds, respectively [23]. To obtain the vertical excitation energies of the low-lying singlet and triplet excited states of the SBF derivatives, TD-DFT calculations using the B3LYP functional was performed at the respective ground-state geometry. Typically, the lowest 6 triplet and 6 singlet roots of the non-Hermitian eigen value equations were obtained to determine time-dependent excitation energies (ε), oscillator strength (f) and dominant orbital excitation.

3. Results and Discussion

3.1. Synthesis of different SBF derivatives

All the SBF compounds are synthesized by using a cross coupling reaction with palladium (Pd) catalyst [24] and their synthetic route is shown in Scheme 1. All the operations are carried out under a dry argon atmosphere. The synthesized compounds are characterized by ^{1}H-NMR, ^{13}C-NMR spectra, and those spectra were obtained from BRUKER DPX-400(9.4T) spectrometer (400 MHz), whereas, FT-IR spectrum is obtained from Perkin Elmer Paragon 1000. The different results show the successful formation of different SBF derivatives (as discussed earlier).

3.2. SBF derivatives as effective OLED materials

The UV absorption, PL and PLE spectra of SBF derivatives in diluted solution are shown in Figure 2 and their corresponding λ values are reported in Table 1.

The SBF derivatives in chloroform exhibit UV absorption due to π–π* transition (λ_{max}) at 356, 354, 350, 357, 365, 377, 373 nm for the compounds sp-01 ~ sp-07, respectively, while the PL emission spectrum with two sharp bands for almost all SBF derivatives, (except sp-06 with only one emission at 426 nm) e.g., 398, 376 for sp-01, 397, 377 for sp-02, 376, 352 nm for sp-03 etc., are observed. The presence of vibronic structure in the emission spectrum indicates that the SBF compounds have a rigid and well-defined backbone structure. Since the π-conjugation of the molecular chain is extended by the incorporation of the π-conjugated functional groups so that greater electron delocalization with the mono or biphenyl end groups is possible, consequently the SBF compounds show a substantial red-shift e.g., 36, 32, 30, 37, 45,

Table 1. Maximum wave length (λ_{max}) as measured from UV, PL and PLE measurements.

Sample code	UV λmax (nm)	PL λ_{max} (nm)	PLE λ_{max} (nm)
sp-00	320, 300	325, 320	320, 300
sp-01	356, 342	398, 376	356, 341
sp-02	354, 333	397, 377	353, 342
sp-03	350, 337, 325	376, 352	351, 335, 326
sp-04	357	410, 395	357
sp-05	365	410, 398	365
sp-06	377	426	386
sp-07	373	461, 426	378

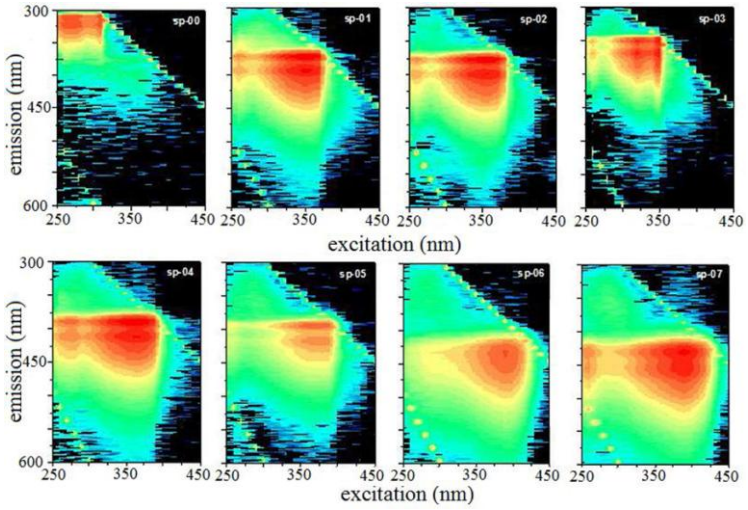

Figure 3. Mapped PL and PLE spectra of different SBF derivatives; slice parallel to the x-axis are the PLE spectra with a specific emission wavelength, and slices perpendicular to the x-axis are the PL spectra with a specific excitation wavelength. The contour lines and the red color (green to blue meaning no emission) are to indicate the PL emission intensity on a logarithmic scale.

57, and 53 nm in UV absorption and 73, 72, 51, 77, 85, 101, 136 nm in PL emission for the compounds sp-01 ~ sp-07, respectively, as compared to the unsubstituted compound, sp-00. Moreover, due to the presence of spiro-fused orthogonal bifluorene segments, which restrict the close packing of the molecular chains and reduce the probability of interchain interactions, the tendency to form aggregates and excimers in SBF film is also less favorable. Thus the PL emission spectra of sp-01 ~ sp-04 compounds are almost identical with a low red-shift (51 ~ 77 nm), whereas the same for the other SBF compounds e.g., sp-05 ~ sp-07 is highly red-shifted (85 ~ 136 nm). Thus the synthesized SBF derivatives showed the PL emission spectra in the range from blue to near-UV range i.e., from 2.7 eV (461 nm) up to 3.5 eV (352 nm) (Table 1). The naphthyl and amine containing derivatives (e.g., sp-05 ~ sp-07) showed a significant deviation in PL, photoluminescence excitation (PLE), and UV-Vis absorption (OD) spectroscopy, indicating their additional photon energy specific to non-radiative decay channels. Mapped PL and PLE spectra of different SBF derivatives show also the same trend (Figure 3). Here the slice parallel to the x-axis are the PLE spectra with a specific emission wavelength, and slices perpendicular to the x-axis are the PL spectra with a specific excitation wavelength. The contour lines and the red color (green to blue meaning no emission) are to indicate the PL emission intensity on a logarithmic scale.

3.3. Molecular orbital of SBF derivatives

The molecular orbital (MO) structures of SBF derivatives using the DFT have been investigated and the contour plots of four HOMOs and two LUMOs of sp-01 and sp-05, as the representative compounds, are shown in Figure 4a, 4b, respectively. The dominant excitations and emissions mainly occur due to the electronic transition among those orbitals. The results of theoretical calculations are summarized in Table 2. It seems that HOMO is formed by the admixing of

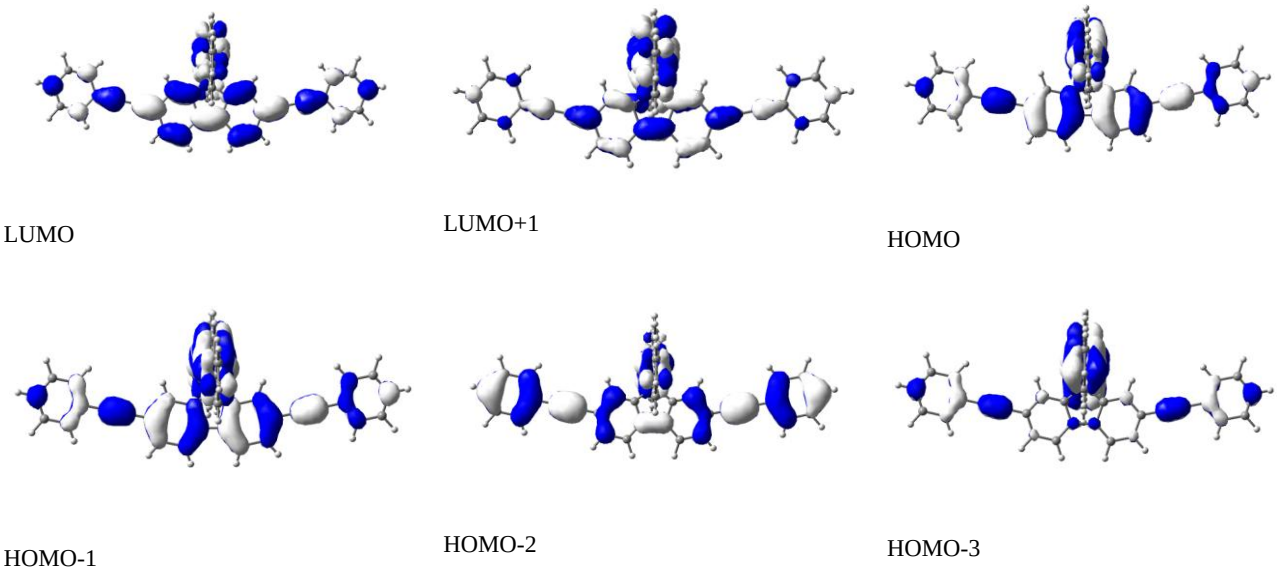

Figure 4a. Contour plots of HOMOs and LUMOs of sp-01 compound.

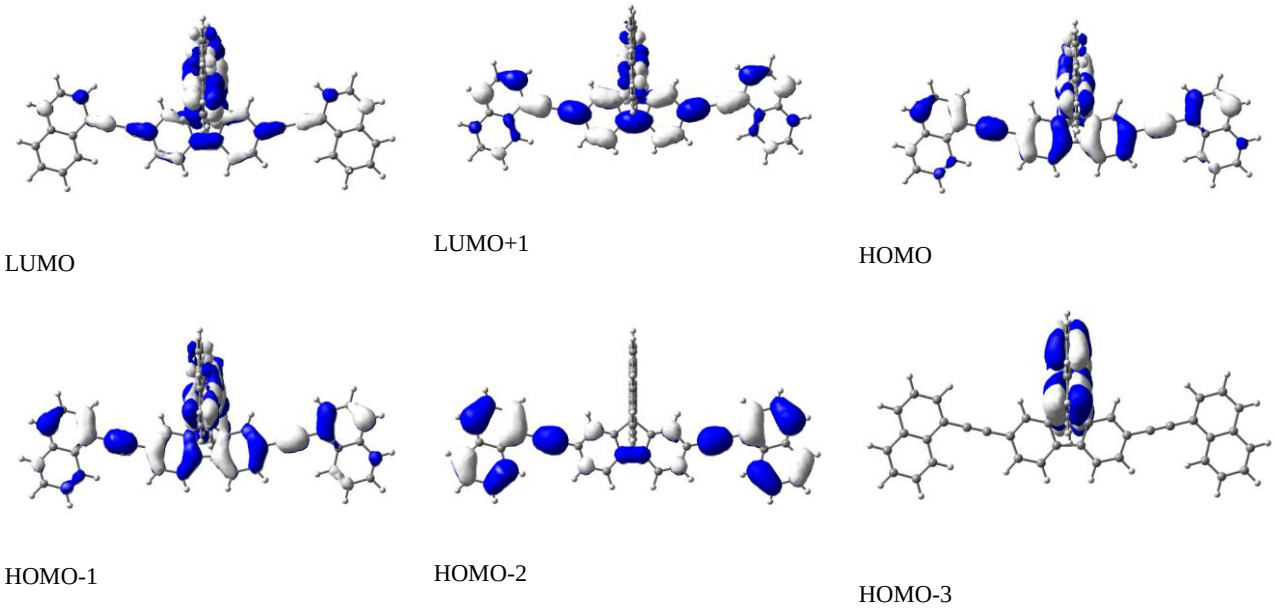

Figure 4b. Contour plots of HOMOs and LUMOs of sp-05 compound.

Table 2. Calculated singlet state Excitation Energies (ε), Oscillator Strengths (f), and Dominant Orbital Excitation from TD-DFT Calculations for two SBF derivatives (e.g., sp-01 and sp-05).

Sample code	Excited state	Excitation energy (ε) (eV)	Wave length (λ) (nm)	Oscillator strength (f)	Dominant orbital excitation (H=HOMO, L=LUMO)
sp-01	S_1	3.085	401.9	0.1788	H → L
	S_2	3.085	401.9	0.1788	H → L+1
	S_3	3,223	384.7	1.8694	H-1 → L
	S_4	3.223	384.7	1.8694	H-1 → L+1
	S_5	3.828	323.9	0.0	H-3 → L+1, H-2 → L
	S_6	3.828	323.9	0.0	H-2 → L+1, H-3 → L
sp-05	S_1	2.878	430.8	0.3358	H → L
	S_2	2.878	430.8	0.3358	H → L+1
	S_3	2.948	420.6	1.6761	H-1 → L+1, H-1 → L
	S_4	2.948	420.6	1.6761	H-1 → L, H-1 → L+1
	S_5	3.375	367.4	0.0	H-2 → L, H-3 → L+1
	S_6	3.375	367.4	0.0	H-3 → L+1, H-2 → L

the p orbitals, however, HOMO-1 and HOMO-2 have rather different characteristics.

3.4. Excitation energy, oscillator strength and dominant orbital excitation as per TD-DFT calculations

The description of time-dependent photo-excitation was incorporated properly into DFT by Runge and Gross [25]. They generalized the Hohenberg-Kohn equations into the time-dependent densities and potentials functions. Though the main application of DFT deals with relatively weak electric fields, e.g. photo-absorption spectra but it can also be used for a small perturbation within linear response theory. Thus it helps in solving the TD-DFT equations i.e., the time domain to dynamically propagate electrons and the nuclei. The TD-DFT theory becomes the most widely used method for calculating electronic excitation energies nowadays. Though it has few limitations in measuring the charge transfer and double excitations energies but the excitation energies using Gaussian-type basis set and plane are found to be almost accurate. The oscillator strength (f), a dimensionless quantity to express the strength of the transition from one quantum state to another of a molecule, is dependent on excitation energy (ε). Figure 5 shows that with the increase of ε there is an increase in f initially, then it shows a maxima and decreases finally with further increase of ε. This is because at the initial stage the number of electron in the ground state will be more and after almost all the electron being excited no more electrons will be available for further excitation. The variation of maximum oscillator strength (f_{max}) with excitation energy for the SBF derivatives are presented in Figure 6, which is the characteristic f values of the different SBF derivatives. TD-DFT calculation was employed to examine the low-lying singlet and triplet states of the SBF compounds and the results are shown in Table 2. The vertical excitation energies for the lowest triplet and singlet states were calculated at the optimized structure for the ground states. For each of the triplet and singlet excitations, a dominant excitation is achieved among several minor excitations. All these

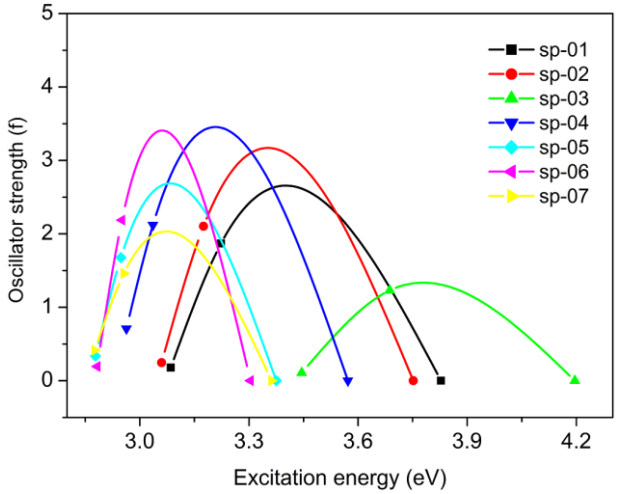

Figure 5. Oscillator strength (*f*) of SBF compounds at three different excitation energies.

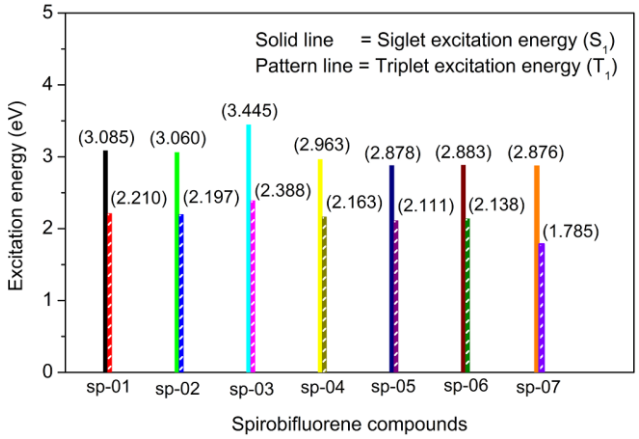

Figure 6. Maximum oscillator strength (f_{max}) with respective excitation energy of different SBF derivatives.

excitations correspond to electron transfer from the two HOMOs to virtual MOs. This characteristic is very similar to that of SBF compounds with only a difference in excitation energy. The wavelengths of the lowest 6 singlet and triplet states calculated by the TD-DFT method are marked "S" and "T" (Figure 7). In the higher region of wavelength, there commonly exist small and elongated tails that are always shown in absorption spectra of SBF compounds. It is speculated that those tails are due to the lower triplets such as T_1 and T_2 [26, 27]. These triplets having lower energies are very important because their transition states are related to the luminescence. Also, they play a role in setting the criterion that predicts the position of the luminescent wavelength through the comparison. Here the measured value mostly agrees with calculated value. From the TD-DFT calculation, the value of the lowest triplet excitation of sp-01 is 570 nm, which is 250 nm longer than that of sp-00. The emission wavelength of sp-05 is about 410 nm in the region of violet to blue color. From the calculation of the electronic population of some HOMOs and LUMOs, it is predicted that an extended conjugation length promising intensified emissive efficiency will exist in the electronic transition of SBF compounds.

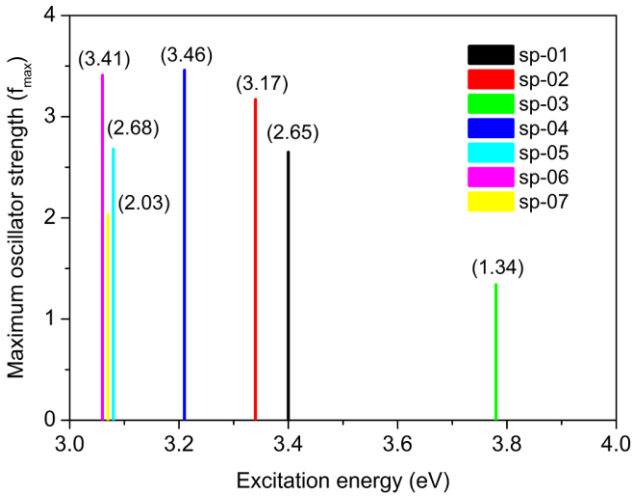

Figure 7. Lowest singlet state (S_1) and triplet state (T_1) excitation energies of different SBF derivatives.

4. Conclusions

A series of SBF derivatives containing different π-conjugated functional groups were synthesized using a cross coupling reaction with palladium (Pd) catalyst at inert atmosphere. The synthesized SBF derivatives showed PL emission spectra in the range from blue to near-UV range i.e., from 461 nm to 352 nm. The naphthyl and amine containing derivatives (e.g., sp-05 ~ sp-07) showed a significant deviation in their PL, PLE and UV-Vis absorption (OD) spectra compared to the base compound (i.e., sp-00), indicating their additional photon energy specific to non-radiative decay channels. The TD-DFT based calculation showed that the excitation energies (ε), oscillation strength (*f*) and dominant orbital excitation are almost similar to that obtained experimentally. The results also demonstrated that the synthesized materials could be used as promising organic blue light-emitting diode (OLED) materials.

References

1. Jianping Lu, Qinde Liu, Jianfu Ding, Ye Tao, Synth. Met. 158 (2008) 95.
2. Sunyoung Sohn, Keunhee Park, Donggeun Jung, Hyoungsub Kim, Heeyeop Chae, Hyunmin Kim, Junsin Yi, Mann-ho Cho, and Jin-hyo Boo, Jpn. J. Appl. Phys. 46 (2007) L461.
3. Shuai Wang, Yunqi Liu, Xuebin Huang, Gui Yu, and Daoben Zhu, J. Phys. Chem. B 107 (2003) 12639.
4. Bernard Geffroy, Philippe le Roy, Christophe Prat, Polym. Int. 55 (2006) 572.
5. Myeon-Cheon Choi, Youngkyoo Kim, Chang-Sik Ha, Prog. Polym. Sci. 33 (2008) 581.
6. Jeong-Ik Lee, Hye Yong Chu, Hyoyoung Lee, Jiyoung Oh, Lee-Mi Do, Taehyoung Zyung, Jaemin Lee, and Hong-Ku Shim, ETRI J. 27 (2005) 2.
7. Leni Akcelrud, Prog. Polym. Sci. 28 (2003) 875.
8. Andrew C. Grimsdale and Klaus Müllen, Bridged Polyphenylenes from polyfluorenes to ladder polymers, Advances in Polymer Science, Heidelberg, Berlin, Vol. 212 (2008).
9. Huei-Jen Su, Fang-Iy Wu, and Ching-Fong Shu, Macromolecules 37 (2004) 7197.
10. Francesca Cecchet, Giulia Fioravanti, Massimo Marcaccio, Massimo Margotti, Leonardo Mattiello, Francesco Paolucci,

Stefania Rapino, and Petra Rudolf, J. Phys. Chem. B 109 (2005) 18427.
11. Jeong-Ik Lee, Hyoyoung Lee, Jiyoung Oh, Hye Yong Chu, Seong Hyun Kim, Yong Suk Yang, Gi Heon Kim, Lee-Mi Do, Taehyoung Zyung, Curr. Appl Phys. 3 (2003) 469.
12. Ya-Hsien Tseng, Ping-I Shih, Chen-Han Chien, Ajay Kumar Dixit, and Ching-Fong Shu, Macromolecules 38 (2005) 10055.
13. Kreyenschmidt. M., Klaemer G., Fuhrer. T., Ashenhurst. J., Karg. S., Chen. W. D., Lee. V. Y., Scott. J. C., Miller. R. D., Macromolecules 31 (1998) 1099.
14. Kla¨rmer. G., Lee. J. I., Lee. V. Y., Chan. E., Chen. J. P., Nelson. A., Markiewicz. D., Siemens, R., Scott. J. C., Miller. R. D., Chem. Mater. 11 (1999) 1800.
15. Xia. C., Advincula. R. C., Macromolecules 34 (2001) 5854.
16. Jacob. J., Zhang. J., Grimsdale. A. C., Mu¨llen. K., Gaal. M., List. E. J. W., Macromolecules 36 (2003) 8240.
17. Wu. F. I., Dodda. R., Jakka. K., Huang. J. H., Hsu C. S., Shu. C. F., Polymer 45 (2004) 4257.
18. Tang. H. Z., Fujiki. M., Zhang. Z. B., Torimitsu. K., Motonaga. M., Chem. Commun. 23 (2001) 2426.
19. Lin. W. J., Chen. W. C., Wu. W. C., Niu. Y. H., Jen. A. K. Y., Macromolecules 37 (2004) 2335.
20. Chou. C. H., Hsu. S. L., Dinakaran. K., Chiu. M. Y., Wei. K. H., Macromolecules 38 (2005) 745.
21. R. Wu, J. Org. Chem. 61 (1996) 6906.
22. Frisch. M. J., et al., Gaussian 98, Revision A.9, Gaussian Inc., Pittsburgh, PA (1988).
23. Young Hee Lee, Young Sik Kim, Mol. Cryst. Liq. Cryst. 462 (2007) 149.
24. K. M. Jones, T. M. Keller, Polymer 36 (1995) 187.
25. E. Runge and E. K. U. Gross., Phys. Rev. Lett. 52 (1984) 997.
26. Nam. E. J., Kim. J. H., KIm. B., Kim. S. M., Park. N. G., Kim. Y. S., Kim. Y. K., Ha. Y. K., Bull. Chem. Soc. Jpn. 77 (2004) 751.
27. Park. N. G., Choi. G. C., Lee. J. E., Kim. Y. S., Curr. Appl Phys. 5 (2005) 79.

Cite this article as:

R. N. Jana *et al.*: **Organic Light Emitting Diode (OLED) materials from spirobifluorene derivatives.** *Phys. Express* 2014, **4:** 2

Structural, magnetic and transport properties of $Gd_{0.7}Ca_{0.3}MnO_3$ and $Gd_{0.7}Ca_{0.3}CrO_3$: A comparative study

Sudipta Pal[a,*], Esa Bose[b]

[a] *Department of Physics, University of Kalyani, Kalyani, Nadia, W.B. 741235, India*
[b] *Department of Engineering Physics, B. P. Poddar Institute of Management & Technology, Kolkata -700052, India*

[*] *Author for Correspondence: S. Pal, email: sudipta.pal@rediffmail.com*
Received 26 Mar 2013; Accepted 17 May 2013; Available Online 17 May 2013

Abstract

The gadolinium-based perovskites $Gd_{0.7}Ca_{0.3}MnO_3$ (GCMO) and $Gd_{0.7}Ca_{0.3}CrO_3$ (GCCO) have been investigated and compared through their structural, magnetic and transport properties. It was found that both the compounds have completely different magnetic ground states but have similar crystallographic structures and exhibit negative magnetization at low temperatures in the field cooled (FC) process. Isothermal (2 K) magnetization values under applied magnetic field of 55 kOe recorded for GCMO and GCCO are 2.54 μ_B and 3.57μ_B, respectively. These low values indicate the antiparallel alignment of Mn / Cr and Gd sublattices. The conductivity data follows small polaron hopping (SPH) model for GCMO throughout the measured temperature range (5 - 400 K), while it shows a transition from SPH to variable range hopping (VRH) mechanism at low temperatures in case of GCCO.

Keywords: Crystallographic structure; Negative magnetization; Polaron hopping

1. Introduction

The study of the rare-earth transitional metal (RTM) oxides with perovskite structure (with general formula ABO_3 where A and B denote the rare-earth and transitional metal respectively) is an interesting area of basic condensed matter physics research. Apart from the technological point of view, unconventional magnetic ground states are observed in these compounds mainly due to the competing interactions of the internal degrees of freedom like spin, charge or orbital momentum. A large number of studies have been done to elucidate the nature of spin, charge or orbital ordering or the exchange interactions of the transition metal ions which affect the physical properties (i. e transport, magnetization etc.) of these compounds. Recently the magnetodielectric property in these materials has also attracted a lot of attention.

One of the interesting behavior in these RTM oxides is anomalous negative magnetization occurring in the antiferromagnetic state. It has been found in the $LaVO_3$ compound that the magnetic moments orient opposite to the applied magnetic field below a certain temperature T_t ($T_t < T_N$, T_N is the Neel temperature) [1]. The symmetry of $LaVO_3$ changes at T_t from the orthorhombic space group Pbnm to monoclinic $P2_1c$. In the monoclinic phase V ions have two crystallographically inequivalent sites. Since La has no magnetic moment, a sign reversal of the net magnetization is supposed to be due to the different temperature dependencies of the individual V-sub lattice magnetization. In case of other RTM oxides, however the magnetic moment of the rare-earth also can play an important role on the magnetic properties through the complex interplay between 3d and 4f orbitals [2, 3]. The ordering of rare-earth ions within the internal field of transition metal ion results in a sign reversal of the net magnetization in the compounds like $La_{1-x}Gd_xMnO_3$ [2], $La_{1-x}Pr_xCrO_3$ [4] or $Re_{1-x}Ca_xMnO_3$ [5-8] (where Re=Nd, Gd, Dy) at low temperatures (below antiferromagnetic Neel temperature T_N). Such behavior has not been observed in the undoped $LnCrO_3$ or $LnMnO_3$ (where Ln is the rare earth) except $GdCrO_3$ [9]. In non-stoichiometric $NdMnO_{3+\delta}$ however similar magnetization property has been observed [10].

It is observed that in the $Gd_{1-x}Ca_xMnO_3$, the substitution of Gd by Ca drastically changes the magnetic properties of $GdMnO_3$ and the FC magnetization becomes negative at low temperature [6,11]. So this effect in the solid solutions may have a correlation with the weakening of anisotropy around the rare-earth arising from the substitution of the magnetic cation by a non-magnetic one [i.e. $Ca^{2+}(4s^0)$]. Further the substitution of Mn with Cr has shown interesting effect in magnetic properties [12]. To elucidate the nature of the internal field effect of transition metal on the rare-earth we have studied and compared the magnetic properties of GCMO and GCCO. The changes observed in the magnetic properties through changes in the structure and thus exchange interactions between rare-earth sub-lattice and transition metal sub lattice are reported in this paper.

2. Experimental Details

High quality polycrystalline samples were prepared in air via solid state reaction method. The precursors Gd_2O_3, CaO and MnO_2 or Cr_2O_3 were mixed in stoichiometric ratio. They were heated at 800°C for 24 h. Then the powder was pelletized and fired in air at 1500° C for 6 to 18 h to obtain single phase. The room temperature crystal structure was determined by powder X-ray diffraction (*XRD*) measurements using CuK_α radiation (Philips diffractometer). The lattice parameters were obtained from the Rietveld analysis of the XRD data using FULLPROF suite [13]. Quantum Design magnetometers were used to collect the AC susceptibility and DC magnetization data.

Table 1. Lattice parameters and selected inter-atomic distances for GCMO and GCCO obtained by Rietveld refinement of the XRD data. Both the samples show the same space group *Pnma*.

GCMO

Cell parameters (Å)		distances (Å)		angles(^{0})	
a	5.5553(3)	Mn-O1x2	2.079(6)	Mn-O1-Mn	129.11(6)
b	7.5077(4)	Mn-O2x2	2.004(2)	Mn-O2-Mn	151.98(2)
c	5.3334(3)	Mn-O2x2	1.965(2)		
cell volume	222.452(2) (Å^3)				

GCCO

Cell parameters (Å)		distances	(Å)	angles(^{0})	
a	5.4647(2)	Cr-O1x2	1.953(3)	Cr-O1-Cr	151.20(3)
b	7.5661(2)	Cr-O2x2	1.967(3)	Cr-O2-Cr	152.35(5)
c	5.3131(1)	Cr-O2x2	1.957(9)		
cell volume	219.678(7)(Å^3)				

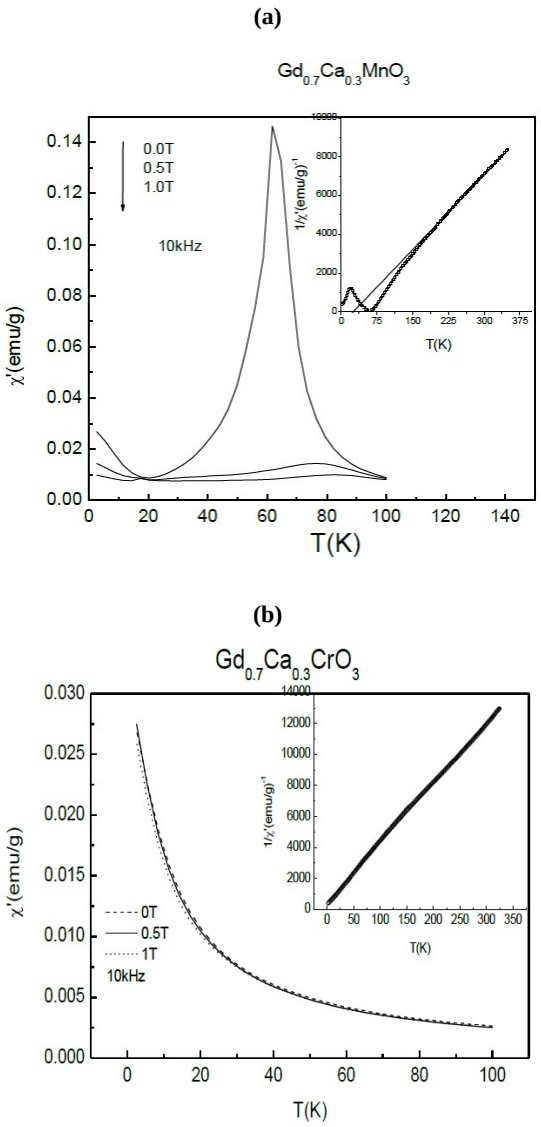

Figure 1. A.C susceptibility in different external dc field 0T, 0.5T, and 1T for (a) GCMO (b) GCCO. Inset :(a) and (b) plot of inverse of A.C susceptibility vs temperature. Straight line corresponds to the Curie-Weiss fit.

3. Results and Discussion

The X-ray diffraction investigation revealed that GCMO and GCCO are pure phases that crystallize in an orthorhombic structure (space group *Pnma*). The lattice parameters and Mn-O interatomic distances are given in Table 1 for comparison. Even if the accuracy of the oxygen positions obtained from the *XRD* is not very high, the value of the bond lengths and angles clearly indicate that the CrO_6 octahedra is much regular in GCCO than the MnO_6 octahedra in GCMO, in agreement with the Jahn-Teller character of Mn^{3+}. Figure 1 shows the temperature variation of the real part of ac susceptibility (χ'_{ac}) for the GCMO and GCCO compounds. χ'_{ac} data were collected using a weak driving field of rms (root-mean-square) strength 10 Oe with and without applied dc field. In case of GCMO, χ'_{ac} *(T)* shows a maximum around 61 K without applied dc field. On the other hand the value of χ'_{ac} monotonically increases with the decrease of temperature in GCCO throughout the temperature range (2.5-350 K). However zero field cooled (ZFC) and field cooled (FC) dc magnetization bifurcate (Figure 2) at 130 K. This temperature is inferred as the antiferromagnetic Neel temperature [4].

To investigate the magnetic transition in detail, the ac susceptibility data for both compounds have also been taken in presence of external DC field 0.5T and 1T. In case of GCCO the applied field has almost no effect on χ'_{ac}. In contrast, the sharp maximum in χ'_{ac} of GCMO is completely depressed with the application of dc field. This indicates the existence of antiferromagnetic ordering which is destroyed with the application of external magnetic field. Above 200 K the susceptibility data can be fitted (inset of Figure 1) to the Curie-Weiss law: $\chi = \mu^2_{eff} / [8(T-\Theta)]$ with $\mu^2_{eff} = 69.68\mu^2_B$ and Curie-Weiss temperature are deduced as Θ = 24 K for GCMO and $\mu^2_{eff} = 46.01\mu^2_B$ and Θ=-11 K for GCCO. Positive value of Curie-Weiss temperature in GCMO indicates ferromagnetic interactions but negative value in GCCO shows an antiferromagnetic background.

The temperature dependence of dc magnetization for the GCMO and GCCO are presented in Figure 2. The magnetization was measured at both ZFC and FC modes at an external field of 50 Oe. In ZFC mode the sample was first cooled down to the lowest temperature (5 K) and magnetization was measured during heating. In FC-cooling,

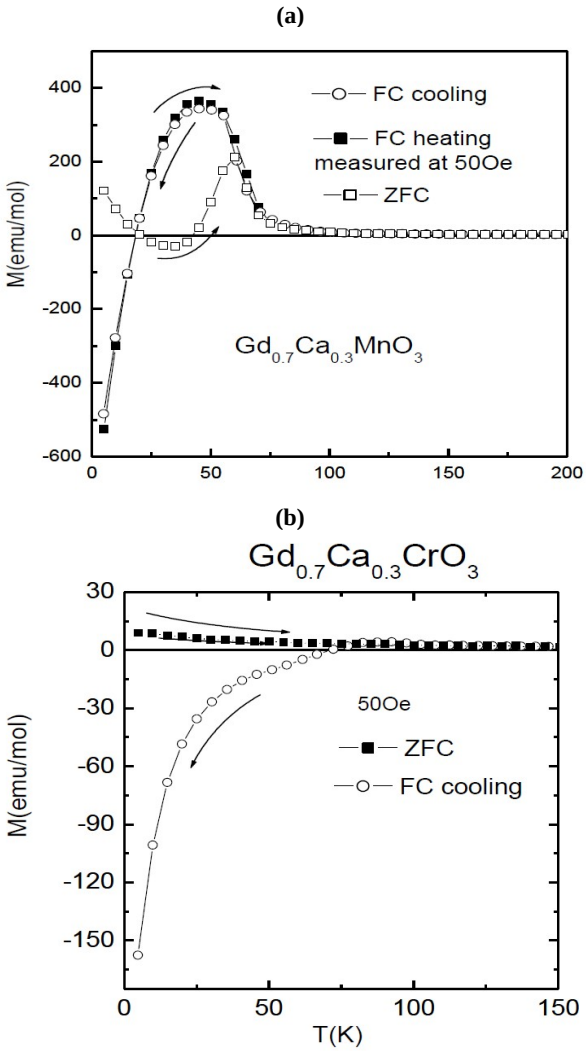

Figure 2. ZFC/FC cycles of (a) GCMO (b) GCCO.

the magnetization data were recorded while cooling the sample. In case of FC heating the sample was first cooled down to lowest temperature (5 K) under a small field (50 Oe) and then measured in heating in the same field. With the decrease of temperature, the ZFC magnetization in GCMO increases up to a temperature 61 K then decreases and shows a minimum with a small negative value (-30 emu/mol) and reaches ~100 emu/mol at 4 K. Similar value has been observer earlier [11]. It is noted that in the ZFC data negative magnetization is observed in some temperature range but this trend is not observed in the AC susceptibility data. This may be due to the fact that AC susceptibility data has been taken at high frequency (10 kHz). At this high frequency the AC moment of the sample does not follow along the DC magnetization curve due to dynamic effects in the sample. In the ZFC magnetization curve of GCCO no such anomaly is observed. A large difference is observed in the ZFC and FC mode for both compounds below a magnetic ordering temperature (130 K for GCCO and 61 K for GCMO). A cusp-like maximum in the FC mode in GCMO indicates a spontaneous ferromagnetism that results from the manganese spins [1, 2]. But this spontaneous ferromagnetism almost disappears in GCCO which is supposed to be due to the absence of ferromagnetic exchange interaction between Cr ions. However similar nature of negative magnetization in the FC process in these two compounds can be understood

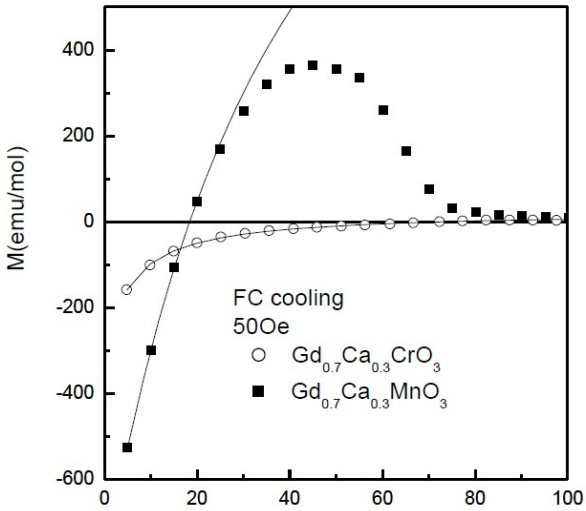

Figure 3. Replotted FC cooling curve. The solid line is the fit of the expression $M=M_{\text{Mn or Cr}} + C_{\text{Gd}}(H_{\text{int}}+H_{\text{ext}}) /(T-\theta)$.

considering the polarization of Gd spins in the internal field of Mn or Cr ion. It has been proposed [2- 4] that the Gd spins are polarised antiparallel with respect to the ferromagnetic (FM) component of the manganese spins via the antiferromagnetic coupling of the Gd spins to the Mn moments. The antisymmetric exchange interactions between the ions according to the Dzyaloshinsky-Moriya rule could be the explanation of this type of coupling [14]. With decreasing temperature, the Gd spins become aligned in the field of manganese moments, yielding to a negative magnetization when the polarization of Gd exceeds the FM component of Mn. Similar phenomenon can be considered in case of Cr. But the difference is that the negative magnetization value at 5 K of GCMO is 3 times larger than the value of GCCO measured in the same applied field (50 Oe). This indicates the difference between the internal field created by the Cr and Mn sublattices.

From the theoretical point of view the negative magnetization M can be approximated by the expression [15] $M = M_{\text{Mn or Cr}} + C_{\text{Gd}}(H_{\text{int}}+H_{\text{ext}}) /(T-\theta)$, where the spontaneous magnetization $M_{\text{Mn or Cr}}$ and the internal field H_{int} result from the Mn or Cr moments and the external field is H_{ext}=50 Oe. C_{Gd} is the Curie constant of the Gd moments and θ is a fitting parameter resemble with the Weiss temperature. The fitted curves have been plotted in Figure 3. The values of H_{int}, obtained from the best fit, are 20 kOe and 390 Oe for GCMO and GCCO, respectively. In $La_{1-x}Gd_xMnO_3$ [2] the obtained value of H_{int} was of the order of 8 kOe. In GCMO the large value of H_{int} might be the result of ferromagnetic double exchange interaction between Mn^{3+} and Mn^{4+} ions. On the other hand double exchange is not observed between Cr ions and the value of H_{int} is much smaller in GCCO. In Figure 4 the magnetization is shown as a function of field measured at 2 K. The magnetization was measured after cooling the samples in zero field at the desired temperature. With the increase of magnetic field the magnetization (M) increases but does not reach saturation value which is ascribed as a canted magnetic ordering [2]. At higher fields elevated value of M is observed for GCCO. The ferromagnetic-like M-H curve in case of GCMO indicates Mn^{3+}-O-Mn^{4+} ferromagnetic double exchange interaction. Under an applied magnetic field 55 kOe, the magnetization value reaches 2.54 μ_B and 3.57 μ_B, for

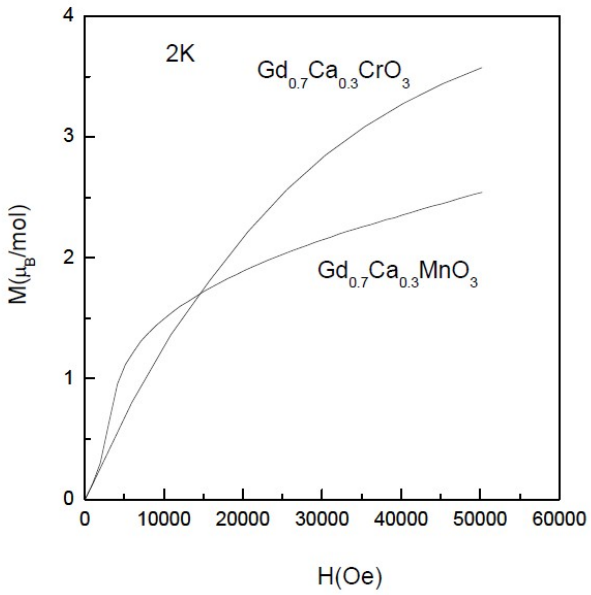

Figure 4. M-H curves for GCMO and GCCO measured at 2K. The magnetization was measured after cooling under zero field.

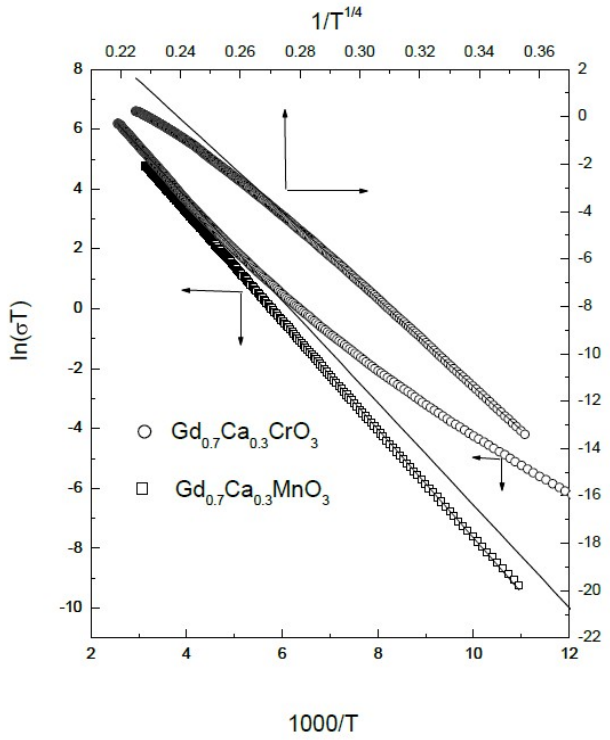

Figure 5. *ln* (σT) vs *1000/T* curve (left and bottom axis) for GCMO and GCCO. Plot of *ln*(σ) vs $1/T^{1/4}$ (right and top axis) for GCCO. Straight line corresponds to the linear fit.

GCMO and GCCO respectively. The saturation magnetization per mole of GCMO expected from Gd^{3+} s= 7/2, l=0 is $\mu = gs\mu_B$ =2× (0.7 ×7/2) μ_B = 4.9μ_B, while high-spin manganese gives spin only value μ =2× [0.7×2 (from Mn^{3+}) 0.3×3/2 (from Mn^{4+})]μ_B=3.7μ_B. Assuming the Gd and Mn sublattice are antiparallel, the net magnetization can be predicted as 4.9-3.7=1.2μ_B . However the large field dependent magnetization observed at 2 K can be understood as the two sublattices are canting away from the antiparallel arrangement. Similarly in GCCO large magnetization value 3.57 μ_B is obtained at 55 kOe compare to the expected 2.2μ_B [4.9 (from Gd^{3+}) -2.7 (from $Cr^{3+}$and Cr^{4+})].

A comparison of the temperature dependence of the conductivity of GCMO and GCCO gives an idea about the different electronic ground states. Both systems are semiconducting in nature and the resistivity monotonically decreases with temperature. The temperature dependent conductivity of GCMO can be well fitted with $\sigma = \sigma_0 \exp(-E/k_BT)$ in the entire temperature range (5-325 K) of our measurements, which indicates small polaron hopping conduction (Figure 5). In case of GCCO a deviation is observed from the small polaron hopping conduction behavior around 160 K. Below this temperature the conductivity data is better described by $\sigma_0\exp(T_0/T)^{1/4}$, which is commonly attributed to variable range hopping [16]. So in GCCO the conduction mechanism changes from the small polaron hopping to variable range hopping conduction with lowering temperature. The variable range hopping conduction at low temperature also indicates a disordered semiconducting system. However the activation energy (E) estimated from the fitting of the conductivity data with $\sigma = \sigma_0 \exp(-E/k_BT)$ shows that the E is almost of the same order (156.45 meV for GCMO and 147.35 meV for GCCO respectively) for the two compounds.

4. Conclusions

In summary, crystallographic, magnetic and transport properties of GCMO and GCCO have been studied and compared. Useful comparison between these two compounds allowed us to draw important conclusion on the interplay between the magnetic contribution of both rare-earth and transition metal sublattice. Both compounds have similar crystallographic structures and exhibit negative magnetization in the FC process. However it has been shown that the two compounds have completely different magnetic ground state. The positive value of Curie-Weiss temperature in GCMO indicates ferromagnetic interactions but the negative value in GCCO shows an antiferromagnetic background. Resistivity measurements show that the systems are semiconducting in nature and resistivity monotonically decreases with temperature. In GCCO the conduction mechanism changes from the small polaron hopping to variable range hopping conduction with lowering temperature (below 160 K) indicating a disordered semiconducting system.

Acknowledgements

The corresponding author (SP) acknowledges the financial support of this work partially from the DST-PURSE and DST FAST TRACK project No- SR/FTP/PS-101/2010 Govt. of India.

Referrences

1. A. V. Mahajan, D. C. Johnston, D. R. Torgeson, and F. Borsa, Phys. Rev. B. 46 (1992) 10966.
2. J. Hemberger et al, Phys. Rev. B. 70 (2004) 02441.
3. O Peña, M Bahout, D Gutierrez, P Duran, C Moure, Solid State Sci. 5 (2003) 1217.
4. K. Yoshii, A. Nakamura, Y. Ishii, and Y. Morii, J. Solid State Chem. 162 (2001) 84.

5. I O Troyanchuk, V A Khomchenko, G M Chobot, A I Kurbakov, A N Vasil'ev, V V Eremenko, V A Sirenko, M Yu Shvedun, H Szymczak and R Szymczak, J. Phys.: Condens. Matter 15 (2003) 8865.
6. O. Pena, M. Bahout, K. Ghanimi, P. Duran, D. Gutierrez and C. Moure, J. Mater. Chem. 12 (2002) 2480.
7. C. A. Nordman, V. S. Achutharaman, V. A. Vas'ko, P. A. Kraus, A. R. Ruosi, A. M. Kadin, and A. M. Goldman, Phys. Rev. B. 54 (1996) 9023.
8. M Bahouta, O Pena, D Gutierrez, P Duran, C Moure, Solid State Commun. 122 (2002) 561.
9. K. Yoshii, J. Solid State Chem. 159 (2001) 204.
10. F. Bartoloméa, J. Herrero-Albillos, L. M. García, J. Bartolomé, N. Jaouen and A. Rogalev, J. Appl. Phys. 97 (2005) 10.
11. G. Jeffrey Snyder, C. H Booth, F. Bridges, R. Hiskes, S. DiCarolis, M. R. Beasley and T. H Geballe, Phys. Rev. B. 55 (1997) 6453.
12. S. Biswas, M H Khan, S Pal, E Bose, J. Magn. Magn. Mater. 328 (2013) 31.
13. J. Rodrigues-Carvajal, Physica B 192 (1993) 55.
14. I Solovyev, N Hamada and K Terakura, Phys. Rev. Lett. 76 (1996) 4825.
15. A. H. cook, D. M. Martin and M. R wells, J. Phys. C: Solid State Phys. 7 (1974) 3133.
16. S. Pal, A. Banerjee, E. Rozenberg and B. K. Chaudhuri, J. Appl. Phys. 89 (2001) 4955.

Cite this article as:

Sudipta Pal *et al.*: **Structural, magnetic and transport properties of $Gd_{0.7}Ca_{0.3}MnO_3$ and $Gd_{0.7}Ca_{0.3}CrO_3$: A comparative study.** *Phys. Express* 2014, **4:** 3

Nonlinear optical response of asymmetric monolayer graphene

Vipin Kumar*, Enamullah, Girish S. Setlur

Department of Physics, Indian Institute of Technology Guwahati, Guwahati, Assam, 781039, India

Author for Correspondence: Vipin Kumar, email: k.vipin@iitg.ernet.in
Received 17 Mar 2013; Accepted 23 Apr 2013; Available Online 23 Apr 2013

Abstract

We study Rabi oscillations (RO) in case of asymmetric monolayer graphene (asymmetry between sub-lattices makes it a gapped system) in two different cases – resonance (conventional RO) and off-resonance (anomalous RO). In an earlier work, we have shown that graphene exhibits anomalous RO far from resonance, attributable to the pseudo-spin degree of freedom of graphene. The anomalous Rabi frequency (ARF) is typically much smaller than the conventional one. In case of asymmetric graphene, the ARF differs from the symmetric value by an additive constant equal to twice the gap parameter. This shift is found to be numerically one to two orders of magnitude larger than the ARF for symmetric graphene. However, the conventional Rabi frequency (CRF) is not significantly modified as a result of asymmetry.

Keywords: Asymmetric graphene; Optical Bloch equations; Rabi oscillations

1. Introduction

Graphene [1] is a new class of material and is only one atom thick, tightly packed, flat carbon sheet in two dimensions, in which carbon atoms are arranged in a honeycomb lattice structure. The honeycomb lattice is made up of two in-equivalent sublattices named A and B. In graphene, the charge carriers are massless Dirac fermions obeying the pseudo-relativistic massless Dirac equation (massless Dirac-Weyl equation), in which the Fermi velocity of charge carriers ($v_F \sim 10^6$ m/s) plays the role of speed of light. The model possesses pseudo-spin instead of real spin - pseudo spin projections referring to sublattices A and B [2]. Graphene Hamiltonian is symmetric under A $\leftrightarrow$ B, showing degeneracy at the Dirac points where the tip of two bands touch one another. If we introduce any kind of asymmetry [3-5] in the graphene Hamiltonian between A and B sublattices i.e. this may occur due to presence of corrugated substrate, this lifts the degeneracy and opens up a band gap at the Dirac points and the charge carriers become massive. Due to massive charge carriers, the energy-momentum dispersion relation becomes parabolic for both electron and hole instead of being linear at Dirac points. Rabi oscillation is a nonlinear optical phenomenon well known in the context of two level atomic systems in quantum optics [6] and also in conventional semiconductors [7]. Semiconductors are similar in some sense to two level atomic systems, the difference being that in semiconductors, levels are replaced by bands. Therefore it is important to investigate such phenomena in graphene where the bands are linear instead of parabolic and unlike semiconductors, graphene possesses a pseudospin degree of freedom. There are several papers on the phenomenon of Rabi oscillations in conventional semiconductors. Using optical Bloch equations, H. S. Brandi *et al.* [8] performed a theoretical analysis of the damping of Rabi oscillations in semiconductor systems. They also calculated the photocurrent and matched their data to the experimental data [9]. The short time semiconductor response with respect to resonant high intensity excitations is studied in [10]. They have calculated the excitation polarization in the coherent limit and found that the polarization of bright exciton exhibits the Rabi oscillations, whereas the polarization of dark exciton is identically zero. Other works have also described the phenomenon of Rabi oscillations in semiconductors [11-13]. The nonlinear optics of graphene is a developing subject in condensed matter physics. In the work of X. Yao *et al.* [14], the linear and nonlinear optical response of graphene in a strong magnetic and optical field is discussed. They show that the system possesses an extremely high nonlinearity. B. Dora *et al.* [15] describes the phenomenon of Rabi oscillations in Landau quantized graphene. Nonlinear optics of graphene is also described in few other papers on this topic [16-18].

The main results of this paper are the prediction of anomalous Rabi oscillations with a frequency offset by the asymmetry parameter. This offset is found to be numerically one to two orders of magnitude larger than the ARF found in our earlier work related to symmetric graphene [19] and is therefore easily detected as the intercept of the plot between ARF and the conventional Rabi frequency. However, the conventional Rabi frequency is modified negligibly as a result of asymmetry.

2. Bloch equations for asymmetric monolayer graphene

The low energy part of asymmetric monolayer graphene Hamiltonian [1-4] is a 2×2 matrix and can be written as follows:

$$H = v_F \begin{pmatrix} \varepsilon & p_x + ip_y \\ p_x - ip_y & -\varepsilon \end{pmatrix} \quad (1)$$

where v_F is the Fermi velocity of carriers and ε is the sub-lattice space asymmetry between A and B sublattices. Due to

sublattice space asymmetry the energy spectrum of monolayer graphene is no more linear but becomes parabolic near the Dirac points with energy eigenvalues, $E=\pm\sqrt{v_F^2\,|p|^2+\varepsilon^2}\approx\pm\left(\varepsilon+v_F^2\,|p|^2/(2\varepsilon)\right)$. A semi-classical approximation is used to derive the Bloch equations for asymmetric monolayer graphene. An in-plane electric field has been applied to graphene sheet through a complex vector potential, $A_c(t)=A_c(0)e^{-i\omega t}$, which couples to the graphene sheet in Coulomb gauge $\left(\vec{\nabla}\cdot\vec{A}=0\right)$ using the minimal coupling prescription, $p\rightarrow p-e/c\;A$. In second quantization, the Hamiltonian for asymmetric monolayer graphene can be then written as given below:

$$H=\sum_{\vec{p}}\begin{bmatrix} v_F\left(p_+-A_c^*(t)\right)\,c_A^\dagger\left(\vec{p},t\right)c_B\left(\vec{p},t\right)+\text{h.c.} \\ +\varepsilon\left(c_A^\dagger\left(\vec{p},t\right)c_A\left(\vec{p},t\right)-c_B^\dagger\left(\vec{p},t\right)c_B\left(\vec{p},t\right)\right)\end{bmatrix} \tag{2}$$

where $c\,(c^\dagger)$ are the annihilation (creation) operators on sub lattice site A and B and vice-versa, $p_+=p_x+ip_y$ and the third term appears due to asymmetry between sublattice A and B. Following a process explained in an earlier work [19], we can easily write the Bloch equations as given below:

$$i\partial_t n_{diff}\left(\vec{k},t\right)=2v_F\begin{bmatrix}\left(k_+-A_c^*(0)e^{i\omega t}\right)\,p\left(\vec{k},t\right) \\ -\left(k_--A_c(0)e^{-i\omega t}\right)\,p^*\left(\vec{k},t\right)\end{bmatrix} \tag{3}$$

$$i\partial_t p\left(\vec{k},t\right)=v_F\left(k_--A_c(0)e^{-i\omega t}\right)n_{diff}\left(\vec{k},t\right)-2\varepsilon\,p\left(\vec{k},t\right) \tag{4}$$

where, $k_\pm=k_x\pm i\,k_y$, $A_c(0)=e/c\left(A_x(0)-i\,A_y(0)\right)$

Equations (3) and (4) are called the optical Bloch equations for asymmetric monolayer graphene.

3. Solution of Bloch equations

3.1. The off resonance case $\left(\omega>>\omega_R \text{ and } \omega>>2E\right)$

In this section, we discuss how to solve the Bloch equations in the off resonance case. However, there is a special case k = 0 where we can solve the Bloch equations exactly. Inserting k = 0 and taking the ansatz of the form $p\left(\vec{0},t\right)=p'\left(\vec{0},t\right)e^{-i\omega t}$ and doing a straightforward calculation, we may easily write the solution of these equations as follows:

$$n_{diff}\left(\vec{0},t\right)=1+\frac{4\,v_F^2\left|A_c(0)\right|^2}{\left(2\varepsilon+\omega\right)^2}\,\text{Cos}\left(\Omega t\right) \text{ and}$$

$$p\left(\vec{0},t\right)=\frac{\left(e^{i\Omega t}-1\right)}{\left(2\varepsilon+\omega\right)}v_F\,A_c(0)e^{-i\omega t}$$

where, $\Omega\approx\omega+\Omega_{ARF}$ and $\Omega_{ARF}=2\varepsilon+2\omega_R^2/\omega$, which shows the offset oscillation. More elaborately, if $\omega_R=0$, still there will be the oscillations and these oscillations are exclusively due to the asymmetry in graphene system absent in symmetric graphene. The main point here is that the asymmetry has the remarkable effect on the anomalous Rabi oscillations whereas conventional Rabi frequency is minutely affected by the asymmetry parameter.

In the general case when $k\neq0$ we used the procedure of an earlier work [19], which means we may write the solutions as,

$$p_+\left(\vec{k},t\right)=-\frac{v_F\,A_c^*(0)}{\left(2\varepsilon+\omega\right)}\,n_s\left(\vec{k},t\right) \text{ and}$$

$$p_-\left(\vec{k},t\right)=-\frac{2\,v_F^2\,p_-\,A_c(0)}{\omega\left(2\varepsilon-\omega\right)}\,p_s\left(\vec{k},t\right)$$

$$p_s\left(\vec{k},t\right)=n_s\left(\vec{k},0\right)\begin{bmatrix}-\omega_{R\varepsilon}/\left(4v_F\,k_+\right)\text{Cos}\left(\Omega_{ARWA}t\right) \\ -i\Omega_{ARWA}/\left(2v_F\,k_+\right)\text{Sin}\left(\Omega_{ARWA}t\right)\end{bmatrix}$$

$$\omega_{R\varepsilon}=\left(2\omega_R^2/\omega+2\varepsilon\right) \text{ and}$$

$$\Omega_{ARWA}=2\sqrt{\left(v_F|k|\right)^2+\omega_{R\varepsilon}^2/4}$$

where Ω_{ARWA} is the anomalous Rabi frequency in case of asymmetric monolayer graphene. Also,

$n_s\left(\vec{k},0\right)=2\left(v_F|k|\right)^2/\left(|E|\;\omega_{R\varepsilon}\right)$,

$p_0\left(\vec{k}\right)=-v_F\,k_-/\left(2|E|\right)$ are the equilibrium values of number density and polarization density respectively. The slow part of current density of asymmetric monolayer graphene in frequency domain is given as follows:

$$\vec{j}_s(\omega')=-\frac{\xi\,\tau\,e\,A\,z_A^*\vec{\sigma}_{AB}}{\omega_{R\varepsilon}\left(2\varepsilon+\omega\right)v_F}\left(\sqrt{\omega'^2-4\left(\varepsilon+\omega_R^2/\omega\right)^2}\right)\omega'$$

for $\omega'>2\left(\varepsilon+\omega_R^2/\omega\right)$ and $\vec{j}_s(\omega')$ is zero otherwise.

3.2. The resonant case (ω ≈ 2E)

To solve the Bloch equations in resonance case, we apply RWA method [5, 6]. Mishchenko [20] has already studied the phenomenon of RO in case of small detuning Δ. Mishchenko uses real vector fields while we have used complex vector fields. We learn in undergraduate classes that the two approaches are equivalent. This is so only when the equations involved are linear. For the Rabi problem at hand they are not equivalent hence the Rabi frequency we get has a different expression from what Mishchenko obtains.

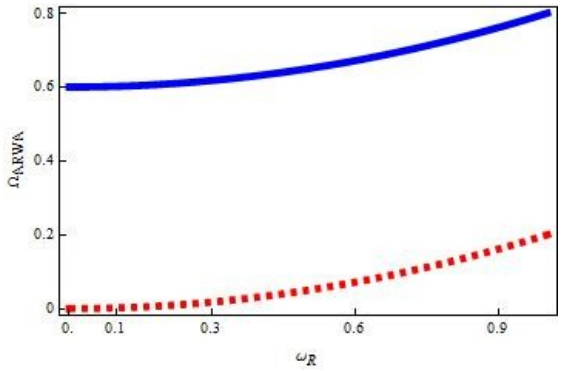

Figure 1. This figure depicts the variation of ARF Ω_{ARWA} vs ω_R for the case of symmetric graphene (red dashed curve) and asymmetric graphene (blue solid curve). A large intercept on the vertical axis is seen in the asymmetric case.

$$\Omega_{RWA}=\sqrt{(\omega - 2E)^2 + \omega_R^2\left(1+\varepsilon(\varepsilon - 2E)/E^2\right)}$$

where $E=\sqrt{v_F^2\,|p|^2+\varepsilon^2}$ is the energy eigenvalue of asymmetric monolayer graphene. Mishchenko [20] gets an additional factor (Sin) in the formula for the conventional Rabi frequency whereas in our approach, the formula for the conventional Rabi frequency is independent of this factor. The reason for this discrepancy has already been pointed out above.

4. Numerical analysis

Here we provide numerical estimates of the various frequency scales that are encountered in this work. They are listed in the table below. The largest is the external frequency followed by the asymmetry parameter and then the conventional Rabi frequency and the smallest is the anomalous Rabi frequency. We have used an electric field of $E_{max}=250$ kV/cm, typical in high power lasers in arriving at this table. One may see easily that the anomalous Rabi frequency $\Omega_{ARF}=\left(2\omega_R^2/\omega + 2\varepsilon\right)$ is significantly different from the symmetric case. However, the CRF $\Omega_{CRF}=\omega_R\left(1- 2\varepsilon/\omega\right)$ is not modified significantly.

Energy	Unit (eV)
$\hbar 2\omega_R^2/\omega$	2.7×10^{-4}
$\hbar\omega_R$	0.013
ε	0.26
$\hbar\omega$	1.24

5. Results and Discussion

In this section, we pictorially describe the main results of the present work. The plots and their captions are self-explanatory.

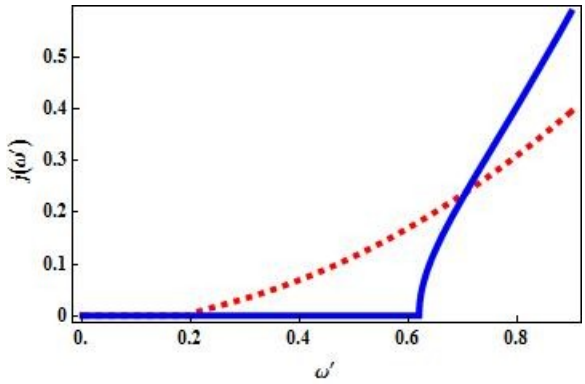

Figure 2. This figure depicts the variation of slow part of current density $j(\omega')$ (ARWA) vs ω' for the case of symmetric graphene (red dashed curve) and asymmetric graphene (blue solid curve). Note that the threshold in case of asymmetric graphene is shifted (horizontal intercepts exaggerated for clarity).

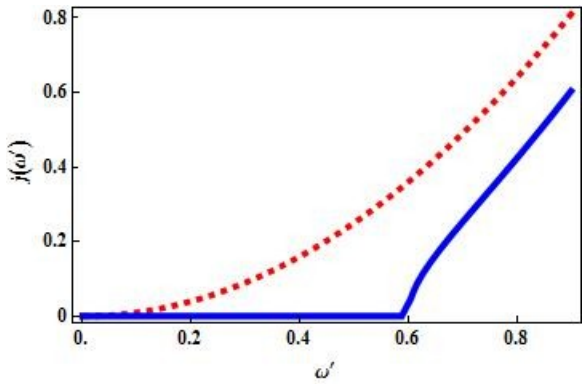

Figure 3. This figure depicts the variation of slow part of current density $j(\omega')$ (ARWA) vs ω' for the case of symmetric graphene (red dashed curve) and asymmetric graphene (blue solid curve) when $\omega_R=0$. In this case, the current density shows no threshold behaviour for symmetric graphene, whereas for asymmetric graphene the threshold behaviour is still present and may be characterized by the parameter 2ε.

6. Conclusions

The main results of this paper are the prediction of anomalous Rabi oscillations with a frequency offset by the asymmetry parameter. This offset is found to be numerically one to two orders of magnitude larger than the ARF found in our earlier work related to symmetric graphene and is therefore easily detected as the intercept of the plot between ARF and the conventional Rabi frequency. However, the conventional Rabi frequency is modified negligibly as a result of asymmetry. Even in the absence of an external optical field, the observed current density in the off resonance case exhibits a threshold behaviour at the offset frequency - a feature absent in symmetric graphene.

References

1. K. Geim, K. S. Novoselov, Nat. Mater. 6 (2007) 183.
2. H. Castro Neto, F. Guinea, N. M. R. Peres, K. S. Novoselov, A. K. Geim, Rev. Mod. Phys. 81 (2009) 109.

3. S. Y. Zhou, G. H. Gweon, A. V. Fedorov, P. N. First, W. A. de Heer, D. H. Lee, F. Guinea, A. H. Castro Neto, A. Lanzara, Nat. Mater. 6 (2007) 770.
4. A. Varykhalov, D. Marchenko, J. Sanchez-Barriga, M. R. Scholz, B. Verberck, B. Trauzettel, T. O. Wehling, C. Carbone, O. Rader, Phys. Rev. X 2 (2012) 041017.
5. S. Russo, M. F. Craciun, T. Khodkov, M. Kashino, M. Yamamoto, S. Tarucha, arxiv:1105.2479v1 [cond-mat.mes-hall, 7 May 2011].
6. R. W. Boyd, Nonlinear Optics, Elsevier, Singapore (2009) pp. 301-316.
7. H. Haug and S. W. Koch, Quantum Theory of Optical and Electronic Properties of Semiconductors, World Scientific, Singapore (2004) pp. 211-215.
8. H. S. Brandi, A. Latge, Z. Barticevic, L E. Oliveira, Solid State Commun. 135 (2005) 386.
9. A. Zrenner, E. Beham, S. Stufler, F. Findeis, M. Bichler, G. Abstreiter, Nature 418 (612) 2002.
10. M. Erementchouk, M. N. Leuenberger, Phys. Rev. B. 78 (2008) 075206.
11. A. Schülzgen, R. Binder, M. E. Donovan, M. Lindberg, K. Wundke, H. M. Gibbs, G. Khitrova, N. Peyghambarian, Phys. Rev. Lett. 82 (1999) 2346.
12. K. Schuh, J. Seebeck, M. Lorke, F. Jahnke, Appl. Phys. Lett. 94 (2009) 201108.
13. J. Förstner, C. Weber, J. Danckwerts, A. Knorr, Phys. Rev. Lett. 91 (2003) 127401.
14. X. Yao, A. Belyanin, Phys. Rev. Lett. 108 (2012) 255503.
15. Dóra, K. Ziegler, P. Thalmeier, M. Nakamura, Phys. Rev. Lett. 102 (2009) 036803.
16. K. L. Ishikawa, Phys. Rev. B. 82 (2010) 201402.
17. A. R. Wright, X. G. Xu, J. C. Cao, C. Zhang, Appl. Phys. Lett. 95 (2009) 072101.
18. E. Hendry, P. J. Hale, J. Moger, A. K. Savchenko, S. A. Mikhailov, Phys. Rev. Lett. 105 (2010) 097401.
19. Enamullah, Vipin Kumar and Girish S. Setlur, Physica B 407 (2012) 4600.
20. E. G. Mishchenko, Phys. Rev. Lett. 103 (2009) 246802.

Cite this article as:

Vipin Kumar *et al.*: **Nonlinear optical response of asymmetric monolayer graphene.** *Phys. Express* 2014, **4:** 4

Silicon aids quasi - planar arrangement of gold clusters

Seema Gautam[a], Neetu Goel[b], Rajiv Bhandari[c,*], Keya Dharamvir [a,*]

[a] *Department of Physics & Centre of Advanced Studies in Physics, Panjab University, Chandigarh-160014, India*
[b] *Department of Chemistry & Centre of Advanced Studies in Chemistry, Panjab University, Chandigarh-160014, India*
[c] *Post Graduate Govt. College, Sector 11, Chandigarh- 160011, India*

[*] *Authors for Correspondence: Keya Dharamvir, email: keya_dv@yahoo.co.in*
Rajiv Bhandari, email: rbhandari293@gmail.com
Received 18 Nov 2012; Accepted 13 Apr 2013; Available Online 13 Apr 2013

Abstract

Clusters of pure gold comprising of more than 14 atoms do not adopt planar arrangement. However on doping with a single Si atom, quasi-planar structures of Au_nSi clusters (with n = 14 – 16) show up as low energy isomers, though it may not be the stable ground state. The calculations have been performed within the framework of DFT with spin-polarized generalized gradient approximation (GGA) implemented with Gaussian-03 code. In all low energy isomers of Au_nSi we find a Si-Au dangling unit sitting over the quasi-planar arrangement of gold atoms. Therefore planar arrangements of gold atoms is possible beyond the size n=14 with the aid of silicon. A pentagonal unit of gold atoms attached with a Si-Au dangling unit can only exist in the presence of other neighboring gold atoms to support the planarity or quasi-planarity. Mulliken charge distribution analysis reveals that a symmetric charge distribution accompanies this unusual planarity of gold cluster beyond size n=14.

Keywords: Density Functional Theory (DFT); Gold Clusters (Aun); Si doped gold clusters (Au_nSi)

1. Introduction

It is well-known from a large number of previous studies [1-3] that free Au_n clusters exhibit a variety of fascinating geometrical structures, e.g., planar ones up to about N = 12, anionic cages for N = 16–18, bulk-fragment pyramidal structures for N = 19–23, possible tubular cages at N = 24 and 26 and gold fullerene at N = 32. The distinct structures of gold clusters are believed to be caused by relativistic effects. Relativistic effects in Au atoms play a key role in planarity (neutral and anionic gold clusters favour 2D structures up to n=14), effectively shrinking the size of S orbitals and causing a large s-d hybridization, so that in-plane overlap between 5d orbitals increases. Apart from unusual preference for planar structures, the interest in gold clusters is due to its various applications in molecular electronic devices, catalysts, and medical diagnostics. The question naturally arises whether we can retain the planarity of gold cluster beyond the size n=14 by doping. Up to now no theoretical study is available about the planarity of gold cluster beyond n=14.

The doped Au_n, especially the bimetallic ones, have been the focus of research since doping can offer chemical versatility by tuning its structural, electronic, and catalytic properties. Out of the large number of experimental and theoretical studies carried out on doped gold clusters only a few have focused on doping of non-transition metal atom, in particular Si atom, while majority involve transition metal atoms. Although Au and Si do not form any stable alloys, the Au-Si interface has been studied extensively owing to its importance in microelectronics.

The current work explores the possibility of planar arrangement of Au_n clusters (n=14, 15 and 16) that otherwise seems to be impossible, by doping with Si atoms. This can be of immense use in nano electronic devices. Charge distributions have also been observed through Mulliken population analysis (MPA) and we find that electron density at silicon decreases with increased coordination causing the electropositive character of the silicon center to increase.

2. Computational Details

The calculations have been performed within the framework of DFT with spin-polarized generalized gradient approximation (GGA) [4] implemented with Gaussian-03 code [5].

Geometry optimizations of several isomeric structures were performed using linear combination of molecular orbital (LCAO-MO) based approach using gradient-corrected exchange-correlational functional of Perdew and Wang (termed as PW91) [6]. The accuracy and reliability of the functional form PW91 for small gold clusters has been verified by earlier studies [4]. Previously reported global minima of Au_n clusters were used to obtain equilibrium geometries of Au_nSi clusters. The initial geometries were prepared by placing a Si atom as a cap on the possible sites of low energy 2D isomer of Au_{14} cluster. Beyond this, low lying isomers for n=15, 16 is generated by extending the quasi-planar isomer of $Au_{14}Si$. There are many other isomers on the potential energy surface. However, we have considered only those which represent planar arrangement of Au atoms including either a tetrahedral local arrangement or a square planar one involving the Si dopant atom. No attempt has been made to find the global minima of Au_nSi (n = 14, 15 and 16) clusters. The main focus of this study is to show the possibility of attaining planar arrangement of Au atoms with the help of Si atom up to size n=16. The triplet-valence basis set 6-311 G (d) was used for Si atoms, while a relativistic frozen core potential with 19-electron valence basis set SDD [7] was adopted for Au atoms. Under this approximation, the $5s^2$ $5p^6$ $5d^{10}$ $6s^1$ outermost valence electrons of the Au atom are described through the

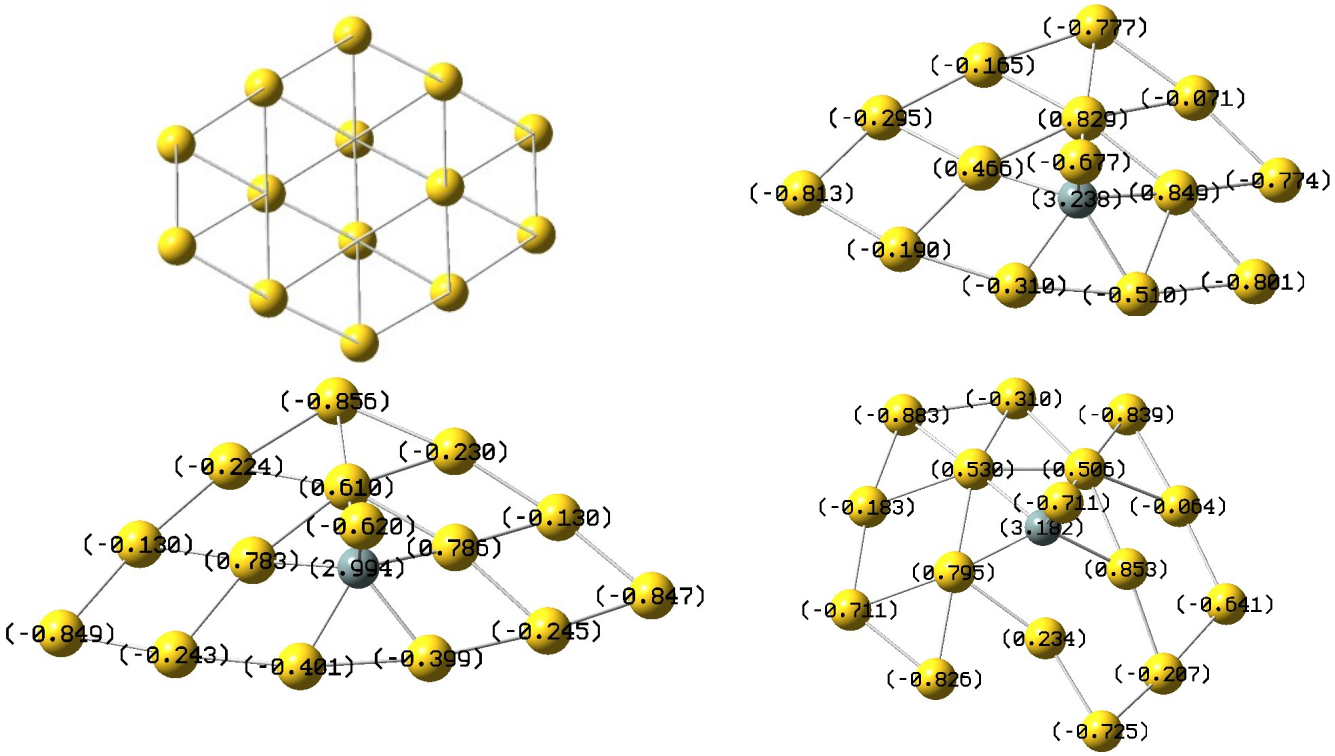

Figure 1. Equilibrium geometries of $Au_{14}$and Au_n Si (n=14-16) clusters.

corresponding SDD basis set. Frequency analyses have also been performed to ensure that there is no imaginary frequency.

3. Results and Discussion

The good agreement of our results on gold dimer i.e., Au_2 cluster with both experimentally and theoretically reported values [8, 9] establishes faith in the accuracy of the computational method and the reliability of atomic pseudo-potentials used in this work. The optimized bond length (BL) and binding energy per atom (E_b/n) of AuSi, found to be 2.28 Å and 1.64 eV/atom respectively, also nicely agree with previously reported experimental and theoretical values [10]. The lowest energy structure of low lying isomers of Au_{14} and Au_nSi (n= 14, 15 and 16) clusters are displayed in Figure 1.

It shows the quasi planar isomer $Au_{14}Si$, confirmed as a stable isomer by frequency analysis. This is a low energy isomer but not the global minimum. Si is penta-coordinated to five gold atoms and is sp^3d hybridized owing to dominant Au-Si interactions. It has a dangling Au-Si unit on the planar surface of 13-atom gold clusters. For $Au_{15}Si$, the input was generated by adding one gold atom to the bridging gold site of $Au_{14}Si$ which yielded the stable structure on optimization. It has a similar dangling Au-Si unit on the surface. The quasi planar isomer $Au_{16}Si$ was obtained by optimization of the structures generated by extending the sheet of $Au_{15}Si$ by adding gold atom. This $Au_{16}Si$ isomer too has a Au-Si dangling unit and the dopant Si atom is almost a part of the quasi-planar sheet. Mulliken charge distribution analysis (MPA) shows that charge distribution is very symmetric i.e. All first neighbours of silicon acquire +ve charge and all second neighbours acquire -ve charge. We also find that electron density at silicon decreases with increased coordination causing the electropositive character of the silicon center to increase.

4. Conclusions

In this work we have reported the possibility of planar arrangement of Au atoms with the aid of Si atom. All the isomers investigated here may not be the lowest energy configuration but are the genuine minima on the potential energy surface. In all three optimized geometry of Au_nSi, a pentagon of gold atoms attached with a dangling Au-Si unit is present. Interestingly, this pentagonal unit with Au-Si dangling cannot exist independently. It can only exist in the presence of neighbors to support the planarity or quasi-planarity. Mulliken charge distribution analysis reveals that symmetric charge distribution is responsible for unusual planarity of gold cluster beyond size n=14.

Acknowledgments

S. G. thanks Council of Scientific and Industrial Research (CSIR), New Delhi for a research fellowship.

References

1. X. Xing, B. Yoon, U. Landman, J. H. Parks, Phys. Rev. B. 74 (2006) 165423.
2. M. P. Johansson, D. Sundholm, J. Vaara, Angew Chem. Int. Ed. 116 (2004) 2732, Angew. Chem. Int. Ed. 43 (2004) 2678.
3. X. Gu, M. Ji, S. -H. Wei, X. –G. Gong, Phys. Rev. B. 70 (2004) 205401.
4. P. Perdew, Orbital-Dependent Functionals, In: P. Ziesche and H. Eschrig (Eds.), Electronic Structure of Solids ’91, Akademie Verlag, Berlin (1991).
5. M. J. Frisch, G. W. Truks, H. B. Schlegelet et. al., Gaussian-03, Revision C.3, Gaussian Inc., Pittsburgh, PA (2003).
6. J. P. Perdew, J. A. Chevary, S. H. Vosko, K. A. Jackson, M. R. Pederson, D. J. Singh, C. Fiolhais, Phys. Rev. B. 46 (1992) 6671.

7. M. Dolg, U. Wedig, H. Stoll, H. Preuss, J. Chem. Phys. 86 (1987) 866; P. Schwerdtfeger, M. Dolg, W. H. E. Schwarz, A. G. Bowmaker, P. D. W. Boyd, Ibid. 91 (1989) 1762.
8. R. C. Weast (Ed.), CRC Handbook of Chemistry and Physics (49th ed.), CRC, Ceveland, OH (1969).
9. X. Li, H. Wang, X. Yang, Z. Zhu, Y. Tang, J. Chem. Phys. 126 (2007) 084505.
10. J. J. Scherer, J. B. Paul, C. P. Collier, A. O'Keeffe, R. J. Saykally, J. Chem. Phys. 103 (1995) 9187.

Cite this article as:

Seema Gautam *et al.*: **Silicon aids quasi - planar arrangement of gold clusters.** *Phys. Express* 2014, **4:** 5

X-ray diffraction and confocal fluorescence microscopy studies on the effect of cholesterol on phospholipid membranes

Sanat Karmakar[a,*], V. A. Raghunathan[b]

[a] *Department of Physics, Jadavpur University, 188 Raja S. C. mallick Road, Kolkata, 700 032, India*
[b] *Raman Research Institute, Shadashivanagar, Bangaluru, 5600 80, India*

[*] *Author for Correspondence: Sanat Karmakar, email: sanat@phys.jdvu.ac.in*
Received 30 Mar 2013; Accepted 13 Jun 2013; Available Online 13 Jun 2013

Abstract

We have studied the influence of cholesterol on the bilayer properties of phospholipid membranes using small angle x-ray scattering and laser scanning confocal fluorescence microscopy. We have obtained a cholesterol induced modulated (P_β) phase in oriented multilayers of dipalmitoyl phosphatidylcholine (DPPC)-cholesterol mixtures at 98% relative humidity at intermediate cholesterol concentrations. The P_β phase, which is distinct from the usual ripple ($P_{\beta'}$) phase, is absent in unoriented samples in excess water. However, we observe enhanced swelling of the bilayers in this part the phase diagram. This results is also supported by the fact that giant unilamellar vesicles (GUVs) at small cholesterol concentration (< 10 mol%) show significant shape fluctuations, indicating softening of bilayers in the presence of cholesterol. However, interestingly smaller GUVs (diameter < 20 μm) are almost spherical in shape and show dark irregular domains on a bright background, indicating the coexistence of gel and fluid phases.

Keywords: Model membrane; Small angle x-ray diffraction; Fluorescence microscopy

1. Introduction

Lipid bilayer is the structural basis of all biological membranes [1]. It is a two dimensional fluid in which the distribution of cholesterol is known to be inhomogeneous. Cholesterol rich domains, called "rafts", have been proposed to exist in these membranes [2-6]. Such lipid domains in the membranes are suspected to play vital role in many cellular events such as protein trafficking, signal transduction etc. Only indirect evidence in support of raft is the formation of detergent resistant membranes (DRM) [7]. Compositional analysis reveals that DRM contains phospholipids, cholesterol and GPI anchored proteins, which are then believed to be components of rafts.

Model membranes composed of ternary mixtures of a saturated lipid (DPPC), an unsaturated lipid (DOPC) and cholesterol have been widely used to mimic the behaviour of biomembranes [8-11]. The coexistence of two fluid phases referred to as the liquid ordered (l_o) and liquid disordered (l_d), seen in these systems below the chain melting transition (T_m) of the saturated lipid, is believed to be relevant for the formation of rafts in plasma membranes [9, 12]. The l_o phase is known to be rich in saturated phospholipid, such as DPPC and cholesterol and this phase resembles rafts in composition. Therefore, PC-cholesterol mixture is an excellent model system to study the structure and phase behaviour of lipid-cholesterol membrane in order to obtain some insights into the rafts.

The importance of lipid-cholesterol membranes has led to a large number of experimental as well as theoretical studies on the thermotropic phase behavior, degree of chain ordering and lateral diffusion of this system [13-16, 18-22]. Spectroscopic studies surmise that there is a two phase region at cholesterol concentrations (X_c) in the range $5 < X_c < 25$ above the main transition of the phospholipid. These two phases are believed to be cholesterol rich l_o and cholesterol poor l_d phases [15, 17, 23, 24]. However, diffraction as well as fluorescence microscopy studies have not shown the coexistence of l_o and l_d phases in these binary mixtures [25, 26]. Recently molecular dynamic simulation has been employed to investigate the effect of cholesterol on water permeability and solute partitioning into phospholipid bilayer [27, 28]. they have reported locally disordered membrane areas of low cholesterol content, rather than the ordering averaged over the entire membranes. However, they did not find any phase separation in the binary lipid-cholesterol mixtures.

Fluorescence microscopy studies on giant unilamellar vesicles (GUVs) made up of binary lipid-cholesterol mixtures do not exhibit fluid-gel phase separation. Shape deformations and thermal shape fluctuations of GUVs have been observed in both single component and binary lipid mixtures near the main transition [29, 30]. These shape transformations at various temperatures have been explained theoretically using membrane elasticity models with various levels of sophistication [31, 32].

In this paper we present our results of x-ray diffraction from both oriented and unoriented samples of lipid-cholesterol membranes. Unoriented samples basically provide information regarding phase behaviour in excess water. Fluorescence microscopy observations of GUVs made from DPPC-cholesterol mixtures are also presented here. These provide complementary information to the results obtained from diffraction study.

2. Experimental Details

Dipalmitoyl phosphatidylcholine (DPPC), was purchased from Fluka and cholesterol from Sigma and were used without any further purification.

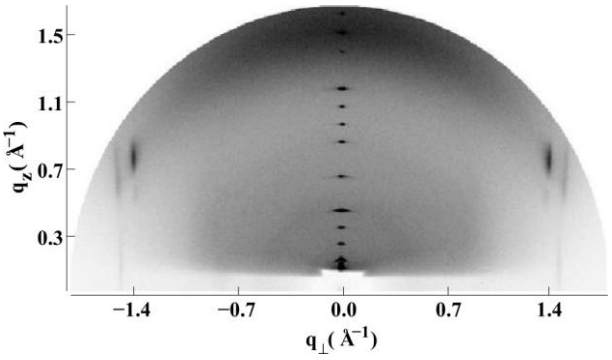

Figure 1. Diffraction pattern of the gel phase of DPPC.

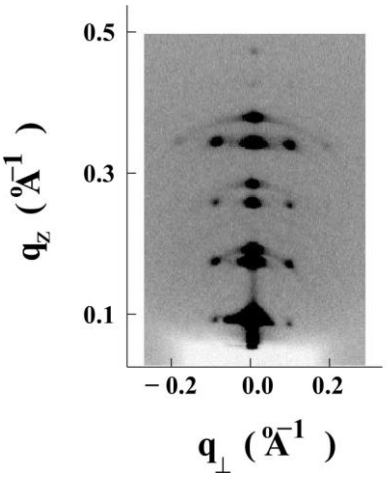

Figure 2. Small angle region of diffraction pattern showing the coexistence of gel and modulated phase (X_c = 10 mol% , T = 10 ^{0}C, RH= 98 ±2%, q scales are approximate and are intended only as guides.

2.1. Small angle x-ray scattering

Appropriate amounts of lipid and cholesterol were dissolved in chloroform. Samples were deposited on glass substrates and then the solvent was allowed to evaporate. To remove all traces of the solvent, samples were kept for ~ 12 hours inside a desiccator which is evacuated. Samples were hydrated for a couple of days in a water saturated atmosphere. This results in well aligned multilayers of phospholipid-cholesterol mixtures. Fully hydrated samples were transferred to a sealed chamber for experiments. X-rays from a rotating anode generator (*Rigaku, Ultra 18X*) were tangential to the substrate. CuK_α radiation (1.54 Å) was selected using a flat graphite crystal monochromator (*Huber*). Temperature of the samples was varied by circulating water from a water bath (*Julabo*) to an accuracy of ± 0.1 °C. The probe of a thermo-hygrometer (*Testo 610*) was introduced into the sample chamber to monitor temperature and relative humidity close to the sample. Diffraction patterns were recorded on a 2D Image plate detector (*Marresearch*). All samples were first heated from room temperature to a temperature above the main transition and then cooled to 5 °C in steps of 5 °C. We record the diffraction pattern for each temperature mainly during cooling from L_α phase, but we also observe the phase behavior during initial heating of the samples. Relative humidity was kept fixed at ± 98%. Typical exposure time was ~ 1 hour.

We have also performed diffraction experiments on unoriented samples of DPPC-cholesterol mixtures. Unoriented samples were taken in glass capillaries having a diameter of 1 mm. They were placed inside a locally built heater, whose temperature could be controlled using a standard PID controller to an accuracy of ±0.1 ^{0}C.

2.2. Preparation of giant unilamellar vesicles (GUVs) and fluorescence microscopy

GUVs were prepared using electroformation first described by Angelova et al [33]. Electroformation of vesicles produces mainly unilamellar vesicles of 10-100 μm diameter. The sample chamber consists of two platinum electrodes across which an electric field (1.5 V, 10 Hz) is applied. Stock solutions of the mixture of phospholipid, cholesterol and a fluorescence dye were prepared in chloroform (0.5 mg/ml). 1-2 μl of the stock solution was taken out using a hamilton syringe and coated onto two platinum electrodes and the solvent was then allowed to evaporate. After removing all traces of the solvent, about 500 μl of Millipore water was added to the chamber and a 10-15 Hz alternating electric field of 1-3 volts amplitude was applied between the platinum electrodes. The temperature was maintained above the main transition of the lipid used. This procedure results in the formation of giant unilamellar vesicles of diameter 10-100 μm. The electric field was turned off after about 1.5 hours and 100 μl of vesicular solution was transferred to a dish for microscopy observations.

GUVs were prepared with DPPC-cholesterol mixtures containing 0.2 mol% of rhodamine dihexadecyl phosphatidylcholine (Rho PE). A Heâ€“Ne laser of wavelength 543 nm (1 mW) was used to excite the Rho PE. Fluorescence images of the GUVs were taken using a Zeiss confocal laser scanning microscope (ZEISS LSM 510).

3. Results

3.1. Small angle x-ray scattering

Phase behavior of DPPC-cholesterol system has been investigated at various cholesterol concentrations ranging from 0 to 55 mol% in both oriented and unoriented samples. DPPC exhibits three lamellar phases at high hydration, consisting of stacks of bilayers separated by water; the fluid (L_α) phase above the main transition (42 ^{o}C), the gel ($L_{\beta'}$) phase below the pre-transition (34 ^{o}C) and the ripple phase (P_β) in between [34]. Two distinct wide angle reflections: One on-axis (q_z = 0) and the other off-axis ($q_z \neq 0$) in the diffraction pattern in the gel phase (Figure 1) clearly indicate that molecules are tilted with respect to the layer normal. Tilt angle, measured from the position of the wide angle reflection, is 30 °.

Incorporation of 2.5 to 10 mol% of cholesterol does not affect the main and pretransition temperatures considerably. Below pretransition, we observe two sets of reflections in the small angle region of diffraction pattern (Figure 2), indicating coexistence of $L_{\beta'}$ with the new modulated phase (P_β). Phase diagram of DPPC-cholesterol mixtures at 98% relative humidity, constructed from the diffraction data, was described in ref. [35, 36]. For X_c >22, P_β phase disappears and the cholesterol rich liquid ordered (l_o) phase persists throughout the temperature range studied.

It would also be interesting to know the stability of the P_β phase in excess water. therefore, unoriented samples of DPPC-cholesterol mixtures have been studied in order to investigate phase behaviour of this system in excess water. Lamellar d-spacings obtained from diffraction data of unoriented samples at 25 °C and 50 °C have been summarized

Table 1. Lamellar spacings d (Å) obtained from unoriented samples of DPPC-cholesterol mixtures with excess water.

T (˚C)	X_c (mol%)				
	0	5	10	33	50
25	63.4	74.5	85.7	68.9	65.8
50	65.0	65.4	67.8	67.1	65.2

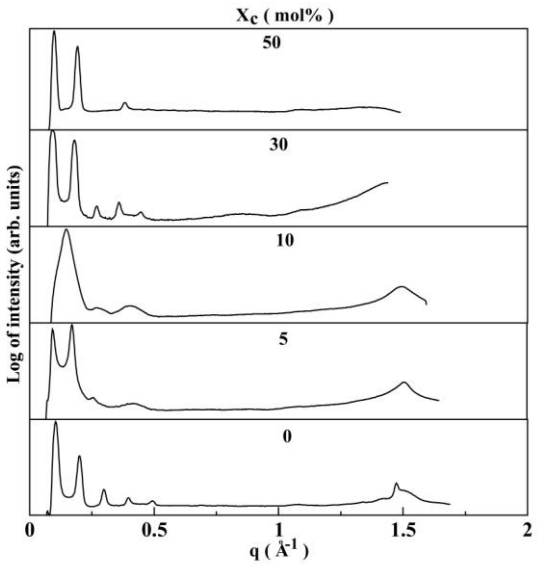

Figure 3. Plot of intensity vs q obtained from unoriented samples of DPPC-cholesterol mixtures with excess water at 25 ˚C.

in Table 1. At X_c = 5 and 10, the typical range of X_c in which the P_β phase occurs, the d-spacing increases drastically to 74.5 Å and 85.7 Å on cooling, respectively. At X_c = 33 and 50 mol%, there is not much change in the d-spacing with increasing temperature, indicating a single cholesterol rich fluid phase (l_o). Plots of log of intensity vs q for different X_c are shown in Figure 3. As seen in Figure 3, the position of the wide angle reflection is shifted towards lower q value at higher X_c which is also found in case of aligned samples. In these mixtures, we have not observed any macroscopic phase separation.

3.2. Fluorescence microscopy

Confocal fluorescence microscopy studies were carried out on GUVs made up of a few DPPC-cholesterol mixtures with cholesterol concentration (X_c) ranging from 0 to 40 mol%. All observations were performed at room temperature (23 ˚C). At room temperature, DPPC bilayers are in the gel phase. Incorporation of small amount of cholesterol ($1.5 < X_c < 10$), GUVs show significant thermal shape fluctuations, indicating softening of the bilayer (Figure 4a). Depending upon the size of the GUVs, we have observed different behaviors.

Smaller GUVs (diameter D $< \sim 20$ μm) are almost spherical in shape and exhibit phase separation. They show dark irregular domains on a bright background indicating the coexistence of two phases (Figure 4b and Figure 5). This phase separation was observed using fluorescence dye, Rho PE. Partitioning of the dye into the two phases suggests that these dark domains are in the gel phase, since Rho PE is known to prefer the fluid phase [9]. This is also supported by the fact

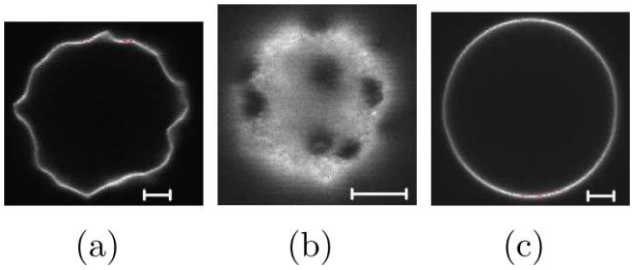

Figure 4. Micrographs of of GUVs made from DPPC–cholesterol mixtures at X_c = 1.5 mol% showing the shape fluctuation (a) and coexistence of gel domains with the fluid phase (Figure b,c) shows spherical GUV at X_c = 20 mol%. Scale bars, 5 μm.

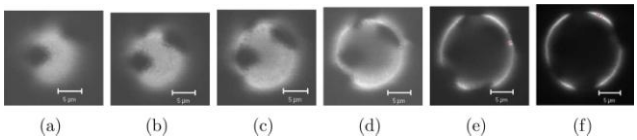

Figure 5. Different confocal sections from top to bottom of a GUV made from DPPC-cholesterol mixture (X_c = 5 mol%) showing coexistence of gel domains with cholesterol-rich fluid phase. Background of the top section of GUV is brighter due to change in contrast in order to make the black domains visible, scale bars, 5 μm

that the domains have irregular shape and do not coalesce on colliding. As the size of these dark domains are very small compared to the size of GUVs, they are clearly visible only at the top or bottom surface of GUVs (Figure 4b). However, we did observe significant intensity variation at the equatorial section of some GUVs due to phase separation (Figure 5). Since GUVs are not attached to the substrate, the position of the GUVs was found to shift after a few scans. As a result, we were not able to obtain good three dimensional images of GUVs. It is interesting to note that the number of GUVs showing the coexistence of the gel and fluid phases decreases as X_c is increased from 1.5 to 10 mol%.

For larger GUVs of D $> \sim 20$ μm, the coexistence of gel and cholesterol-rich phase was not observed at $X_c < 10$ mol%. However, we cannot rule out the possibility of phase separation, as there could be tiny gel domains which are beyond the resolution of the microscope. At these X_c, almost all GUVs show arbitrary non-spherical shapes. These non-spherical GUVs exhibit pronounced thermal shape fluctuations. Interestingly surface of these non-spherical GUVs show corrugations and some of them also show sharp edges on their surface as shown in Figure 4a. As X_c is increased from 5 to 10, the number of non-spherical GUVs decreases.

For $X_c > 10$, GUVs of all sizes are almost spherical as shown in Figure 4c. However, these GUVs do not exhibit significant thermal shape fluctuations indicating increase in the membrane bending rigidity with increasing X_c. GUV surface becomes smooth compared to the corrugated surface observed at lower X_c. This observation is in agreement with the results of recent molecular dynamics simulations of phospholipid-cholesterol membranes [27].

4. Discussion

Thermotropic phase behavior and structure of phospholipid-cholesterol membranes have been probed using

x-ray diffraction and laser scanning fluorescence microscopy techniques. Diffraction techniques are insensitive to determine microscopic phase separation in the plane of bilayers. However, macroscopic phase separation in the plane of bilayer can easily be detected from non-overlapping reflections coming from individual phases. On the basis of the diffraction data we have determined the phases and phase boundaries. Information about in-plane order of bilayers can be envisaged from the wide angle reflections. For example, two distinct wide angle reflection in the gel phase of DPPC (Figure 1) is an signature of quasi hexagonal lattice formed by tilted all-trans hydrocarbon chains of lipid molecules. However, wide angle reflection in the L_α phase is too weak to be detected, indicating fluid, flexible bilayers in this phase.

Although the phase behaviour of the DPPC-cholesterol mixtures has been presented before, the present study provides a comparison of results obtained from diffraction study with that of microscopy observation. The P_β phase is a cholesterol induced modulated phase and is distinct from the usual ripple ($P_{\beta'}$) phase [36]. As can be seen from our unoriented diffraction data (Figure 1) of DPPC-cholesterol mixtures, the lamellar phase at $5 \leq X_c \leq 10$ can swell giving rise to a large d-spacing of $\sim$ 85 Å. This is the range of X_c in which the P_β phase occurs. We have not observed the coexistence of the P_β with the gel phase in these unoriented samples. Unoriented samples could lead to the overlapping of satellite reflections with the lamellar reflections in the diffraction pattern, and make the identification of modulated phase difficult. The relatively large lamellar periodicity of the cholesterol-rich phase clearly indicates that the bilayers are flexible. This is again supported by the fact that few lamellar reflections were observed and higher order lamellar reflections are broad. The occurrence of the modulated phase in oriented samples might be a consequence of enhanced bilayer flexibility due to the presence of cholesterol. It is possible that on swelling the height modulation of the bilayers are no more correlated. Therefore, The P_β phase might not exist with excess water which is consistent with the results on unoriented samples. It was suggested that this increase in d might be the consequence of a decrease in the attractive van der Waals interaction between the bilayers in the presence of cholesterol [37]. However, the fact the cholesterol-rich l_o phase, occurring at much higher X_c ($>$ 25 mol%), has a smaller d does not support this conjecture. Therefore, it is likely that this increase in d arises from an increase in the steric repulsion between the bilayers, resulting from thermal undulations of the bilayers [38]. Indeed our confocal fluorescence microscopy study on GUVs made from DPPC-cholesterol mixtures shows significant thermal shape fluctuations at small values X_c. This observation reveals an unexpected softening of bilayers. At higher cholesterol content ($X_c >$ 25 mol%), d spacing becomes comparable with that of fluid (L_α) phase and no swelling behavior was observed in the diffraction study.

As mentioned above, the microscopy observations on GUVs made from DPPC-cholesterol mixtures are consistent with the large d-spacing of the bilayers in diffraction study. Smaller GUVs of D $<$ 20 μm show dark irregular gel domains, indicating phase separation between gel and fluid phases. Such phase separation has not been observed in earlier optical microscopy study on this system. The fact that larger GUVs do not show domains might be the consequence of differences in the kinetics of the nucleation process involved in the formation of domains. However, we cannot rule out the possibility of phase separation, as there could be tiny gel domains which are beyond the resolution of the microscope. Size dependent behaviour of GUVs could also be due to differences in the tension of the membranes in these GUVs, as smaller vesicles seem to be more tense than larger ones. Occurrence of sharp edges in non-spherical large GUVs in the absence of any phase separation is intriguing, since the formation of such structures is normally associated with the presence of domains with sufficiently different membranes properties. The significant thermal shape fluctuations of these GUVs at $X_c < 5$, at lower T, indicating the softening of bilayer, are also surprising, as cholesterol is known to increase the bending rigidity of fluid membranes. It is important to note that softening of bilayers reported in neutron scattering experiments near the main transition of DMPC–cholesterol mixtures is different from that seen in the present study [39]. It is possible that the softening of the bilayer at lower X_c is a result of the coupling between curvature and cholesterol concentration in the bilayer. Such coupling can in principle reduce the binding rigidity of the membranes.

It is clearly evident from our results that thermal fluctuations observed in DMPC-cholesterol mixtures (data are not shown) near and above the main transition is different from the shape fluctuations in DPPC-cholesterol mixtures at low temperatures. We believe that the shape fluctuations at low temperatures in DPPC-cholestrol mixtures are the consequence of the occurrence of modulated phase seen in diffraction study of oriented multilayers of this system.

5. Conclusions

We have systematically studied DPPC-cholesterol mixtures using both small angle x-ray scattering and confocal fluorescence microscopy in order to understand the influence of cholesterol on phospholipid membranes. The cholesterol induced modulated (P_β) phase in phospholipid membranes observed in the intermediate cholesterol concentration range (2-20 mol%) has not been seen in unoriented bilayers in excess water. However, swelling of bilayers, resulting in large d-spacing has been observed at similar cholesterol concentration at which the P_β phase occurs. Confocal fluorescence microscopy studies on giant unilamellar vesicles have shown significant thermal shape fluctuations, indicating softening of bilayers at small cholesterol concentrations. Coexistence between gel and fluid phases in binary phospholipid-cholesterol mixtures, observed in the present study, has not been seen in any of the earlier microscopy studies. These observations are consistent with and compliment the results of x-ray diffraction study.

Acknowledgments

We thank Prof. Satyajit Mayor for allowing access to the fluorescence microscopy facility and for many useful discussions.

References

1. B. Alberts, D. Bray, J. Lewis, M. Raff, K. Roberts and J. D. Watson, Molecular Biology of the Cell, Garland publishing, Tayor and Francis Group (1994).
2. M. Raguz, L. Mainali, J. Widomska, W. K. Subcyznski, Biochim. Biophys. Acta 1808 (2011) 1072.

3. K. Simans and W. L. C. Vaz, Annu. Rev. Biophys. Biomol. Struct. 33 (2004) 269.
4. Silvius, J. R., Biochim. Biophys. Acta 1610 (2003) 174.
5. P. J. Quinn, Prog. lipid Res. 49 (2010) 390.
6. W. F. Bennett, D, P. Tieleman, J. Lipid Res. 53 (2012) 421.
7. H. HeerKlotz, Biophys. J. 83 (2002) 2693.
8. de Almeida, R. F. M., A. Fedorov and M. Prieto, Biophys. J. 85 (2003) 2406.
9. Baumgart, T., S. T. Hess, and W. W. Webb, Nature 425 (2003) 821.
10. Brown, D. A., and E. London, J. Biol. Chem. 275 (2000) 17221.
11. S. L. Veatch and S. L. Keller, Biophys. J. 85 (2003) 3074.
12. C. Dietrich, L. A. Bagatolli, Z. N. Volovyk, N. L. Thompson, M. Levi, K. Jacobson, and E. Gratton, Biophys. J. 80 (2001) 1417.
13. D. Robinson, N. A. Besley, P. O'Shea and J. D. Hirst, J. Phys. Chem. B 115 (2011) 4160.
14. W. Knoll, G. Schmidt, K. Ibel, and E. Sackmann, Biochemistry 24 (1985) 5240.
15. M. R. Vist and J. H. Davis, Biochemistry 29 (1990) 451.
16. M. B. Sankaram and T. E. Thompson, Biochemistry 29 (1990) 10670.
17. M. B. Sankaram and T. E. Thompson, Proc. Natl. Acad. Sci. U. S. A. 88 (1991) 8686.
18. B. R. Lentz, D. A. Barrow, and M. Hoechli, Biochemistry 19 (1980) 1943.
19. C. Paré and M. Lafleur, Biophys. J. 74 (1998) 899.
20. T. P. W. Mcmullen, R. N. A. H. Lewis, and R. N. McElhaney, Biochim. Biophys. Acta 1416 (1999) 119.
21. W. F. Bennett, J. L. Maccallum and D. P. Tieleman, J. Am. Chem. Soc 131 (2009) 1972.
22. Hui, S. W., N. B. He, Biochemistry 22 (1983) 1159.
23. J. H. Ipsen, G. Karlström, O. G. Mouritsen, H. Wennerström, and M. J. Zuckermann, Biochim. Biophys. Acta 905 (1987) 162.
24. Filippov, J, G. Orädd, G. Lindblom., Biophys. J. 84 (2003) 3097.
25. T. J. McIntosh, Biochim. Biophys. Acta 513 (1978) 43.
26. K. Mortensen, W. Pfeiffer, E. Sackmann, and W. Knoll, Biochim. Biophys. Acta 945 (1988) 221.
27. C. L. Wennberg, D. Van der . Spoel, J. S. Hub, J. Am. Chem. Soc. 134 (2012) 5351.
28. H. Saito, W. Shinoda, J. Phys. Chem. B 115 (2011) 15241.
29. L. A. Bagatolli and E. Gratton, Biophys. J. 77 (1999) 209.
30. J. Käs and E. Sackmann, Biophys. J. 60 (1991) 82.
31. R. Lipowsky and E. Sackmann, Handbook of Biological Physics, Elesevier, Amsterdam, Vol. 1 (1995).
32. U. Seifer, Phys. Rev. Lett. 70 (1993) 1335.
33. M. I. Angelova, S. Solé, Ph. Méléard, J. E. Faucon, and P. Bothorel, Prog. Colloid Polym. Sci. 89 (1992) 127.
34. M. J. Janiak, D. M. Small, and G. G. Shipley, Biochemistry 15 (1976) 4575.
35. S. Karmakar and V. A. Raghunathan, Phys. Rev. Lett. 91 (2003) 98102.
36. S. Karmakar and V. A. Raghunathan, Phys. Rev. E. 71 (2005) 61924.
37. R. P. Rand, V. A. Parsegian, J. A. C. Henry, L. J. Lis, and M. McAlister, Can. J. Biochem. 58 (1980) 959.
38. W. Helfrich, Z. Naturforsch. C. 28 (1973) 693.
39. J. Lemmich, K. Mortensen, J. H. Ipsen, T. Hø nger, R. Bauer, and O. G. Mouritsen, Eur. Biophys. J. 25 (1997) 293.

Cite this article as:

Sanat Karmakar *et al.*: **X-ray diffraction and confocal fluorescence microscopy studies on the effect of cholesterol on phospholipid membranes.** *Phys. Express* 2014, **4:** 6

Variations in structural and magnetic phase transitions of Ni-Mn-In-Si alloy with change in Ni/Mn ratio

Rahul Das*, S. Sarma, B. Deka, A. Perumal, A. Srinivasan

Department of Physics, Indian Institute of Technology Guwahati, Guwahati – 781039, India

Author for correspondence: Rahul Das, email: d.rahul@iitg.ernet.in
Received 27 Mar 2013; Accepted 27 Apr 2013; Available Online 27 Apr 2013

Abstract

Effect of varying Ni/Mn ratio on the structural (martensitic) and magnetic phase transitions of parent as well as Si substituted Ni-Mn-In alloys has been investigated using X-ray diffraction and magnetometry techniques. A small increase in Ni/Mn ratio by a mere 1 at.% drives all the structural characteristic temperatures toward higher value but the magnetic Curie temperatures decrease due to this change. At low temperatures, the exchange bias which occurs due to the coexistence of antiferromagnetic and ferromagnetic phases, decreases as the Ni/Mn ratio is increased. A remarkable magnetic entropy change (ΔS_M) is exhibited by these alloys at the first-order structural phase transition. Ni substitution for Mn enhanced ΔS_M and the highest ΔS_M (= 19.9 $Jkg^{-1}K^{-1}$) was exhibited by $Ni_{51}Mn_{34}In_{14}Si_1$ alloy at 279 K for a magnetic field change of 0 – 1.2 T.

Keywords: Martensitic phase transition; Magnetic phase transition; Magnetic entropy change; Exchange bias; Ferromagnetic shape memory alloys

1. Introduction

Since the recent discovery of structural transition in Ga-free Ni–Mn based alloys [1], much attention has been devoted to investigate their multifunctional applications [2-6]. These alloys exhibit diverse physical properties such as ferromagnetic shape memory effect, magnetocaloric effect (MCE), magnetic superelasticity, magnetoresistance and exchange bias (EB) due to the first-order diffusionless structural phase transition occurring between the high crystallographic symmetry austenite (A) phase and a low symmetry martensite (M) phase [5-9]. Ni-Mn-In is a promising ferromagnetic shape memory alloy (FSMA) which possesses several key features of the prototype FSMA, Ni–Mn–Ga alloys. The lower cost and high or ambient characteristic temperatures of Ni-Mi-In alloy makes it more favorable for applications at ambient temperature. Generally, Ni-Mn-X (where X = In, Sn, Sb) alloys exhibit at least two phase transitions, viz., a second-order magnetic phase transition at the Curie temperature (T_C) and a first-order structural phase transition at the martensitic start temperature (T_{Ms}) [1, 8]. Independently or simultaneously, these two phase transitions are responsible for almost all the physical properties of this alloy. Interestingly, T_{Ms} and T_C of Ni-Mn-In alloys can be tuned by varying the electronic concentration (*e/a* ratio). The *e/a* ratio, which depends on the concentration weighted sum of valence electrons of the constituent atoms, can be varied by changing the composition of the alloys. Inherent sensitivity of the physical properties of $Ni_{50}Mn_{50-x}In_x$ alloys to composition variations has been demonstrated [1,2]. No structural (M ↔ A) transformation in $Ni_{50}Mn_{50-x}In_x$ was observed above a critical In concentration of 16 at.% corresponding to *e/a* ratio of 7.86. For alloys with $16 \geq x \geq 5$, T_{Ms} was found to increase with decrease in In concentration [2]. The Mn–Mn bond length determines the exchange interaction as well as the degree of magnetic ordering in Mn based Heusler alloys [10-12]. The magnetic moment coupling between adjacent Mn atoms may change from ferromagnetic (FM) to antiferromagnetic (AFM) depending upon the Wyckoff positions of the Mn atoms. Due to this AFM coupling, the martensitic phase exhibits a smaller magnetization than the austenite phase. So, considerable change in magnetization is associated with the structural transition which in turn changes the magnetic properties of the FSMA at the structural transition [2,6]. This magnetostructural coupling in $Ni_{50}Mn_{50-x}In_x$ alloys is responsible for a plethora of exciting phenomena observed such as magnetic field induced strain, magnetic superelasticity, large MCE, giant magnetothermal conductivity, giant Hall effect, and exchange bias [6, 9, 13-15]. Rao *et al.* [16,17] have investigated the effect of excess Mn substitution for Ni on the structure, phase transition temperatures and magnetic properties of $Ni_{50-x}Mn_{37+x}In_{13}$ alloys. They have also reported a large MCE with high magnetic entropy change (ΔS_M) of 23.5 $Jkg^{-1}K^{-1}$at 308 K for a low field change of 2 T. It is well known that the transition temperatures as well as the magnetic parameters can be tuned markedly by partial substitution of magnetic or nonmagnetic elements in Ni–Mn–In alloys [18-20]. These additional atoms can perturb the coupling between Mn-Mn atoms, as well as the *e/a* ratio [19-21]. Recently, the effect of partial substitution of Si and Ge for In on the structure and magnetocaloric properties of $Ni_{50}Mn_{35}In_{15}$ alloy has been reported [19, 21]. Due to the large change in magnetic moment at the phase transitions occurring near ambient temperature, Ni-Mn-In-X alloy has a great potential for practical applications. In this paper, we present the effect of Ni/Mn ratio variation on the structural and magnetic properties of $Ni_{50}Mn_{35}In_{15}$ and $Ni_{50}Mn_{35}In_{14}Si_1$ alloys.

Table 1. Nominal composition, measured composition, electron concentration (*e/a* ratio), room temperature crystal structure (orthorhombic martensite and cubic austenite represented by M and A), lattice parameters (*a*, *b* and *c*) and unit-cell volume (*V*) of $Ni_{50}Mn_{35}In_{15}$, $Ni_{51}Mn_{34}In_{15}$, $Ni_{50}Mn_{35}In_{14}Si_1$ and $Ni_{51}Mn_{34}In_{14}Si_1$ alloys.

Nominal Composition	Composition from EDS	*e/a*	Crystal phase	*a* (nm)	*b* (nm)	*c* (nm)	*V* (nm^3)
$Ni_{50}Mn_{35}In_{15}$	$Ni_{50.21}Mn_{34.95}In_{14.84}$	7.91	M	1.758	1.166	0.458	0.939
$Ni_{51}Mn_{34}In_{15}$	$Ni_{50.97}Mn_{33.45}In_{15.58}$	7.91	M	1.706	1.070	0.469	0.856
$Ni_{50}Mn_{35}In_{14}Si_1$	$Ni_{49.81}Mn_{34.99}In_{13.84}Si_{1.36}$	7.90	A	0.598	0.598	0.598	0.214
$Ni_{51}Mn_{34}In_{14}Si_1$	$Ni_{50.69}Mn_{33.83}In_{14.07}Si_{1.41}$	7.92	A	0.597	0.597	0.597	0.213

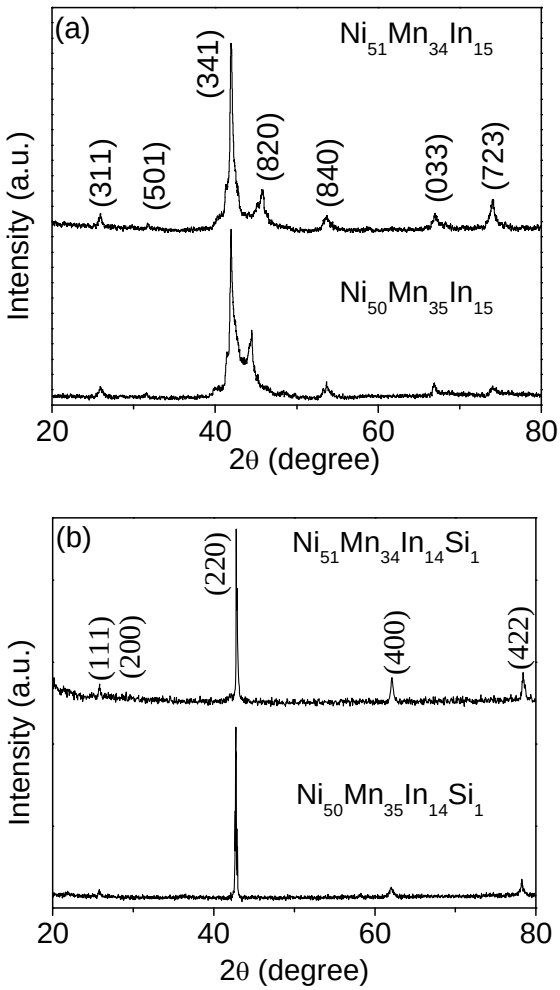

Figure 1. Room temperature XRD patterns of (a) $Ni_{50}Mn_{35}In_{15}$ and $Ni_{51}Mn_{34}In_{15}$, and (b) $Ni_{50}Mn_{35}In_{14}Si_1$ and $Ni_{51}Mn_{34}In_{14}Si_1$ alloys.

2. Experimental Details

Polycrystalline $Ni_{50}Mn_{35}In_{15}$, $Ni_{51}Mn_{34}In_{15}$, $Ni_{50}Mn_{35}In_{14}Si_1$ and $Ni_{51}Mn_{34}In_{14}Si_1$ ingots were prepared from high purity elements by arc melting in argon atmosphere. The final alloy ingot was obtained after repeated melting to ensure proper homogenization of the alloy. The net weight loss in the cast samples was found to be $\leq$ 1.5% of the initial weight. The cast samples were sealed in fused silica tubes under a pressure of 10^{-3} Pa, annealed at 1173 K for 20 h and quenched in ice water. Structural analysis of the annealed alloys was carried out using a powder X-ray diffractometer (Rigaku TTRAX 18 kW and Seifert, 3003T/T) operating with

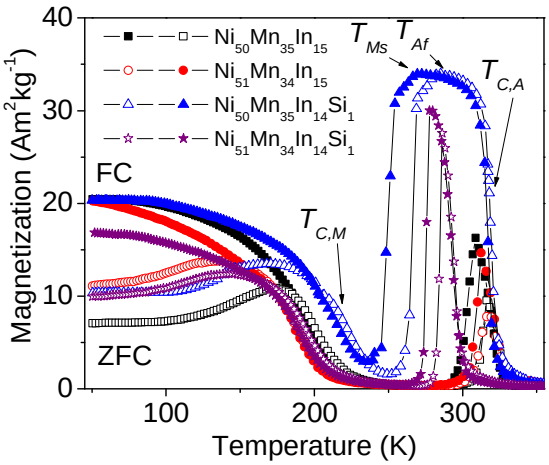

Figure 2. *M-T* curves of $Ni_{50}Mn_{35}In_{15}$, $Ni_{51}Mn_{34}In_{15}$, $Ni_{50}Mn_{35}In_{14}Si_1$ and $Ni_{51}Mn_{34}In_{14}Si_1$ alloys obtained at an applied field of 0.1 T. Filled and open symbols represent data obtained during field-cooled (FC) and zero-field-cooled (ZFC), respectively. Curie temperature of martensitic phase ($T_{C,M}$), martensite start temperature (T_{Ms}), austenite finish temperature (T_{Af}), and the Curie temperature of the austenite phase ($T_{C,A}$) are shown.

Cu-K_α radiation (λ = 0.15406 nm). Elemental composition of the alloys was determined using an energy dispersive spectrometer (EDS) attached to a scanning electron microscope (SEM, Leo 1430VP). Magnetization measurements were carried out using a vibrating sample magnetometer (VSM, Lakeshore 7410) with closed cycle refrigerator insert.

3. Results and Discussion

X-ray diffraction (XRD) patterns (shown in Figure 1) indicate that at room temperature, $Ni_{50}Mn_{35}In_{15}$ and $Ni_{51}Mn_{34}In_{15}$ alloys are in martensitic phase (with orthorhombic unit cell) and $Ni_{50}Mn_{35}In_{14}Si_1$ and $Ni_{51}Mn_{34}In_{14}Si_1$ alloys are in austenitic phase (with cubic $L2_1$ structure), respectively. The slight reduction in unit cell volume with Ni addition indicates that the Mn atoms with larger atomic radius have been substituted by Ni. The overall composition of the alloys obtained from EDS analysis is summarised in Table 1. It can be seen that the final alloy composition is very close to the nominal (starting) composition of the respective alloys.

Figure 2 depicts the thermomagnetization (*M-T*) curves of the alloys recorded under an applied field of 0.1 T in zero-field-cooled (ZFC) and field-cooled (FC) conditions. For

Table 2. Martensite start temperature (T_{Ms}), martensite finish temperature (T_{Mf}), austenite start temperature (T_{As}), austenite finish temperature (T_{Af}), thermal hysteresis (ΔT_{hys}), martensite Curie temperature ($T_{C,M}$), austenite Curie temperature ($T_{C,A}$), bifurcation temperature (T_{bifur}) obtained at 0.1 T field, peak magnetic entropy change (ΔS_M), and exchange bias (H_E) obtained for 1.2 T field change of $Ni_{50}Mn_{35}In_{15}$, $Ni_{51}Mn_{34}In_{15}$, $Ni_{50}Mn_{35}In_{14}Si_1$ and $Ni_{51}Mn_{34}In_{14}Si_1$ alloys.

Alloy	T_{Ms} (K)	T_{Mf} (K)	T_{As} (K)	T_{Af} (K)	ΔT_{hys} (K)	$T_{C,M}$ (K)	$T_{C,A}$ (K)	T_{bifur} (K)	Peak ΔS_M ($Jkg^{-1}K^{-1}$)	H_E (mT) at 50 K
$Ni_{50}Mn_{35}In_{15}$	309	295	305	316	8.5	205	321	185	4.3	9.3
$Ni_{51}Mn_{34}In_{15}$	311	302	307	318	6.0	186	320	153	8.5	7.7
$Ni_{50}Mn_{35}In_{14}Si_1$	269	239	255	282	14.5	217	317	197	17.5	8.6
$Ni_{51}Mn_{34}In_{14}Si_1$	278	270	279	287	9.0	191	294	157	19.9	5.4

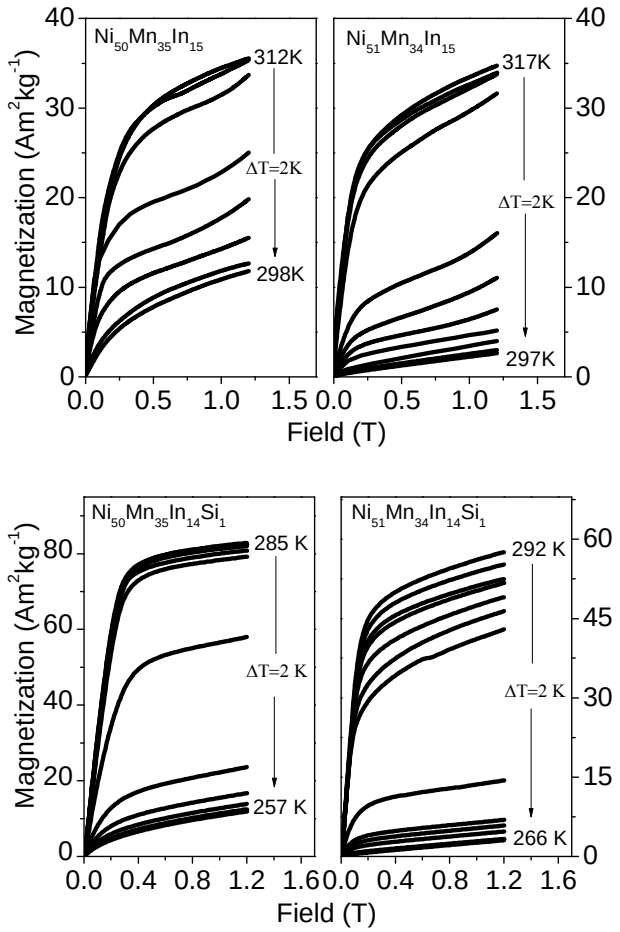

Figure 3. Isothermal magnetization curves of $Ni_{50}Mn_{35}In_{15}$, $Ni_{51}Mn_{34}In_{15}$, $Ni_{50}Mn_{35}In_{14}Si_1$ and $Ni_{51}Mn_{34}In_{14}Si_1$ alloys recorded at 2 K interval (ΔT) around martensite start temperature (T_{Ms}).

ZFC measurements, the samples were first cooled down to 50 K in the absence of magnetic field, whereas for the FC measurements, the samples were cooled down to 50 K in the presence of an external magnetic field of 0.1 T. Figure 2 shows that as the temperature is decreased from 375 K, magnetization first increases sharply due to the second order paramagnetic to ferromagnetic transition and then abruptly decreases due to the structural (A ↔ M) transformation. On further decreasing the temperature below 235 K, the samples exhibit a large increase in magnetization. This signifies the paramagnetic to ferromagnetic transition occurring in the martensite phase of the sample. Thus, all the alloys exhibit three phase transitions, viz., one structural transition at the martensite start temperature (T_{Ms}) and two magnetic transitions, one in the austenite phase (marked as $T_{C,A}$) and another in martensite phase (marked as $T_{C,M}$). Below $T_{C,M}$ and in temperature interval $T_{Ms} < T < T_{C,A}$, ferromagnetic ordering is observed in the samples. Paramagnetic behavior is observed for $T_{C,M} < T < T_{MS}$ and for $T > T_{C,A}$. At lower temperatures (below 197 K), ZFC and FC curves show a bifurcation. The bifurcation temperature (T_{bifur}) shifts to lower temperatures with increase of Ni/Mn ratio in both Ni-Mn-In and Ni-Mn-In-Si alloys as shown in Table 2. A hysteresis behavior, attributed to structural transition is also observed in the *M-T* curves when the samples are thermally cycled. This thermal hysteresis (ΔT_{hys}) can be estimated from the characteristic temperature obtained from the *M–T* curves and is given by the expression, $\Delta T_{hys} = (T_{As} + T_{Af})/2 - (T_{Ms} + T_{Mf})/2$. The lowest (highest) ΔT_{hys} of 6 K (14.5 K) is observed in $Ni_{51}Mn_{34}In_{15}$ ($Ni_{50}Mn_{35}In_{14}Si_1$) alloy. The characteristic temperature, T_{Ms} ($T_{C,M}$ and $T_{C,A}$) is defined as the temperature at which FC (d*M*/d*T* of ZFC) curve exhibits the maximum magnetization (minimum) value. T_{Ms} ($T_{C,M}$, $T_{C,A}$) of $Ni_{50}Mn_{35}In_{15}$, $Ni_{51}Mn_{34}In_{15}$, $Ni_{50}Mn_{35}In_{14}Si_1$ and $Ni_{51}Mn_{34}In_{14}Si_1$ alloys are 309 K (205 K, 321 K), 311 K (186 K, 320 K), 269 K (217 K, 317 K) and 278 K (191 K, 294 K), respectively. With the substitution of Ni for Mn in $Ni_{50}Mn_{35}In_{15}$ and $Ni_{50}Mn_{35}In_{14}Si_1$, T_{Ms} is shifted to higher temperatures, but $T_{C,M}$ and $T_{C,A}$ are shifted to lower temperatures. An earlier work [2, 22] on $Ni_{50-x}Mn_{35+x}In_{15}$ alloys showed that T_{Ms} increases with increase in *e/a* ratio. In this work, the measured compositions of $Ni_{50}Mn_{35}In_{15}$ and $Ni_{51}Mn_{34}In_{15}$ show nearly the same *e/a* ratio. T_{Ms} of these alloys differ by merely 2 K. Such small variations in T_{Ms} for alloys with same *e/a* has also been observed in some earlier work [23]. In the case of Ni-Mn-In-Si alloys, T_{Ms} increases with an increase in *e/a* ratio. Figure 2 shows another interesting feature, viz., magnitude of the magnetization change (ΔM) at the structural transition decreases with increasing Ni/Mn ratio. This behaviour closely follows the variation in unit cell volume which is in turn related to the Mn-Mn interatomic distance. Thus, the magnetic properties of Ni–Mn–X alloys are primarily determined by the Mn atoms and are described in terms of exchange interaction via conduction electrons [24]. In order to confirm the occurrence of first order structural transition at T_{Ms} in these alloys, isothermal magnetization $(M\text{-}H)_T$ curves (shown in Figure 3) were recorded close to the structural transition and Arrott (M^2 vs. *H/M*) plots were constructed from these data. Arrott plots have been used to investigate the order of martensitic transition in NiMnGa [25] and NiCoMnSb based alloys [26]. When the Arrott plots are linear across the transition, they describe a second order phase transition. In the case of martenstic transition, Arrott plots are non-linear with a S-type behavior,

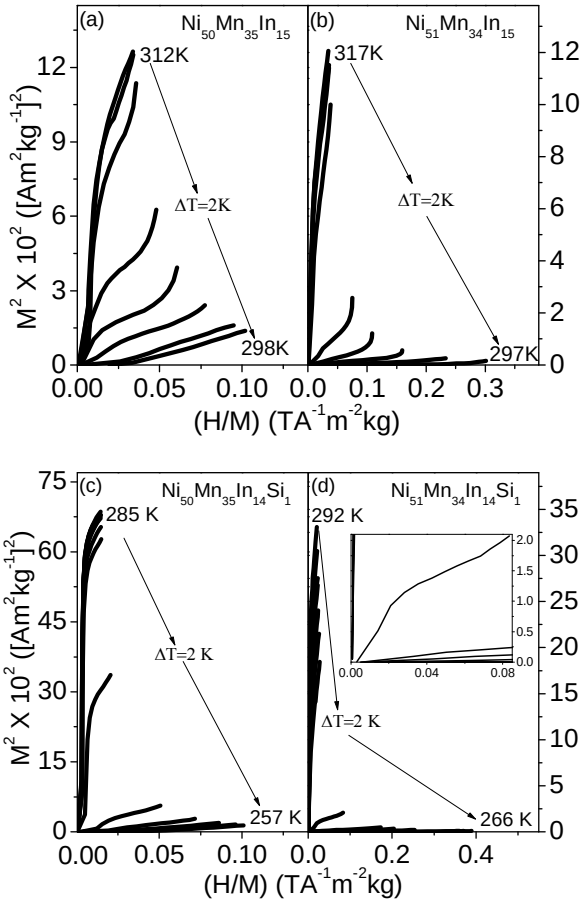

Figure 4. Arrott plots indicating the first order structural transition in (a) $Ni_{50}Mn_{35}In_{15}$, (b) $Ni_{51}Mn_{34}In_{15}$, (c) $Ni_{50}Mn_{35}In_{14}Si_1$ and (d) $Ni_{51}Mn_{34}In_{14}Si_1$ alloys. Inset in Figure 4(d) shows an enlarged view of the data near the origin.

which is ascribed to first order transition. It can be seen that the Arrott plots (Figure 4) are nonlinear (S shaped), which is indicative of the first order nature of the transition [27]. Since entropy is discontinuous at the first order phase transition, ΔS_M will be large near T_{Ms}. ΔS_M was calculated from isothermal magnetization $(M\text{-}H)_T$ data using the Maxwell relation [6, 28],

$$\Delta S_M(T,H) = \int_0^H \left(\frac{\partial M(T)}{\partial T}\right)_H dH \qquad (1)$$

ΔS_M was calculated from $(M\text{-}H)_T$ curves recorded as a function of increasing magnetic field from 0 to 1.2 T at different temperatures near T_{Ms} of the respective alloys (*cf.* Figure 3). Figure 5 depicts the variation of ΔS_M as a function of temperature for all the alloys. Peak ΔS_M value obtained for $Ni_{50}Mn_{35}In_{15}$, $Ni_{51}Mn_{34}In_{15}$, $Ni_{50}Mn_{35}In_{14}Si_1$ and $Ni_{51}Mn_{34}In_{14}Si_1$ alloys are listed in Table 2. The highest ΔS_M was exhibited by $Ni_{51}Mn_{34}In_{14}Si_1$ alloy at 279 K. ΔS_M is clearly related to the sharpness of the structural transition or the $(\partial M/\partial T)_H$ term in equation (1). A relatively sharper structural transition is observed in the Ni substituted alloys. For an applied magnetic field of 0.1 T, $Ni_{51}Mn_{34}In_{14}Si_1$ alloy exhibits the highest $(\partial M/\partial T)_H$ value of 6.6 $Am^2kg^{-1}K^{-1}$, among all the alloy compositions.

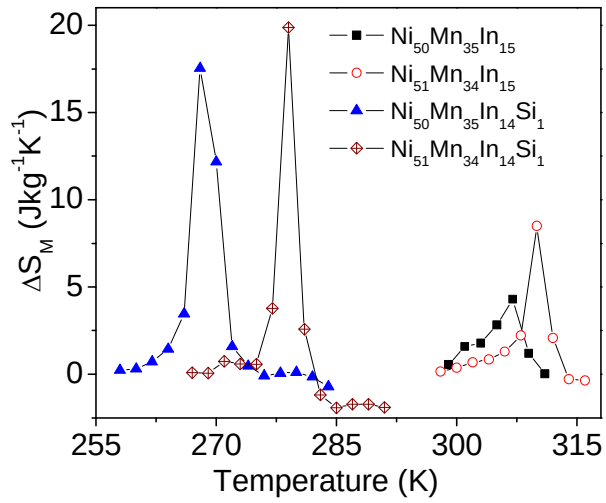

Figure 5. Temperature dependence of magnetic entropy change (ΔS_M) obtained under 1.2 Tesla field in $Ni_{50}Mn_{35}In_{15}$, $Ni_{51}Mn_{34}In_{15}$, $Ni_{50}Mn_{35}In_{14}Si_1$ and $Ni_{51}Mn_{34}In_{14}Si_1$ alloys.

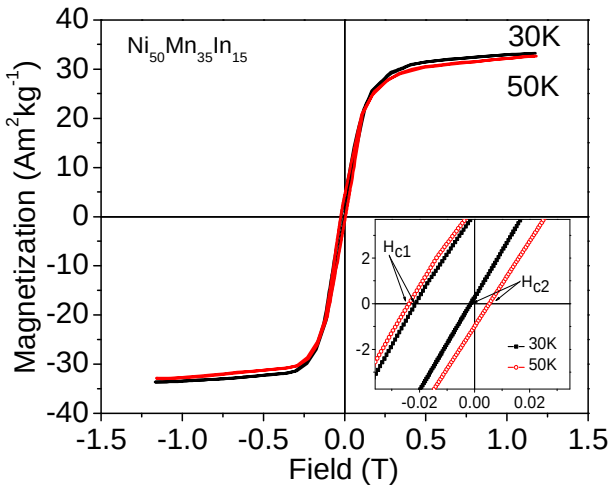

Figure 6. Typical *M-H* loops at 30 K and 50 K obtained under 1.2 T field for $Ni_{50}Mn_{35}In_{15}$ alloy. Inset shows an expanded view of the data near the origin.

The bifurcation observed below T_{bifur} in the *M-T* curves shown in Figure 2 can be attributed to the co-existence of FM and AFM phases. When such a system is cooled below T_{bifur} under a magnetic field, one can expect a shift in the *M-H* loop towards the negative field axis. Such a shift in the *M-H* loop is a manifestation of exchange bias H_E [29], which can be estimated from the relation [30],

$$H_E = -\left(\frac{H_{c1} + H_{c2}}{2}\right) \qquad (2)$$

where, H_{c1} and H_{c2} are the negative and positive coercive fields at which the magnetization is zero. Figure 6 shows the *M-H* loops for $Ni_{50}Mn_{35}In_{15}$ alloy recorded at two temperatures well below T_{bifur}. It is evident from the Figure that the loop shifts more towards the negative field axis as the temperature is decreased. H_E at 50 K and 30 K are 9.3 and 11 mT, respectively. Similar behaviour is also shown by Si substituted Ni-Mn-In alloy as shown by the corresponding H_E data listed

in Table 2. With increase in Ni/Mn ratio, H_E decreases. Observation of exchange bias verifies the coexistence of FM and AFM interactions in these alloys. Existence of AFM coupling in Ni-Mn-X alloys has been proposed by many researchers [8, 12, 30-32]. However, experimentally the same has been established in $Ni_2Mn_{1.44}Sn_{0.56}$ alloys by neutron diffraction studies [12]. In FSMAs, Mn occupying Mn sites results in FM interaction. On the other hand, Mn occupying Ni or In anti-sites induces AFM interactions. When Ni/Mn ratio is decreased in Ni-Mn-In (and Ni-Mn-In-Si) alloys, the excess Mn atoms occupying Ni (or In) anti-sites can result in AFM coupling [33]. This leads to an increase in H_E in Ni-Mn-In and Ni-Mn-In-Si alloys as indicated in Table 2. These H_E values may be compared with those reported for $Ni_{50}Mn_{35}In_{15}$ (~9.6 mT) [31], $Ni_{49.5}Mn_{34.5}In_{16}$ (~8.4 mT) [30] and $Ni_{50}Mn_{35}In_{14}Si_1$ (~6.7 mT) [34] alloys at 50 K. The possibility of varying H_E by changing Ni/Mn ratio in bulk Ni-Mn-In alloys is reported for the first time in this work. Exchange bias properties are generally observed in inhomogeneous materials or thin films [35, 36].

4. Conclusions

Variations in magnetic and magneto-caloric properties with small change of Ni/Mn ratio in $Ni_{50}Mn_{35}In_{15}$ and $Ni_{50}Mn_{35}In_{14}Si_1$ alloys have been studied. ΔS_M is positive in all the investigated alloys because $\partial M/\partial T$ is positive at the first order structural phase transition. Positive ΔS_M (or inverse MCE) implies that the sample cools down upon application of external magnetic field. Maximum ΔS_M of 19.9 $Jkg^{-1}K^{-1}$ was obtained for $Ni_{51}Mn_{34}In_{14}Si_1$ alloy at 279 K, just below the ambient temperature for a magnetic field change of 0 to 1.2 T in this study. Exchange bias phenomenon has been observed in all of the alloys studied. Influence of Ni/Mn ratio on H_E has been reported for the first time in these alloys. These results are expected to aid technological exploitation of these alloys in futuristic magnetic devices such as read heads for ultra-high density magnetic recording and spintronics devices.

Acknowledgments

Financial assistance from Council of Scientific and Industrial Research [Project No: 03(1236)/12/EMR-II] and infrastructural facilities provided by the DST [SR/S2/CMP-19/2006 and SR/FST/PII-020/2009] are gratefully acknowledged.

References

1. Y. Sutou, Y. Imano, N. Koeda, T. Omori, R. Kainuma, K. Ishida and K. Oikawa, Appl. Phys. Lett. 85 (2004) 4358.
2. T. Krenke, M. Acet, E. F. Wassermann, X. Moya, L. Mañosa, and A. Planes, Phys. Rev. B. 73 (2006) 174413.
3. V. K. Sharma, M. K. Chattopadhyay, and S. B. Roy, Phys. Rev. B. 76 (2007) 140401.
4. X. Moya, D. González-Alonso, L. Mañosa, A. Planes, V. O. Garlea, T. A. Lograsso, D. L. Schlagel, J. L. Zarestky, S. Aksoy, and M. Acet, Phys. Rev. B. 79 (2009) 214118.
5. M. Khan, I. Dubenko, S. Stadler, and N. Ali, Appl. Phys. Lett. 91 (2007) 072510.
6. T. Krenke, E. Duman, M. Acet, E. F. Wassermann, X. Moya, L. Mañosa, A. Planes, E. Suard, and B. Ouladdiaf, Phys. Rev. B. 75 (2007) 104414.
7. M. Khan, N. Ali, and S. Stadler, J. Appl. Phys. 101 (2007) 053919.
8. A. K. Pathak, M. Khan, B. R. Gautam, S. Stadler, I. Dubenko, and N. Ali, J. Magn. Magn. Mater. 321 (2009) 963.
9. B. Zhang, X. X. Zhang, S. Y. Yu, J. L. Chen, Z. X. Cao, and G. H. Wu, Appl. Phys. Lett. 91 (2007) 012510.
10. C. V. Stager, and C. C. M. Campbell, Can. J. Phys. 56 (1978) 674.
11. J. Kubler, A. R. Williams, and C. B. Sommers, Phys. Rev. B. 28 (1983) 1745.
12. P. J. Brown, A. P. Gandy, K. Ishida, R. Kainuma, T. Kanomata, K. U. Neumann, K. Oikawa, B. Ouladdiaf and K. R. A. Ziebeck, J. Phys.: Condens. Matter 18 (2006) 2249.
13. B. M. Wang, Y. Liu, P. Ren, B. Xia, K. B. Ruan, J. B. Yi, J. Ding, X. G. Li, and L. Wang, Phys. Rev. Lett. 106 (2011) 077203.
14. I. Dubenko, A. K. Pathak, S. Stadler, N. Ali, Y. Kovarskii, V. N. Prudnikov, N. S. Perov, and A. B. Granovsky, Phys. Rev. B. 80 (2009) 092408.
15. R. Y. Umetsu, Y. Kusakari, T. Kanomata, K. Suga, Y. Sawai, K. Kindo, K. Oikawa, R. Kainuma, and K. Ishida, J. Phys. D: Appl. Phys. 42 (2009) 075003.
16. N. V. Rama Rao, V. Chandrasekaran, and K. G. Suresh, J. Appl. Phys. 108 (2010) 043913.
17. N. V. Rama Rao, R. Gopalan, V. Chandrasekaran, and K. G. Suresh, Appl. Phys. A 99 (2010) 265.
18. R. Kainuma, Y. Imano, W. Ito, Y. Sutou, H. Morito, S. Okamoto, O. Kitakami, K. Oikawa, A. Fujita, T. Kanomata, and K. Ishida, Nature 439 (2006) 957.
19. A. K. Pathak, I. Dubenko, S. Stadler and N. Ali, J. Phys. D. Appl. Phys. 41 (2008) 202004.
20. V. K. Sharma, M. K. Chattopadhyay, A. Khandelwal, and S. B. Roy, Phys. Rev. B. 82 (2010) 172411.
21. A. K. Pathak, I. Dubenko, J. C Mabon, S. Stadler, and N. Ali, J. Phys. D: Appl. Phys. 42 (2009) 045004.
22. B. Gao, F. X. Hu, J. Shen, J. Wang, J. R. Sun, and B. G. Shen, J. Appl. Phys. 105 (2009) 083902.
23. W. Ito, Y. Imano, R. Kainuma, Y. Sutou, K. Oikawa, and K. Ishida, Metall. Mater. Trans. A 38 (2007) 759.
24. P. J. Brown, A. Y. Bargawi, J. Crangle, K. U. Neumann and K. R. A. Ziebeck, J. Phys.: Condens. Matter 11 (1999) 4715.
25. X. Zhou, W. Li, H. P. Kunkel, and G. Williams, Phys. Rev. B. 73 (2006) 012412.
26. R. Sahoo, A. K. Nayak, K. G. Suresh, and A. K. Nigam, J. Appl. Phys. 109 (2011) 07A921.
27. N. H. Duc, D. T. Kim Anh and P. E. Brommer, Physica B 319 (2002) 1.
28. A. M. Tishin and I. Spichkin, The Magnetocaloric Effect and Its Applications, Institute of Physics, Bristol (2003).
29. G. Vallejo-Fernandez, L. E. Fernandez-Outon, and K. O'Grady, J. Appl. Phys. 103 (2008) 07C101.
30. B. M. Wang, Y. Liu, L. Wang, S. L. Huang, Y. Zhao, Y. Yang, and H. Zhang, J. Appl. Phys. 104 (2008) 043916.
31. C. Jing, J. Chen, Z. Li, Y. Qiao, B. Kang, S. Cao, J. Zhang, J. Alloys Compd. 475 (2009) 1.
32. S. Esakki Muthu, N. V. Rama Rao, D. V. Sridhara Rao, M. Manivel Raja, U. Devarajan, and S. Arumugam, J. Appl. Phys. 110 (2011) 023904.
33. X. G. Zhao, C. C. Hsieh, J. H. Lai, X. J. Cheng, W. C. Chang, W. B. Cui, W. Liu and Z. D. Zhang, Scripta Mater. 63 (2010) 250.
34. A. K. Pathak, I. Dubenko, S. Stadler and N. Ali, IEEE Trans. Magn. 45 (2009) 3855.
35. J. Nogues and I. K. Schuller, J. Magn. Magn. Mater. 192 (1999) 203.
36. J. C. S. Kools, IEEE Trans. Magn. 32 (1996) 3165.

Cite this article as:

Rahul Das *et al.*: **Variations in structural and magnetic phase transitions of Ni-Mn-In-Si alloy with change in Ni/Mn ratio.** *Phys. Express* 2014, **4:** 7

Ab–initio study of structural, electronic and vibrational properties of Si_xGe_y (x + y ≤ 4) nanoclusters

R. K. Yadav[a,*], Sohini Goswami[a], P. S. Yadav[b]

[a] *Department of Physics, National Institute of Technology Agartala, Tripura, India-799055*
[b] *Department of Physics, University of Allahabad, Allahabad, India-211002*

[*] *Author for Correspondence: R. K. Yadav, email: rkyadav.phy@nita.ac.in*
Received 30 Mar 2013; Accepted 17 May 2013; Available Online 17 May 2013

Abstract

An *ab-initio* study of the stability, structural, electronic and vibrational properties has been made for the most stable geometries of Si_xGe_y (x+y = 2 to 4) nanoclusters. Among the various configurations corresponding to a fixed x + y = n value, the configuration possessing the maximum value of binding energy (BE) is named as the most stable structure. A B3LYP-DFT/6-311G(3df) method has been employed to optimize fully the geometries of the nanoclusters. The binding energies (BEs), highest-occupied and lowest-unoccupied molecular orbital (HOMO-LUMO) gaps and the bond lengths have been reported for the most stable clusters. We have considered the zero point energy (ZPE) corrections. The adiabatic and vertical ionization potentials (IPs) and electron affinities (EAs), vibrational frequencies and infrared intensities have also been investigated for the most stable structures. The configurations containing the Si atoms in majority are seen to be the most stable structures. The strong Si-Si bond has important role in stabilizing the clusters. For the clusters containing one germanium atom and all the other as Si atoms, the BE increases monotonically with the number of the Si atoms. The HOMO-LUMO gap increases with the cluster size (x + y = n). In general, the adiabatic IP (EA) is smaller (greater) than the vertical IP (EA). All the predicted physical quantities are in good agreement with the experimental data wherever available. The growth of these most stable structures should be possible in the experiments.

Keywords: Nanoclusters; Binding energies; HOMO-LUMO gaps; Electronic properties; Vibrational frequencies

1. Introduction

Nanoclusters of metals or semiconductors can be considered as building blocks of future technologies. This is due to size dependent electronic properties of these materials. The properties of nanosized semiconductors have long been known to depend very sensitively on the particle size [1].

Recently, there have been growing interests in materials containing the group IV atoms C, Si, Ge and Sn [2 - 6]. These materials are important due to their application in the semiconductor and optoelectronic industries [7 - 10]. The Si - Ge materials have been studied extensively in past two decades and the binary heterostructure Si / $Si_{1-x}Ge_x$ has produced a new generation of high performance heterojunction bipolar transistors, field effect transistors, infrared detectors and solar cells [2, 11]. The silicon–germanium light-emitting and photodetecting devices make silicon technology quite competitive with those of conventional optoelectronic materials, such as the III–V compounds.

Atomic-scale analysis on Si-Ge materials is becoming more and more important as semiconductor devices are constantly being scaled down. It is observed that the concepts obtained from SiGe in the bulk form may not be directly applicable to SiGe at the nanoscopic level due to enormous surface energy effects and lattice strains. Therefore, the fundamental understanding of the structure and thermodynamic/electronic properties of Si-Ge nanoclusters would soon play an important role in the advancement in the nanoscale devices, especially in the interfacial areas where the lattice mismatch occurs due to the change of atomic composition.

There were not many theoretical studies of Si_xGe_y nanoclusters, probably due to lack of experimental studies. Li et al [12] have performed a density functional theory (DFT) study on neutral Si_xGe_y for x+y ≤ 10 using the B3LYP/6-311G(3df) method. Their cluster structures are selective and preserve definite symmetries. Bing et al [13] have calculated the structures and energetics of neutral and anionic Si_xGe_y for x+y ≤ 7 using the DFT-B3LYP and the CCSD(T) methods with the 6-311+G(d) basis. Their results are similar to those of Li et al [12]. Recently, Wielgus and co-workers [14] have studied the neutral and cationic Si_xGe_y for x+y ≤ 5 using the MP2/aug-cc-pVTZ method. They have not only identified the minimum energy structures, but also provided a molecular orbital analysis on the relative stability among isomers. For selected structures of large Si-Ge nanoparticles, Walker et al [15] have performed parameter-free density functional calculation. Rehman et al [16] have used a parameterized density functional method for stoichiometric Si_xGe_x clusters with up to x=22. Wang and Chao [24] have studied the structural and energetic properties of neutral and ionic semiconductor binary Si-Ge clusters Si_xGe_y for x+y ≤ 12 using the density functional theory (DFT-B3LYP) and coupled cluster [CCSD(T)] methods with 6-311++G(3df, 3pd) basis set.

In spite of these previous studies, IP, EA have not been studied for Si_xGe_y clusters. In the present paper, we report a comprehensive detailed study of the stability, structural, electronic, and vibrational properties of the small semiconductor binary Si_xGe_y for x+y ≤ 4 nanoclusters by using the B3LYP-DFT/6-311G (3df) method. In section 2, we present the method used in the computation. Section 3 contains

the calculation and results. The conclusions are contained in section 4.

2. Computational Methods

The linear combination of Gaussian functions is made to obtain the atomic orbitals, which are also called the contracted functions. For a precise calculation, a large basis set is chosen by increasing the number of basis functions per atom. 6-311G is a triple split valance basis set which uses three sizes of the contracted functions for each orbital type. The split valance basis set allows orbitals to change the size but they do not permit change in the shape of the orbitals. In order to overcome this limitation, we employ a polarized basis set, 6-311G (3df) by adding orbitals with the angular momentum beyond what is required for the ground state in the description of each atom. For Si and Ge atoms we add 3d functions and one f function respectively. For generating the quite accurate structural parameters the triple zeta basis set and the multiple polarization functions have been used.

The exact exchange in the Hartree-Fock theory for a single determinant is replaced in the DFT by a more general expression, the exchange-correlation functional which can include terms accounting both for the exchange energy and the electron correlation.

In BLYP, one includes the Becke exchange functional and the LYP correlation functional whereas in B3LYP, one includes Becke [17] three parameter hybrid functionals and the LYP correlation functional. The correlation function of Lee, Yang and Parr (LYP) [18, 19] which includes both local and nonlocal terms have been employed. The functional of Becke which includes the Slater exchange along with the corrections involving the gradient of the density [17] is used.

The B3LYP-DFT/6-311G(3df) version in the Gaussian-03 code [20] has been used to optimize the geometries of the silicon-germanium binary nanoclusters. The Gaussian programme contains the hierarchy of procedures corresponding to different approximation methods.

3. Calculation and Results

3.1. Stability of structures

Different types of geometries linear chain, ring, planer and three dimensional structures have been studied. The minimum energy structures are obtained by optimizing their atomic positions.

In order to have stability of cluster, we define the binding energy of the cluster. We subtract the total energy of a cluster from the sum of the energies of all the isolated atoms present in the cluster and divide the resultant quantity by the number of atoms. We name this as the binding energy (BE) per atom. For a more precise calculation, we have calculated the harmonic vibrational frequencies and the corresponding zero point energies (ZPE) have been subtracted from the earlier calculated BE values so that our final binding energy (FBE) = BE - ZPE. Among all the complexes pertaining to a specific chemical formula Si_xGe_y, the configuration possessing the maximum value of BE is named as the most stable structure.

We present all the most stable structures for Si_xGe_y ($x + y \leq 4$) nanoclusters in Figure 1. The computed Si-Si, Si-Ge, and Ge-Ge bond lengths are 2.15, 2.34, 2.40 Å and their corresponding bond energies are 3.08, 3.06, and 2.93 eV, respectively for isolated dimers. The calculated Si–Si bond lengths are in excellent agreement with the experimental values [21] 2.246 Å. The corresponding bond energies of Si_2, and SiGe dimers are 3.08, and 3.06 eV, respectively, which are in very close agreement with the experimental value [21,3] 3.24 and 3.08 eV. One may expect the minimum energies for those complexes, which contain the maximum number of Si–Si bonds followed by Si–Ge and Ge–Ge bonds.

The FBE's and HOMO-LUMO gaps are given for all the optimized most stable structures in Table 1. The HOMO-LUMO gaps reported by other workers have also been included for comparison. During the optimization for each structure, we have selected the ground state with minimum energy. For the most stable structures, the calculated Si-Si, Si-Ge, and Ge-Ge bond lengths, IPs & EAs and harmonic vibrational frequencies are compared with others' values in Table 2, 3 and 4, respectively.

We now discuss each cluster individually in the following:

SiGe: The ground state of SiGe cluster is triplet state and the singlet state lies above it at 0.7 eV. The present FBE is 1.51 eV. No experimental value is available for comparison. The computed bond energy for Si – Ge bond is 3.06 eV, which is in excellent agreement with the experimental value [3] 3.08 eV. The computed Si – Ge bond length is 2.34 Å which is in agreement with other workers [4, 22, 23] and slightly higher than the reported values [12, 13].

$SiGe_2$: For $SiGe_2$ ($x + y = 3$), the most stable structure is the triangular one whose ground state is singlet. The FBE for it is 2.16 eV. The computed GeSiGe angle is 84.65˚ which is in close agreement with earlier workers [12, 13, 24] values 85˚, 84.7˚, and 84.52˚. The calculated Si-Ge bond lengths 2.25 Å are in excellent agreement with the values as reported in Table 2. No experimental data is available for the comparison of above reported values.

Si_2Ge: The most stable structure reported for Si_2Ge ($x + y = 3$) is the planer triangular structure. The ground state of the Si_2Ge triangular one is the triplet state and its computed FBE is 2.19 eV. No experimental result is available for comparison. The bond angle SiGeSi is 56.71˚ which in agreement with other theoretical values [12, 13, 24] values 57˚, 56.9˚, and 56.96˚. The calculated Si-Ge and Si-Si bond lengths are 2.39 and 2.27 Å respectively and Si-Ge bond lengths are in good agreement the values reported by other workers as shown in Table 2.

$SiGe_3$: The most stable structures for the chemical species $SiGe_3$ are rhomboidal structures a & b with the symmetries C_{2v} and C_s. These structures have FBE's 2.50 and 2.52 eV, respectively. Their ground states are singlet one. The computed Si-Si and Si-Ge bond lengths are reported in Table 2 and are in agreement with other workers.

Si_2Ge_2: The linear, planer and three dimensional structures have been studied for Si_2Ge_2. Among the studied structures the most stable structures are the rhombus and rhomboidal structures. Their FBE's are 2.60 and 2.57 eV respectively. Our predicted values of Si-Ge and Si-Si bond lengths for the rhombus structure are 2.39 and 2.44 Å which are in excellent agreement with values of other workers reported in Table 2. Our values of bond lengths for the rhomboidal structures are also compared with other workers in Table 2.

Si_3Ge: The rhomboidal structures a & b are the most stable structures out of different studied structures for Si_3Ge species. Their predicted FBE's are 2.62 and 2.65 eV. The

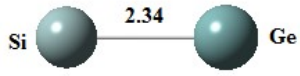

SiGe Linear ($C_{\infty v}$)

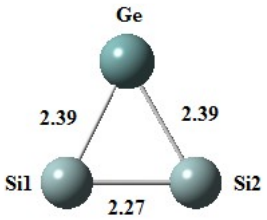

Si_2Ge Triangular (C_{2v})

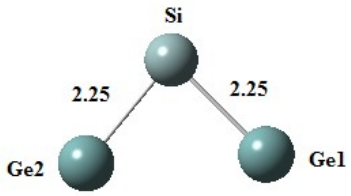

$SiGe_2$ Triangular (C_{2v})

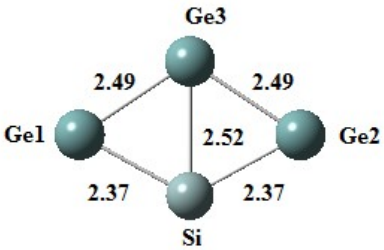

$SiGe_3$ Rhomboidal (C_s)-a

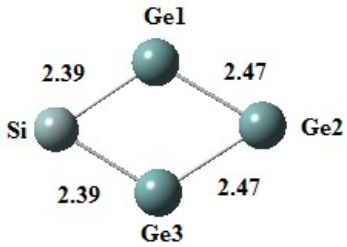

$SiGe_3$ Rhomboidal (C_{2v})-b

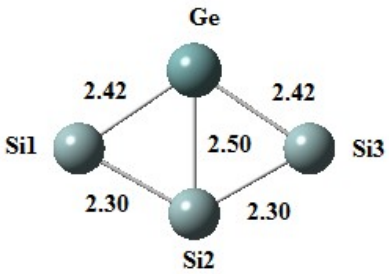

Si_3Ge Rhomboidal (C_s)-a

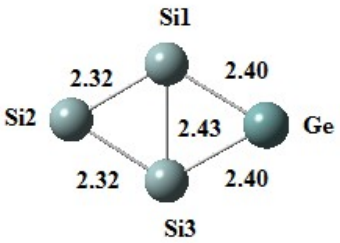

Si_3Ge Rhomboidal (C_{2v})-b

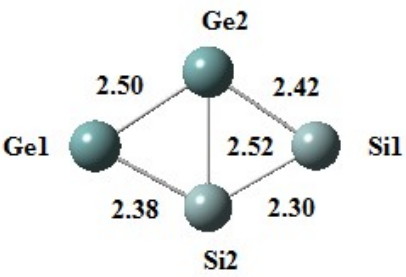

Si_2Ge_2 Rhomboidal (C_s)-a

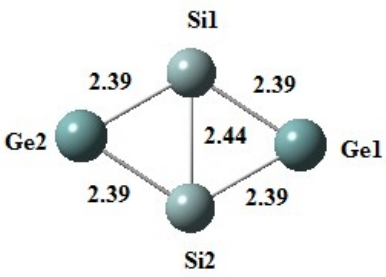

Si_2Ge_2 Rhombus (D_{2h})-b

Figure 1. Optimized most stable structures of Si_xGe_y (x + y = 2 to 4). The bond lengths are in Å.

computed Si-Ge and Si-Si bond lengths for both the structures are in good agreement with other workers as reported in Table 2. No experimental values are available for comparison.

Our predicted values of FBE's are shown in Table 1. The variation of FBE with cluster size (x + y = n) for the most stable structures are shown in the Figure 2(a). We observe that the FBE increases continuously as we go from n= 2 to 4. The most stable structures are those which contain the maximum number of Si atoms because of the occurrence of strong Si-Si bonds. The clusters containing one Ge atom, the FBE increases monotonically with the number of Si atoms.

3.2. Electronic structure

The predicted HOMO-LUMO gaps for all the studied most stable structures are included in Table 1 and their variation with the cluster size (x + y = n) for the most stable structures are shown in the Figure 2(b). The HOMO-LUMO gap increases with the increase of number of atoms. The

Table 1. The binding energy (BE) per atom and HOMO–LUMO gap in eV for the most stable configurations of Si_xGe_y ($x + y = 2$ to 4) clusters. The final binding energy (FBE) = BE − zero point energy (ZPE).

Clusters	Configurations	BE without ZPE (eV)	ZPE (eV)	FBE(eV)	HOMO-LUMO Gap (eV)	
					Present	Others
SiGe	Linear	1.53	0.02	1.51	1.65	1.36[a], 3.4[b]
$SiGe_2$	Triangular	2.22	0.06	2.16	2.44	2.44[a], 2.43[b], 2.45[c]
Si_2Ge	Triangular	2.25	0.06	2.19	1.90	1.90[a], 2.23[b], 3.59[c]
$SiGe_3$	Rhomboidal – b	2.58	0.08	2.50	2.30	2.39[a], 2.41[c], 2.30[b]
	Rhomboidal - a	2.61	0.09	2.52	2.39	2.30[b], 2.39[c]
Si_2Ge_2	Rhomboidal - a	2.67	0.10	2.57	2.35	2.35[b], 2.36[c]
	Rhombus - b	2.70	0.10	2.60	2.46	2.46[a], 2.46[b], 2.49[c]
Si_3Ge	Rhomboidal - a	2.73	0.11	2.62	2.34	2.34[b], 2.35[c]
	Rhomboidal - b	2.76	0.11	2.65	2.39	2.39[b], 2.42[c]

[a]Li et al (Ref. 12) [b]Wang et al (Ref. 24) [c]Bing et al (Ref. 13)

Table 2. Bond lengths (in Å) for all the most stable configurations of Si_xGe_y (x + y = 2 to 4) clusters.

Cluster	Configuration	Bonds	Bond lengths(Å)	
			Present	Others
SiGe	Linear	Si-Ge	2.34	2.22[a], 2.229[b], 2.32[c], 2.36[d], 2.34[e]
$SiGe_2$	Triangular	Si-Ge	2.25	2.25[a], 2.256[b], 2.25[f]
		Ge-Ge	3.03	
Si_2Ge	Triangular	Si-Ge	2.39	2.39[a], 2.395[b], 2.386[f]
		Si-Si	2.27	
$SiGe_3$	Rhomboidal - b	Si-Ge1(Ge3)	2.39	2.37[a], 2.40[b]
		Ge2-Ge1(Ge3)	2.47	2.49[a], 2.477[b]
		Si-Ge2	4.12	
		Ge1-Ge3	2.59	2.605[b], 2.594[f]
	Rhomboidal - a	Si-Ge1(Ge2)	2.37	2.38[b]
		Ge3-Ge1(Ge2)	2.49	2.502[b]
		Si-Ge3	2.52	2.541[b], 2.527[f]
Si_2Ge_2	Rhomboidal - a	Si1-Si2	2.30	
		Ge1-Ge2	2.50	
		Si1-Ge2	2.42	2.46[b]
		Si2-Ge1	2.38	2.384[b]
		Si2-Ge2	2.52	2.525[b], 2.515[f]
	Rhombus - b	Ge1(Ge2)-Si1(Si2)	2.39	2.39[a], 2.402[b]
		Si1-Si2	2.45	2.44[a], 2.463[b], 2.443[f]
Si_3Ge	Rhomboidal - a	Si2-Si1(Si3)	2.30	2.310[b]
		Ge-Si1(Si3)	2.42	2.428[b]
		Si2-Ge	2.50	2.510[b], 2.501[f]
	Rhomboidal - b	Ge-Si1(Si3)	2.40	2.405[b]
		Ge-Si1(Si3)	2.32	2.326[b]
		Si1-Si3	2.43	2.447[b], 2.431[f]

[a]Li et al (Ref. 12), [b]Bing et al (13), [c]Levent (Ref. 22), [d]Sefyani(Ref. 23), [e]Jan et al (Ref. 4), [f]Wang et al (Ref. 24)

Table 3. Adiabatic and vertical ionization potential (IP) and electron affinity (EA) in eV for all the most stable configurations of Si_xGe_y (x + y = 2 to 4) clusters.

Cluster	Configuration	IP (eV)		EA (eV)	
		Vertical	Adiabatic	Vertical	Adiabatic
SiGe	Linear	7.74	7.73	1.80	1.84
$SiGe_2$	Triangular	8.03	7.96	1.70	1.86
Si_2Ge	Triangular	8.06	7.88	2.15	2.18
$SiGe_3$	Rhomboidal - a	7.93	7.66	1.91	1.93
	Rhomboidal - b	7.81	7.55	1.90	2.07
Si_2Ge_2	Rhomboidal - a	7.91	7.65	1.93	1.96
	Rhombus - b	8.06	7.83	1.95	1.97
Si_3Ge	Rhomboidal - a	7.92	7.66	1.96	1.98
	Rhomboidal - b	8.00	7.80	1.97	1.99

Table 4. The calculated vibrational frequencies (cm^{-1}) and infrared intensities (IR Int. in Km mol^{-1}) for the most stable configurations of Si_xGe_y (x + y = 2 to 4) clusters.

Cluster	Configuration	Frequency/IR Int.
SiGe	Linear	**396/0.31** 419[a*] ; 431[b] ,426[c], 411[d], 387[e], 397[f], 396[g]
$SiGe_2$	Triangular	**112/0.90, 424/34.36, 427/5.24** (112, 424, 427)[b] (110, 421, 423)[c] (111, 423, 426)[g]
Si_2Ge	Triangular	**244/0.28, 275/1.34, 441/0.52** (243, 274, 440)[b] (237, 237, 435)[c] (148, 426, 432)[g]
$SiGe_3$	Rhomboidal- a	**67/1.33, 144/0.0, 211/1.62, 266/8.68, 274/0.07, 384/23.61** (66, 140, 203, 240, 340, 397)[c] (240, 341, 401)[g]
	Rhomboidal - b	**62/0.72, 140/0.10, 204/0.09, 240/7.34, 341/1.03, 402/38.30** (240, 342, 403)[b] (68, 144, 203, 240, 340, 397)[c] (148, 426, 432)[g]
Si_2Ge_2	Rhomboidal - a	**73/1.72, 162/0.18, 238/4.52, 301/3.38, 361/3.19, 467/41.62** (79, 161, 237, 298, 358, 462)[c] (238, 300, 466)[g]
	Rhombus- b	**67/0.83, 180/1.28, 214/0.0, 373/0.0, 396/58.15, 411/0.24** (67, 180, 396)[b] (75, 177, 212, 366, 391, 403)[c] (67, 180, 395)[g]
Si_3Ge	Rhomboidal- a	**82/2.83, 196/0.13, 304/0.71, 318/6.58, 420/0.52, 488/53.10** (91, 194, 301, 315, 416, 484)[c] (81, 317, 487)[g]
	Rhomboidal - b	**75/2.0, 205/1.50, 270/3.62, 405/0.01, 414/14.06, 480/46.19** (87, 200, 268, 398, 408, 473)[c] (269, 413, 479)[g]

[*]Expt. Value= 419 cm^{-1} (Ref. 5)
[a]Li et al (Ref. 5), [b]Li et al (Ref. 12), [c]Bing et al (Ref. 13), [d]Levent et al (Ref.22), [e]Sefyani (Ref. 23), [f]Jan et al (Ref. 4), [g]Wang et al (Ref. 24)

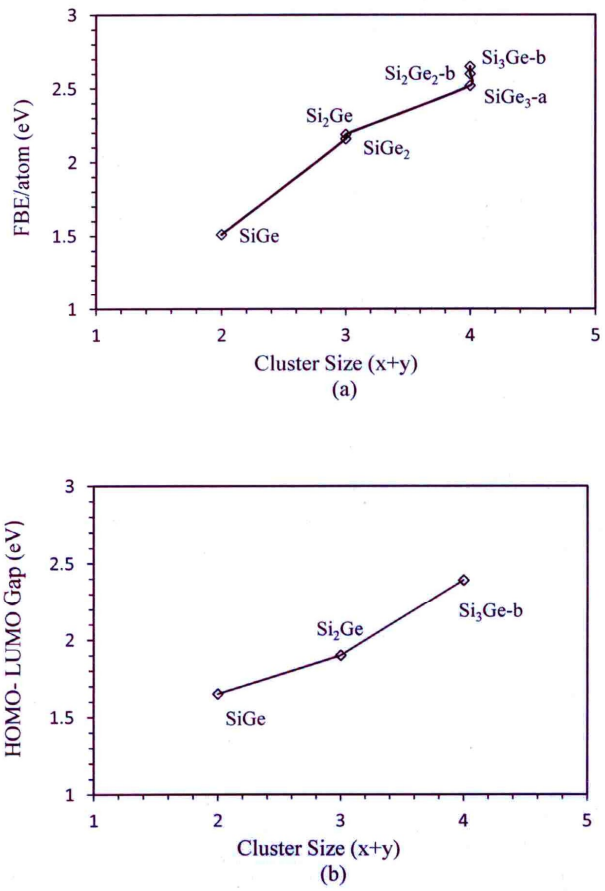

Figure 2. Variation of (a) FBE and (b) HOMO-LUMO gap with cluster size (x + y).

presently reported values are in good agreement with the values reported by earlier workers shown in Table 1.

3.2.1. Ionization potential and electron affinity

The ionization potential (IP) is defined as the amount of energy required to remove an electron from a cluster. We determine the adiabatic IP by evaluating the energy difference between the neutral and the ionized clusters after finding the most stable state for the ionized clusters by using the optimization procedure.

The electron affinity (EA) is defined as the energy released when an electron is added to a neutral cluster. We have determined the adiabatic EA by finding the energy difference between the neutral and the anionic clusters. The anionic cluster has been relaxed to its most stable state.

The adiabatic and vertical IPs and EAs are calculated using B3LYP-DFT/6-311G(3df) method for the most stable structures of Si_xGe_y ($x + y \leq 2$ to 4) nanoclusters. Our predicted adiabatic and vertical IPs and EAs for the most stable clusters are included in Table 3. The adiabatic IP (EA) is smaller (greater) than the vertical IP (EA). Furthermore IPs are significantly higher than the EAs, meaning that the molecules are more apt to gain an electron than to lose one.

It may be pointed out that adiabatic IP can be measured by using photoionization or photoelectron spectroscopic methods. On the other hand, when a technique such as fast electron bombardment is employed, the ionization occurs during the period of collision which enables the ionized cluster, the IP is named as vertical. In general, in adiabatic IP and EA, the cationic and anionic cluster relaxes to the most stable ground state whose energy is lower as compared to the ground state of the unrelaxed charged cluster. For the removal of an electron from the neutral cluster, one has to supply the necessary energy because the ground state of the cationic cluster is higher than the ground state of the neutral cluster by the same amount of energy and this energy is called the IP. In case of adiabatic ionization potential (AIP), the positively charged cluster relaxes by changing its atomic positions acquiring larger various bond lengths to find a low energy ground state as compared to the energy of the cationic cluster without any relaxation (used for the vertical IP). One observes dilation in the positively charged cluster because of the relaxation. The adiabatic IP will thus be lower than the vertical IP.

On the other hand, on adding an electron to the neutral cluster, the resulting ground state of the anionic cluster is lowered by energy equal to the electron affinity. In this case, the anionic cluster is allowed to obtain the most stable ground state by incurring relaxation in the atomic positions. We find a contraction (smaller than the dilation observed in the cationic cluster) in the size of the cluster reducing the various bond lengths. As a result of the atomic relaxation, the most stable ground state lies lower than the ground state corresponding to the unrelaxed cluster considered in determining the vertical EA. The adiabatic EA are therefore larger than the vertical EA.

3.3. Vibrational frequencies

The harmonic vibrational frequencies are calculated using B3LYP-DFT/6-311G(3df) method for the most stable structures of Si_xGe_y ($x + y \leq 2$ to 4) nanoclusters. These calculations were performed with the lowest energy configurations of Si_xGe_y ($x + y \leq 2$ to 4) nanoclusters in order to confirm that they are true minima on the cluster potential energy surface (PES). The calculated results show that there is no imaginary frequency, implying that the structures are located at minimum position on PES. The presently calculated vibrational frequencies and Infrared Intensities (IR Int.) for the most stable structures of Si_xGe_y ($x + y \leq 2$ to 4) nanoclusters are presented in Table 4. We discuss each nanocluster below:

SiGe: We obtain the stretching mode frequency of 396 cm^{-1} which is 5% less than the experimentally measured [5] value of 419 cm^{-1} and similar low frequency has been obtained by earlier workers [4, 22, 23] except by workers [12, 13, 24] who have reported frequencies 431, 426, 411 cm^{-1} similar to the experimental value. This stretching mode frequency is IR active.

$SiGe_2$: For $SiGe_2$ ($x + y = 3$), we obtained three vibrational frequencies 112, 424 and 427 cm^{-1} for the triangular structure. The first two frequencies are of symmetric and asymmetric stretching and highest one is due to bending mode. The asymmetric mode of vibration is highly IR active. These predicted values are in good agreement with others values [12, 13, 24].

Si_2Ge: The predicted vibrational frequencies for the triangular planer structure are 244, 275 and 441 cm^{-1}. The highest frequency 441 cm^{-1} is due to stretching of Si-Si bond and the frequencies 275 and 244 cm^{-1} are due to asymmetric stretching and bending mode. The asymmetric mode of vibration is IR active. Our values are compared with others in Table 4.

$SiGe_3$: For the rhomboidal-a (C_s) and rhomboidal-b (C_{2v}) structures our predicted vibrational frequencies are reported in Table 4. For rhomboidal-a three highest

frequencies are in good agreement with other workers [13, 24] and the highest three frequencies for rhomboidal-b are in agreement with others values [12, 13]. The frequency 384 and 402 cm^{-1} of rhomboidal-a and rhomboidal-b, respectively, are highly IR active.

Si_2Ge_2: The calculated vibrational frequencies for rhomboidal – a and rhombus – b are shown in Table 4 and compared with the values reported by others [12, 13, 24]. The frequencies 467 and 396 cm^{-1} of rhomboidal and rhombus structure, respectively, are highly IR active. No experimental result is available for comparison.

Si_3Ge: The predicted values of rhomboidal-a and rhomboidal-b are depicted in Table 4. Our values are compared with others [12, 13, 24] as shown in Table. The highest frequencies of the above two structures are highly IR active. Unfortunately no experimental result is available for comparison.

4. Conclusions

The present study establishes the occurrence of the most stable configurations of the various Si_xGe_y nanoclusters. For Si_xGe_y nanoclusters, we have predicted the bond lengths, binding energies, HOMO-LUMO gaps, IPs, EAs, vibrational frequencies and IR int., many of which need to be verified experimentally. The vibrational frequencies of Si-Ge cluster is in good agreement with the experimental data wherever available.

The most stable structures are those which contain the maximum number of silicon atoms because of the occurrence of the strongest Si–Si bonds whereas the lowest binding is seen for clusters containing maximum number of germanium atoms because of the occurrence of maximum number of the weak Ge–Ge bonds. For the clusters containing maximum number of silicon atoms i.e. the clusters containing only one germanium atom, the BE increases monotonically with the number of silicon atoms. The HOMO-LUMO gap increases with the increase in the number of atoms. The adiabatic IP (EA) is smaller (greater) than the vertical IP (EA) because of the lower energies of the most stable ground state of the cationic (anionic) clusters. The IPs are significantly higher than the EAs, meaning that the molecules are more apt to gain an electron than to lose one.

References

1. G. Schmid, M. Baumle, M. Greekens, I. Heim, C. Osemann, T. Sawitowski, Chem. Soc. Rev. 28 (1999) 179.
2. D. De Salvador, M. Petrovich, M. Berti, F. Romanato, E. Napolitani, A. Drigo, J. Stangl, S. Zerlauth, M. Muhlberger, F. Schafffler, G. Bauer, P. C. Kelires, Phys. ReV. B 61 (2000) 13005.
3. J. Drowart, G. D. Maria, A. J. H. Boerboom, M. G. Inghram, J. Chem. Phys. 30 (1959) 308.
4. Jan, R. Nino, R. S. Dennis, J. Chem. Phys. 87 (1987) 6562.
5. S. Li, R. J. Van Zee, W. Weltner, Chem. Phys. Lett. 229 (1994) 531.
6. J. Bai, L. F. Cui, J. L. Wang, S. H. Yoo, X. Li, J. Jellinek, C. Koehler, T. Frauenheim, L. S. Wang, X. C. Zeng, J. Phys. Chem. A 110 (2006) 908.
7. I. Shim, M. Sai Baba, K. A. Gingerich, Chem. Phys. 277 (2002) 9.
8. G. Abbate, V. Barone, F. Lelj, E. Iaconis, N. Russo, Surf. Sci. 152-153 (1985) 690.
9. M. Gazicki, H. Szymanowski, J. Tyczkowski, L. Malinovsky, J. Schalko, W. Fallmann, Thin Solid Films 256 (1995) 31.
10. S. Kumar, H. J. Trodahl, Thin Solid Films 193-194 (1990) 72.
11. K. Maiti, L. K. Bera, S. Maikap, S. K. Ray, N. B. Chakrabarti, R. Kesavan, V. Kumar, Def. Sci. J. 50 (2000) 299.
12. S. D. Li, Z. G. Zhao, X. F. Zhao, H. S. Wu, Z. H. Jin, Phys. Rev. B 64 (2001) 195312.
13. Bing, Q. C. Nguyen, X. F. Fan, J. L. Kuo, J. Phys. Chem. A 112 (2008) 2235.
14. P. Wielgus, S. Roszak, D. Majumdar, J. Saloni, J. Leszczynski, J. Chem. Phys. 128 (2008) 144305.
15. B. G. Walker, S. C. Hendy, R. D. Tilley, Eur. Phys. J. B 72 (2009) 19.
16. H. Rehman, M Springborg, Y. Dong, J. Phys. Chem. A 115 (2011) 2005.
17. A. D. Becke, J. Chem. Phys. 98 (1993) 5648; Phys. Rev. A 38 (1988) 3098.
18. C. Lee, W. Yang, R. G. Parr, Phys. Rev. B 37 (1988) 785.
19. B. Miehlich, A. Savin, H. Stoll, H. Preuss, Chem. Phys. Lett. 157 (1989) 200.
20. GAUSSIAN 03, Revision C.03, Gaussian, Inc., Pittsburgh PA (2003).
21. K. P. Huber, G. Herzberg, Constants of Diatomic Molecules, Van Nostrand Reinhold, New York (1979).
22. S. Levent, Y. Yukio, F. S. Henry, J. Chem. Phys. 119 (2003) 8266.
23. F. L. Sefyani, J. Schamps, J. M. Delaval, J. Mol. Spectrosc. 162 (1993) 269.
24. Y. S. Wang, S. D. Chao, J. Phys. Chem. A 115 (2011) 1472.

Cite this article as:

R. K. Yadav *et al.*: **Ab–initio study of structural, electronic and vibrational properties of Si_xGe_y ($x + y \leq 4$) nanoclusters.** *Phys. Express* 2014, **4:** 8